Thèse de doctorat

Présentée à la faculté des sciences&Département de Physique

Université Sultan Qaboos, Sultanat d'Oman

En co-tutelle avec

Université Paris 13, France

Pour l'obtention du diplôme de

**DOCTORAT DE PHYSIQUE**

Présentée par**:**

***Maya Al-Azri***

# Structural and Magnetic Properties of Mn Implanted 6H-SiC

Soutenue Publiquement le 10/09/2013

Devant le jury:

| | | | |
|---|---|---|---|
| Edaman Krishnan | Professor | Sultan Qaboos University, Oman | Chairman |
| Mohamed Elzain | Professor | Sultan Qaboos University, Oman | Supervisor |
| Khalid Bouziane | Professor | Université Internationale de Rabat, Morocco | Co-Supervisor |
| S. Mourad Chérif | Professor | Université Paris 13, France | Co-Supervisor |
| Frédéric Mazaleyrat | Professor | ENS-Cachan, France | External examiner |
| Osama Awadelkarim | Professor | Penn State University, USA | External examiner |
| Mohamed Belmeguenai | Associate Professor | Université Paris 13, France | Examiner |
| Rachid Sbia | Associate Professor | Sultan Qaboos University, Oman | Internal Examiner |

**LSPM (CNRS-UPR 3407), Université Paris 13, 99 Avenue J.B. Clément, 93430 Villetaneuse, France**

**Abstract**: In this study, n-Type 6H-SiC(0001) substrates were implanted with three fluencies of $Mn^+$ $5\times10^{15}$ Mn/cm$^2$ (Mn content: 0.7%), $1\times10^{16}$ (~2 %), and $5\times10^{16}$ cm$^{-2}$ (7%) with implantation energy of 80 keV and substrate temperature of 365°C. The samples were characterized using Rutherford Backscattering and Channeling Spectroscopy (RBS/C), High Resolution X-Ray Diffraction technique (HRXRD), micro Raman Spectroscopy (μRS) and Superconducting Quantum Interference Device (SQUID) techniques. The aims were to investigate implantation-induced defects upon dose and to study any correlation between disorder-composition and magnetic properties. RBS/C spectra were fitted using McChasy code, and the corresponding results show that 41% of Mn occupy substitutional sites for the lowest dose , 63% for intermediate Mn content, whereas an almost amorphization occurred for the highest dose. The hysteresis loops of the all samples have typical ferromagnetic shapes. The maximum magnetic moments were obtained for the fluence of $1\times10^{16}$ Mn/cm$^2$ at which the ratio of Mn at substitutional site was maximum. In addition, we investigated the structural and magnetic properties of Mn-doped 6H-SiC using ab-initio calculations. Various configurations of Mn sites and vacancy types were considered. The calculations showed that a substitutional Mn atom at Si site possesses larger magnetic moment than Mn atom at C site. A model is introduced to explain the dependence of the magnetic structure on site occupation. The magnetic properties of ferromagnetically (FM) and antiferromagnetically (AFM) coupled pair of Mn atoms with and without neighboring vacancies have also been explored.

Keywords: Silicon Carbide, Ion implantation, Defects, Magnetic properties, *ab-initio* Calculations

**Résumé:** Dans cette étude, des substrats 6H-SiC (0001) de type-n ont été implantés avec trois concentrations de $Mn^+$ : $5\times10^{15}$ Mn/cm$^2$ (teneur en Mn: 0,7%), $1\times10^{16}$ (~ 2%), et $5\times10^{16}$ cm$^{-2}$ (7 %) à une énergie d'implantation de 80 keV et pour une température de substrat de 365° C. Les échantillons ont été caractérisés par spectroscopie de rétrodiffusion de Rutherford, diffraction des rayons-X à haute résolution, spectroscopie micro-Raman et magnétométrie SQUID. L'objectif est d'étudier l'effet des défauts induits par l'implantation et de déduire une corrélation avec les propriétés magnétiques. Les résultats obtenus à partir des résultats de RBS/C montrent que 41% des Mn occupent les sites de substitution pour la plus faible concentration, 63% pour la concentration intermédiaire, alors qu'une structure amorphe apparaît pour la dose la plus élevée. Les cycles d'hystérésis présentent des formes typiques d'une réponse ferromagnétique. Le moment magnétique maximal a été obtenu pour la concentration $1\times10^{16}$ Mn/cm$^2$ à laquelle le taux de Mn en site de substitution est maximal. Les résultats expérimentaux ont été confrontés aux résultats des calculs *ab initio*. Différentes configurations de sites Mn et types d'occupation ont été pris en compte. Les calculs ont montré qu'un atome de Mn substitué sur le site d'un atome de Si possède un moment magnétique supérieur à celui d'un atome Mn sur un site C. Un modèle est introduit pour expliquer la dépendance de la structure magnétique au type d'occupation des sites. Les propriétés magnétiques de paires d'atomes Mn couplés, type ferromagnétique (FM) et antiferromagnétique (AFM), avec et sans sites voisins vacants, ont également été explorées.

Mots-clés: Carbure de Silicium, Implantation ionique, Défauts, Propriétés magnétiques, Calculs *ab initio*

**To my mother, husband and kids**

# Acknowledgments

Much of the work presented in this thesis would never have materialized but for the support, advice and companionship that I got from so many people, both in my professional, as well as my personal life. First of all, I would like to express my sincere gratitude to my supervisor, Prof. Mohammed Elzain for his continuous support during my PhD research. It was a pleasure working under his supervision and I appreciate his constant guidance, encouragement and support. I would like also to express my gratitude to my co-supervisor, Prof. Khalid Bouziane from Université Internationale de Rabat (Morocco) for his great support and knowledge and many insightful discussions and suggestions. I am also very grateful to my co-supervisor, Prof. Mourad Chérif from Université Paris 13 (France) for his continuous support, guidance and encouragements in achieving the research goals. I want to thank him also for his great help and assistance during my stay at Université Paris 13. There are not enough words to express my gratitude to my supervisors for their willingness to share their knowledge with me, numerous discussions and support that they have giving me.

My warmest thanks go to Prof. Lionel Thomé from Université d'Orsay (France) and Prof. Alain Declémy from Université de Poitiers (France) for giving part of their valuable time to help in the structural characterization, which results were very valuable in this study. Sincere thanks to Dr. Michel Viret from CEA Saclay (France) for help in SQUID measurements.

I gratefully acknowledge the department of physics in SQU and LSPM in Université Paris 13, for the assistance and the facilities received during my PhD study. Special thanks to Prof. Mujibur Rahman, Head of Physics Department, for his valuable comments and support. I am also grateful to all kind people at LSPM (Université Paris 13) for their support and help during my stay there.

Special thanks are extended to the Ministry of Education and SQU for giving me the chance to do my PhD and for the financial support. Thanks are also giving to my real friends who were highly supportive during my PhD study.

Last but not least, I want to express my heartfelt thanks to my mother, husband, and children for understanding, encouragement and patience during my study.

# Table of Contents

Abstract ii

Acknowledgments iv

Table of contents v

List of Figures viii

List of Tables xiii

**CHAPTER 1: INTRODUCTION** 1-20

**1.1 Silicon Carbide (SiC)** 2

1.1.1 Silicon Carbide crystallography 3

1.1.2 The physical properties of SiC 6

**1.2 SiC based DMS** 7

1.2.1. Defects in SiC 9

1.2.2 Damage recovery 11

**1.3 Models describing magnetism in DMS** 14

1.3.1 Mean Field Theory 15

1.3.2 Impurity Band Model 17

1.3.3 Bound Magnetic Polaron (BMP) 18

**CHAPTER 2: METHODOLOGY** 21-61

**2.1 Ion Implantation in SiC** 22

2.1.1 Ion implantation 22

2.1.2 Physics of ion penetration in solids 25

2.1.3 Simulation of ion implantation profiles 27

**2.2 Experimental Techniques** 29

2.2.1 Rutherford backscattering and channeling spectrometry (RBS/C) 29

2.2.1.1 Channeling and RBS/C 31

2.2.1.2 Analysis of an RBS/C spectrum 33

2.2.2 High-Resolution X-Ray Diffraction (HRXRD) 35
2.2.2.1 Analysis of an XRD spectrum 37
2.2.3 Micro Raman Spectroscopy (µRS) 39
2.2.4 Magnetometry techniques 41
2.2.4.2 SQUID Magnetometry 42
2.2.5 Hall effect measurements 44
**2.3 Ab-initio calculations** 49
2.3.1 Density Functional Theory (DFT) 49
2.3.2 The exchange – correlation potential 52
2.3.2.1 The Local Density Approximation (LDA) 52
2.3.2.2 The generalized gradient approximation (GGA) 53
**2.3.2 GGA+U** 53
**2.3.3 Solution of Khon-Sham equations** 55
2.3.3.1 Augmented Plane Wave method (APW) 56
2.3.3.2 Linear Augmented Plane Wave Method (LAPW) 57
**2.3.4 The WIEN2k Code** 59

**CHAPTER 3: RESULTS AND DISCUSSION** 62-127

**3.1 Ion implantation-induced lattice damage** 63
**3.1.1** Structural characterization 66
3.1.1.1 Defects and Mn profiles 66
3.1.1.2 Implantation induced Strain 77
3.1.1.3 Micro-Raman spectroscopy (µRS) measurements 81
**3.2 Magnetic characterization** 85
**3.3 Subsequent thermal annealing treatment** 89
3.3.1 Structural characterization 90
3.3.2 Magnetic properties 95
3.3.3 Annealing temperature effect 100
**3.4 Ab-initio calculations results** 107

3.4.1 The electronic structure of virgin 6H-SiC 108
3.4.2 Magnetic moments in Mn-doped 6H-SiC 109
3.4.3 Coupled impurities 118
3.4.4 Magnetic coupling strength 122
3.4.5 Relaxation effect 124
3.4.6 GGA+U results 125

**CHAPTER 4**: **CONCLUSIONS** 128-133

**4.1 Conclusions** 128
Publications 134
References 136
Appendix A 144
Appendix B 145

# List of Figures


| | | |
|---|---|---|
| **Figure 1.1** | The tetragonal cell of SiC. | 3 |
| **Figure 1.2** | Schematic diagram of atomic arrangements in the different SiC polytypes. | 4 |
| **Figure 1.3** | (a) The stacking sequence Si-C double layers of the most common SiC polytypes. (b) Three-dimensional perspective views of the primitive unit cells of the most common SiC polytypes. | 5 |
| **Figure 1.4** | RBS/C spectra of $P^+$ implanted 6H-SiC samples at room temperature and at 800 °C. | 11 |
| **Figure 1.5** | Representation of carrier-mediated ferromagnetism in p-type DMS. | 16 |
| **Figure 1.6** | Representation of Magnetic Polarons in a semiconductor lattice. | 19 |
| **Figure 2.1** | Schematic of an ion implanter showing (1) ion source, (2) mass spectrometer, (3) ion electrostatic accelerator (4) beam scanning system and (5) end station, where the target is mounted. | 22 |
| **Figure 2.2** | Some parts of the Ion implanter at CSNSM-CNRS lab. | 23 |
| **Figure 2.3** | Point defects: (a) vacancy, (b) interstitial atom, (c) small substitutional atom, (d) large substitutional atom, (e) Frenkel defect–ionic crystals. | 24 |
| **Figure 2.4** | Schematic graph of typical electronic and nuclear energy loss as a function of energy. | 26 |
| **Figure 2.5** | A particle incident on a solid penetrated with a total path length R, resulting in a projected range Rp, along the direction parallel to the incident ion. | 27 |
| **Figure 2.6** | Simulated penetration trajectories of 10,000 electrons inside SiC for 170 keV. | 28 |
| **Figure 2.7** | Experimental setup employed in RBS. b) Schematic illustration of the RBS principle from the point of view of a classical two-particle collision event. | 30 |

| | | |
|---|---|---|
| **Figure 2.8** | Schematic representation of the channeling effect. | 31 |
| **Figure 2.9** | The random and channeled RBS measurements for virgin 6H-SiC sample**.** | 33 |
| **Figure 2.10** | (a) ARAMIS accelerator in CSNSM lab, (b) The sample chamber. | 34 |
| **Figure 2.11** | Diffraction of the X-ray beam at the atomic planes in the crystal. | 36 |
| **Figure 2.12** | Source, sample and detector configuration during 2θ-θ scan. | 36 |
| **Figure 2.13** | X-ray diffraction spectra of a virgin SiC sample and of a 80 keV Mn-implanted SiC sample to a fluence of $5\times10^{15}$ at/cm$^2$. | 37 |
| **Figure 2.14** | Schematic of a micro-Raman spectrometer where illumination and collection are performed through microscope objective. | 40 |
| **Figure 2.15** | Block diagram of the VSM. | 42 |
| **Figure 2.16** | A scheme for a SQUID. | 43 |
| **Figure 2.17** | SQUID magnetometer technique at CEA Saclay with magnified sample rod. | 44 |
| **Figure 2.18** | Hall Setup. | 46 |
| **Figure 2.19** | Schematic representation of the Temperature Dependent Hall setup. | 47 |
| **Figure 2.20** | The supercell used in the calculation. | 60 |
| **Figure 3.1** | Random and channeled RBS spectra obtained from virgin 6H-SiC sample. | 63 |
| **Figure 3.2** | Channeled RBS spectra obtained from virgin 6H-SiC sample and $5\times10^{15}$ Mn/cm$^2$ implanted 6H-SiC. | 64 |
| **Figure 3.3** | Channeled RBS spectra of 80 keV Mn-implanted 6H-SiC. | 65 |
| **Figure 3.4** | The RBS/channeling spectra (A) and corresponding McChasy fits (solid lines) for samples A, B,C and D. | 67 |
| **Figure 3.5** | The RBS/C spectra for samples a, B, C and D. The solid lines are the Gaussian fitting of each spectrum. | 68 |
| **Figure 3.6** | Maximum yield of different types of defects versus fluence as deduced from Figure. 3.5. | 68 |

| | | |
|---|---|---|
| **Figure 3.7** | Schematic representation of the distribution of the vacancies and interstitials in the implanted layer. | 69 |
| **Figure 3.8** | (a) Defects profile deduced from RBS spectra using McChasy fitting, (b) accumulated damage at the surface region. | 71 |
| **Figure 3.9** | Polynomial and Gaussian fit of accumulated damage versus depth. | 73 |
| **Figure 3.10** | Mn distribution vs depth for samples B, C and D random (R) and axial (A) directions respectively. | 74 |
| **Figure 3.11** | Mn and vacancy distribution calculated by SRIM for samples B, C and D. | 74 |
| **Figure 3.12** | X-ray diffraction patterns of the four Mn-implanted 6H-SiC samples. | 77 |
| **Figure 3.13** | Strain depth profiles for Mn implanted 6H-SiC deduced from XRD patterns. | 79 |
| **Figure 3.14** | First-order Raman spectra of undoped 6H-SiC sample. | 83 |
| **Figure 3.15** | Second-order Raman spectra of undoped 6H-SiC sample. | 83 |
| **Figure 3.16** | μRS spectra for the three samples (virgin, $5\times10^{15}$ and $1\times10^{16}$ $Mn/cm^2$) in (a) axial direction and (b) polarized direction. | 84 |
| **Figure 3.17** | Hysteresis loops of the samples indicated in the graph recorded at 7 K. | 86 |
| **Figure 3.18** | RBS/C spectrum for implanted samples annealed at $1600^0$C. | 91 |
| **Figure 3.19** | RBS/C spectrum for $5\times10^{15}$, $1\times10^{16}$ and $5\times10^{16}$ $Mn/cm^2$ before and after annealing at 1600°C. | 92 |
| **Figure 3.20** | EPMA- EDX measurements of the $5\times10^{15}$ $Mn/cm^2$ at three different electrons energies: 5, 10 and 20 keV. | 94 |
| **Figure 3.21** | Hysteresis loops of the annealed samples recorded at 7 K. | 96 |
| **Figure 3.22** | Hysteresis loops of the samples recorded at 7 K before and after annealing at 1600 $^o$C. | 96 |
| **Figure 3.23** | Second-order Raman spectra of $5\times10^{15}$ $Mn/cm^2$ sample before and after annealing. | 99 |

**Figure 3.24** The first-order Raman spectra LO mode of as-implanted and annealed C and D samples. 100

**Figure 3.25** RBS/C spectrum of $5\times10^{15}$ Mn/cm$^2$ sample annealed at different temperatures. 101

**Figure 3.26** RBS/C Si yield (upper part) and the Mn Yield (lower part) for $5\times10^{15}$ Mn/cm$^2$ sample annealed at different temperatures. 102

**Figure 3.27** XRD spectra of $5\times10^{16}$ Mn/cm$^2$ samples before and after annealing at 800℃. 102

**Figure 3.28** Hysteresis loops of the $5\times10^{15}$ Mn/cm$^2$ sample annealed at different temperature, the insets are the hysteresis loop for each temperature around zero magnetic field. 103

**Figure 3.29** The supercell used in the calculation 107

**Figure 3.30** The total (upper panel) and partial densities of states of undoped hexagonal 6H-SiC. 109

**Figure 3.31** P states of 6H-SiC with Si vacancy, (b) Density of state of 3d Mn substitute Si site in 6H-SiC. 113

**Figure 3.32** P states of 6H-SiC with C vacancy, (b) Density of state of 3d Mn substitute C site in 6H-SiC. 113

**Figure 3.33** Energy level diagram of Si/C dangling bonds and 3d Mn level. 114

**Figure 3.34** Energy-level diagram of (a) Mn at Si site and (b) Mn at C site. 116

**Figure 3.35** Total (upper panel) and 3d-Mn (lower panel) densities of states of Mn-doped 6H-SiC. (a) The dopant is at the Si site with neighboring C vacancy and (b) the dopant is at the C site with neighboring Si vacancy. The Fermi level corresponds to the zero of energy. 117

**Figure 3.36** The Supercell used in the calculation of Mn-Mn magnetic ordering, (a) without vacancy, (b) with C vacancy $V_C$. 119

**Figure 3.37** Mn d states from the GGA and GGA+U calculations for different values of U for (a)Mn at Si site with nearest C vacancy and (b) Mn at C site with nearest Si vacancy. 127

| | | |
|---|---|---|
| **Figure. B.1** | A schematic diagram of RBS experiment. | 145 |
| **Figure B.2** | Components of energy loss for a projectile that scatters at a depth t. | 146 |

# List of Tables


| | | |
|---|---|---|
| **Table 1.1** | Physical Properties of different polytypes of SiC. | 6 |
| **Table 3.1** | Ratio of Mn atoms that occupy substitutional (Si and/or C) sites for samples B,C and D. | 75 |
| **Table 3.2** | Accumulated damage parameter $f_D$, percentage of Mn at substitutional site and magnetic moment of Mn implanted 6H-SiC. | 87 |
| **Table 3.3** | The estimated values of $C_{Mn}$, the saturation magnetization and the magnetic moment of the annealed samples. | 97 |
| **Table 3.4** | Energy and magnetic moments ($\mu_B$) in 6H-SiC doped with Mn atom. | 110 |
| **Table 3.5** | (a) Energy relative to the FM configuration and average magnetic moment per Mn atom for different coupled pair configurations with neighboring C vacancy and (b) Energy and average magnetic moment per Mn atom for coupled Mn atoms at substitutional and interstitial sites. | 120 |
| **Table 3.6** | Magnetic moments and energy differences between FM and AFM coupled configurations as a function of Mn-Mn distances. The energies shown are values relative to the FM energy. | 123 |
| **Table 3.7** | Energy, total magnetic moments and magnetic moment per 3d-atom.for FM and AFM configurations before and after relaxation. The energies shown are relative to the relaxed case of each configuration. | 125 |
| **Table 3.8** | Energy relative to the GGA calculation and average magnetic moment per Mn atom for different configurations with neighboring C vacancy. | 126 |
| **Table. A.1** | List of recently reported annealing studies of SiC implanted with different elements. | 143 |

# Chapter 1. Introduction

Data storage and data analysis in computer system are carried out at physically different locations and through different processes. Data storage is achieved using electronic spins of ferromagnetic (FM) materials, while data analysis is carried out using electric currents. This requires data exchange between the two locations which results in time delay. It is quite natural to ask if both the charge and spin of electrons can be used at the same time to enhance the performance of devices. This is the main idea of spintronics, which is widely expected to be the future solution to downsize current microelectronic devices into size of even nanometers. The realization of functional spintronic devices requires materials with ferromagnetic ordering at operational temperatures compatible with existing semiconductor materials.

Great expectations are placed on diluted magnetic semiconductors (DMSs) due to the possibility of integrating charge and spin degrees of freedom in a single material [1]. The idea of DMS was to dope magnetic elements such as Mn into a semiconductor host to make the semiconductor magnetic at room temperature. It is widely believed that DMS are ideal material for spintronics. Various material systems have been considered as possible candidates for DMSs applications. The most extensively studied DMS material system is (Ga,Mn)As in which ferromagnetic (FM) ordering is found with Curie temperatures ($T_C$) up to 190 K and has been successfully utilized as spin-polarized devices [2, 3]. However, this is still too low temperature for most practical applications. The mean field theory of ferromagnetism by Dietl et al [4, 5] had created a great deal of interest in magnetic properties of wide band semiconductors. The Curie temperatures were calculated based on Mn doping with a high p-type doping level. The candidates that

result in the highest Tc include III-V nitrides such as GaN and InN, as well as oxides such as ZnO. Following these predictions, a lot of DMSs research has been focused upon nitrides and oxides. ZnO and ZnS doped with transition metals were predicted to be candidates for high $T_C$ DMSs [6]. Silicon Carbide is another wide band gap semiconductor which has been considered a possible candidate for spin electronic applications. However, only few experimental studies on silicon carbide (SiC) based DMSs have been reported despite the high potential of SiC for high power and high temperature electronics.

The main objectives of this work is to study ion implantation-induced lattice damage of Mn implanted 6H-SiC and the effect of the structural disorder on the magnetic properties of the implanted samples.

In this chapter, a short description of SiC material will be given including its crystallographic structure and physical properties. Then the previous work on DMS materials based SiC and the models describing the magnetism in such materials will be described.

## 1.1 Silicon Carbide (SiC)

SiC is a wideband gap IV–IV compound semiconductor material, which is receiving attention due to its great technological interest in devices operating at high temperatures, high power, high-frequency and in harsh environments. Actually, SiC semiconductor technology has been advanced rapidly, but there are numerous problems, such as in the large-scale crystal growth, defect engineering and device performance, that need to be solved before SiC can reach its full potential. The occurrence of SiC in different crystal

structures and their definite arrangement in heteropolytypic structures with novel properties will open new fields of application for SiC.

### 1.1.1 Silicon Carbide crystallography

SiC is a IV-IV semiconductor, meaning that both Si and C atom belong to group IV elements. Each carbon atom is bonded to four silicon atoms (and vice versa) forming a tetragonal building block (Figure.1.1[7]). The nature of the bond between Si and C is not purely covalent but has a slight ionic character because of the difference in electronegativity between Si and C (C has greater electronegativity than Si).

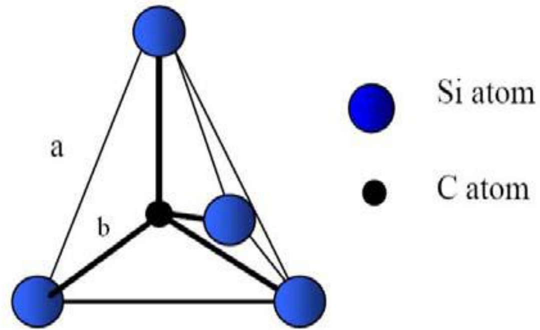


*Figure.1.1. The tetragonal cell of SiC. The distance between two nearest neighbors is approximately 3.08Å (a) whereas the distance between a C atom and a Si atom is approximately 2.52 Å (b)[7].*

Many of the materials that have tetrahedral bond form either diamond/zinc blende, or wurtzite structures. Both these structures are close packed and can be described as close-packed arrangement of equal spheres held together by interatomic forces. In the case of SiC the positions of one kind of atoms (Si) resembles that of equal close-packed spheres with other atoms residing in the voids. This structure is also regarded as close-packed, although, not ideally close-packed [8]. Another way of describing such structure is in terms of two identical interpenetrating close packed lattices, one consisting of Si and another of C atoms. These two lattices are displaced one fourth of layer spacing along C-axis from one another. In 1912, the occurrence of SiC in different crystal structures was discovered [9].This behavior of SiC was later called Polytype (polytypism). More than 250 SiC polytypes are

identified to date[10, 11]. Despite the large number of polytypes, only three crystalline structures exist: cubic, hexagonal and rhombohedral. The SiC polytypes can be described by different stacking of the Si–C double layers perpendicular to the direction of the closed-packed plane.

We describe the stacking possibilities by considering the close packed arrangement of equivalent spheres representing Si atoms on a plane (Figure 1.2). In Figure 1.2, the solid circles represent spheres closely packed in a plane; the position of this first layer we call "A". The next layer of Si atoms can be placed in the close-packed arrangement either in B (coloured circles) or C (dotted circles).

Likewise the layer above could be either in A or C (if the second layer is in B), or else in A or B (if the second layer is C). Carbon atoms reside in the voids formed between Si atoms. For each Si atom in a layer there is a corresponding carbon atom located ~1.89 Å below. Therefore the above description of stacking possibilities of layers of equal spheres should hold for bilayers of Si-C formed by corresponding layers of Si and C. The order of stacking of the planes determines the types of close-packed structures and their symmetry properties.

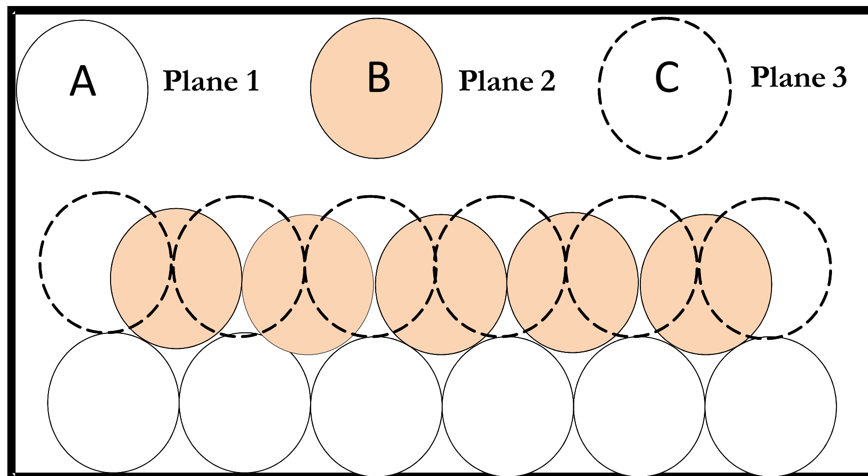


*Figure. 1.2. Schematic diagram of atomic arrangements in the different SiC polytypes.*

According to the conventional nomenclature, a SiC polytype is represented by the number of Si-C double layers in the unit cell, with the appending letter C, H, or R indicating a cubic, hexagonal or rhombohedral symmetry. For example, the 6H hexagonal lattice has six such layers in the primitive cell with the following succession of the above planes: A,B,C,A,C,B,A,B,C,A,C,B; the 3C lattice is built up as A,B,C,A,B,C; 2H-SiC corresponds to A,B,A,B; and 4H-SiC corresponds to A,B,A,C,A,B,A,C. The stacking sequence of the most common polytypes of SiC is shown in Figure (1.3).

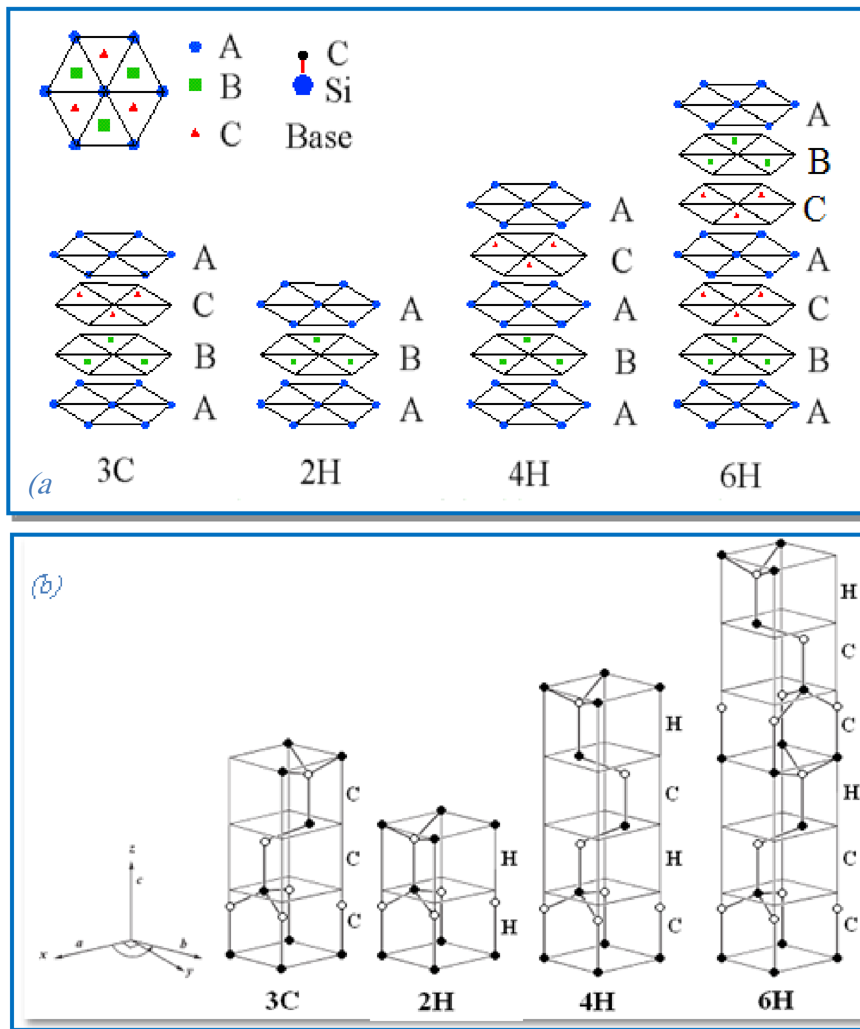


*Figure. 1.3. (a) The stacking sequence Si-C double layers of the most common SiC polytypes. (b) Three-dimensional perspective views of the primitive unit cells of the most common SiC polytypes. The cubic (C) or hexagonal (H)*[12].

## 1.1.2 The physical properties of SiC

Owing to the differing arrangements of Si and C atoms within the SiC crystal lattice, each SiC polytype exhibits unique fundamental electrical and optical properties. Some of the more important semiconductor electrical properties of the 3C, 4H, and 6H silicon carbide polytypes are given in Table 1.1. For comparison, Table 1.1 also includes comparable properties of Si and GaAs.

***Table 1.1*** *Physical properties of different polytpes of SiC* [11, 13, 14]

| | 3C-SiC | 4H SiC | 6H SiC | Si | GaAs |
|---|---|---|---|---|---|
| **Band gap Energy (eV)** | 2.3 | 3.26 | 3.03 | 1.12 | 1.43 |
| **Breakdown Field (V/cm)** | $1.5\times10^{6}$ | $3\times10^{6}$ | $3\times10^{6}$ | $2.5\times10^{5}$ | $3.0\times10^{5}$ |
| **Thermal Conductivity at Room Temperature (W/cm·K)** | 3-5 | 4.0 | 4.0 | 1.5 | 0.5 |
| **Saturated Drift Velocity (cm/s)** | $2.5\times10^{7}$ | $2.0\times10^{7}$ | $2.0\times10^{7}$ | $1.0\times10^{7}$ | $1.0\times10^{7}$ |

The most important properties of SiC are its exceptionally high breakdown electric field, wide band gap energy, high thermal conductivity, and high carrier saturation velocity. Since SiC has an energy gap $E_g>2.0$ eV, it is considered a wide band gap semiconductor. It is important to note the larger band gap for SiC compared to GaAs or Si. The wide band gap is also accompanied by considerably higher breakdown voltage as compared to silicon. For power electronics, SiC's large band gap translates into a high critical field. A high critical electric field allows device designs that have lower series resistance and lower power dissipation.

Some of the possible applications of SiC as a material for power electronics are for advanced turbine engines, automotive and aerospace electronics, and applications requiring large-radiation resistance. Properties such as large breakdown electric field strength, large saturated electron drift velocity, small dielectric constant, reasonably high

electron mobility, and high thermal conductivity make SiC an attractive candidate for fabricating power devices with reduced power losses and die size.

As it can see from Table 1.1, SiC has a higher thermal conductivity than GaAs and Si. It has been found that its thermal conductivity is higher than any other semiconductors at room temperature[15]. This property enables SiC devices to dissipate the large amount of heat generated in the high power devices. It also reduces the extra need for cooling inside the electronic devices, which could save space for integrated circuits.

## 1.2 SiC based DMS

Despite the above interesting properties and large compatibility with the mature Si technology, a little attention has been devoted to SiC. One possible reason is that most TM-doping elements have a little solubility in SiC. For this reason, dopant introduction into SiC is practically limited to ion implantation technique.

In recent studies, ferromagnetism with the Curie temperature Tc~160 K was reported in 4H-SiC doped with Mn in concentrations of up to 5% [16]. Magnetic response was observed in a more heavily doped material, and was attributed to the formation of secondary phases. Curie temperatures of 50, 250, 270 K were reported in Ni, Mn, and Fe-doped 6H-SiC, respectively, for peak concentration of 5% of substitutional TM atoms[17, 18]. Stromberg et al.[19] performed an extensive study of 6H-SiC implanted with various doses of Fe. The authors found the samples with the peak Fe concentration below 3% to exhibit DMS behavior, with the magnetic ordering disappearing above 20 K. The magnetic response in the samples with Fe concentrations above 3% was determined to originate mostly from superparamagnetic $Fe_3Si$ clusters. Room temperature ferromagnetism was also reported in V-doped 6H–SiC [20]. However, there are no reliable

data on whether the materials obtained were 'true DMSs', with the uniform distribution of the magnetic constituent, or whether the magnetic signal was due to TM clusters or secondary phases.

C. Dupeyrat et al [21] found that Fe implanted 6H-SiC exhibits a high level of substitutional fraction of Fe atoms on Si-sites and a homogeneous distribution of implanted Fe atoms but they didn't find any ferromagnetic response, even at low temperature under 1 T. SiC doped with Mn has become the most actively studied SiC DMS material. Experimental studies of Mn-implanted 3C-SiC/Si heteroepitaxial structure [22], the structural, magnetic, and magnetooptical properties of Mn-doped SiC films prepared on 3C-SiC substrates[23], and the properties of 6H-SiC films low-doped with Mn[24] and polycrystalline 3C-SiC[25] testify that Mn can be a suitable impurity for achieving a high-temperature FM ordering in the SiC DMS.

In addition to experimental work, theoretical work was done in parallel in an attempt to explain the available experimental data and to obtain guidance for experimentalists. Most of these works concentrated on first principles calculations which are a powerful tool for modeling and predicting DMS material properties.

*Ab-initio* calculations using different computational techniques were used to study the magnetic properties of SiC DMS theoretically. Miao and Lambrecht[26] studied the magnetic properties of numbers of transition metal impurities in 3C-SiC using the linearized muffin-tin orbital (LMTO) method. They found that the Si site is more favorable compared to the C site for TM substitution and that Fe and Co are non-magnetic, while Cr and Mn possess local magnetic moments. They found also that

preferred coupling between near-neighbor dopants was ferromagnetic for Cr whereas for Mn the results depend on relaxation and computational method.

Ferromagnetic ordering was later confirmed for 3C-SiC doped with V, Mn, and Cr using ultrasoft pseudopotential plane wave method[27].

Shaposhinikov and Sobolev [28] obtained similar results for atomic magnetic moments of TM impurities in 3C-SiC using the full potential linearized augmented plane wave method (FLAPW) calculation technique. The authors also studied the magnetic properties of TM impurities in 6H-SiC for Mn substitution atomic concentrations of 2% and 16%. They found that Cr and Mn possessed magnetic moments in both concentrations, while Fe was magnetic only in the atomic concentration of 2%. Andrei Los et al [29] studied the magnetic properties of Fe-doped 4H-SiC using FLAPW method, and they found that Fe can be in either a magnetic or nonmagnetic state and this depends on the TM atom environment in the host matrix.

### 1.2.1 Defects in SiC

The study of 3d transition metal point defects in SiC is very important because they can be incorporated in SiC by doping or can be present in the material as residual impurities and they play an important role in the crystal electric and magnetic properties. The TM impurity properties depend on whether it's a substitutional in C or Si sites or in an interstitial site. The existence of inequivalent lattice sites in different polytypes of SiC gives rise to a large variety of possible defects. In addition, combinations of intrinsic simple point defects are often possible, e.g. $V_{Si}$–$V_C$ divacancies, $C_{Si}$–$V_C$ vacancy–antisite pairs, N–$V_{Si}$ vacancy-impurity pairs, or even more complex defects can be formed.

Defects have different energy levels in the band gap, which can usually be detected, e.g. by optical or electron paramagnetic resonance (EPR) techniques. Due to the large band gap, intrinsic and extrinsic defects often have their ground states and in many case also the low excited states within the gap and can be electrically or optically active.

In accordance to the results of calculations based on the density-functional theory in the local-density approximation, Mn impurity located at substitutional Si site in 4H-SiC in the hexagonal as well as in the cubic layers has three levels in the gap and the Mn dopant is amphoteric as it has both donor and acceptor levels in the gap [30]. Appearance of the both donor and acceptor levels in the gap can lead to passivation of n as well as p-type unexpected additional impurities. It will lower the majority carrier concentration, both n- or p-type and will lead to the creation of semi-insulating material.

Barbosa et al [31] found that the formation energy results indicate that the Ti impurity in 3C–SiC in substitutional sites is more stable than in interstitial sites. Moreover, the Si site sublattice is the more stable one. Jing Zhou et al [32] studied the structural and magnetic properties of 3d transition metal doped 3C-SiC using *ab initio* calculations. They found that the structure of substitutional $TM_{Si}$ is the most stable one for early transition metals like Ti, V, Cr, and Mn, while the clustering of $TM_{Si}$-$TM_{I}$ dimers formed by the neighboring substitutional $TM_{Si}$ and interstitial $TM_{I}$ is energetically favored for late transition metals such as Co, Ni, and Cu. Most of theoretical work done so far concentrated on 3C-SiC with few data related TM doped 6H-SiC.

### 1.2.2 Damage recovery

The low temperature implantation techniques typically lead to a high quantity of native defects within the system. Large doses of TM atoms act as compensating defects and reduce the overall carrier (hole) concentration and ferromagnetic behavior within the samples. When ion implantation is carried out at high temperature, defect migration is more likely and crystallization is enhanced. This is confirmed by several reports on ion implanted SiC in a temperature range from liquid nitrogen temperature to 1000° C. The crystal quality of a solid can be evaluated by Rutherford Backscattering and Channeling Spectroscopy (RBS/C). For example, M. Rawaski et al [33] performed implantation of $Al^+$ ions in 6H-SiC in two different temperatures (RT and 500° C) and its removal by high temperature (up to 1600° C) thermal annealing. Following the 1300–1600° C annealing, RBS/C spectrum showed that the level of residual radiation damage in the samples implanted at RT is higher than at the 500° C implantation. The same effect was observed in 850 keV Ni implanted SiC with two different temperatures (RT and 450° C) and thermally annealed at 1000° C for 40 minutes. It has been found that the high-temperature implantation is effective in reducing the amorphization process in the sample. In Figure.1.4 comparison between the damage introduced by a room

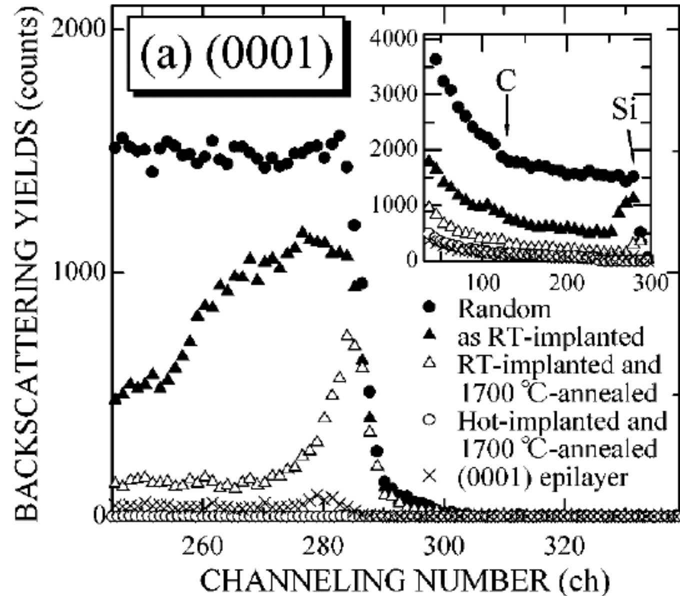


*Figure. 1.4. RBS-C spectra of $P^+$ implanted 6H-SiC samples at room temperature and at 800 °C [35].*

temperature $P^+$ ion implantation and by a 800° C implantation into 6H-SiC is shown after annealing at 1700°C for 30 minutes in argon[34] .The room temperature ion implantation process creates a nearly amorphous layer. Severe damage persists even after a 1700°C annealing. In the case of hot ion implantation, the same annealing at 1700° C restores the lattice order to the virgin value.

In addition to ion implantation performed at elevated temperatures, thermal annealing is normally performed after ion implantation, which serves the dual purpose of repairing defects and activating dopants. Although a considerable part of the implantation-induced damage can be removed by annealing at $1200^o$ C, annealing at temperatures in excess of 1600 $^o$C should be performed because of the high bonding strength of the SiC lattice[35]. After bombarding the target surface with ions, the implanted ions predominantly occupy interstitial lattice sites which affect the electrical properties of material. The electrical activation of the implanted ions, via, the incorporation of dopants into proper lattice sites known more formally as substitutional dopant incorporation, is performed by thermal annealing of the wafer. Several papers about the annealing of damage introduced by ion implantation in silicon carbide have been published [21, 33, 36-45]. Table A.1 in Appendix A summarizes some of these results.

Miranda et al [38] studied Fe implantation in 6H–SiC at different temperatures and fluences. The damage formation and annealing was studied by RBS/C. The authors found that amorphization is avoided by implanting at temperatures above 250 $^o$C and after the annealing at 1000 $^o$C, a maximum fraction of 75%, corresponding to a total of $3.8\times10^{14}$ $Fe^+/cm^2$, was measured in regular sites. Also, Fe implantation in 6H–SiC at $550^o$ C and integrated fluence of $2.2\times10^{16}$ ions/cm$^2$ has been investigated by Dupeyrat et al [21].

However, the authors found that the substitutional fraction of Fe on Si-site reduces down to zero after thermal treatments with a short-range Fe atoms migration leading to the formation of crystalline Fe-rich nanoparticles.

It has been shown that defect annealing is not a simple process, but it depends on the implantation details like implantation temperature, implantation method, dopant concentration, type of defects, annealing method and annealing temperature. Experimentally, the annealing of vacancies has been studied since decades ago, based on their EPR signals. Such studies resulted in an annealing temperature of $500^o$ C for carbon vacancies ($V_C$) and of $750^o$ C for silicon vacancies ($V_{Si}$) in as-irradiated samples. These values are valid, however, only in the presence of self-interstitials, when the annihilation of vacancies can occur by recombination.

In cases where only out-diffusion of vacancies is relevant, $V_{Si}$ disappears above $1400^o$ C and $V_C$ can still be detected at temperatures as high as $1600^o$ C [45]. Traditionally, post-implantation annealing of SiC is performed in either resistively or inductively heated, high-temperature ceramic furnaces, since temperatures greater than $1600^o$ C are required.

## 1.3 Models describing magnetism in DMS

The mechanisms responsible for ferromagnetism in DMSs, particularly early on, have not been fully understood and appreciated. While the magnetic properties can be successfully calculated by *ab initio* methods and many calculations for such systems have been performed, the physical understanding of the exchange mechanisms involved is a very delicate and difficult problem, since no simple and elementary magnetic interaction exists, such that a multitude of mechanisms can lead to ferromagnetism or anti-ferromagnetism and some of them might even act simultaneously. The basic model for DMSs is of a magnetically inert host semiconductor doped with localized spins, which may then be doped with electrons or holes. The introduction of TM in a semiconductor material such as SiC creates local moments. The magnetically ordered structures are the results of direct or indirect interactions between the local moments in sites or delocalized electronic moments in crystal. In the following we will briefly describe the three main exchange mechanisms which are most frequently observed in local moment systems.

- **Direct exchange**

This interaction is the direct consequence of the Pauli exclusion principle and depends strongly on the overlap of the participating wave functions. It is a function of distance; for small interatomic distances, antiferromagnetic coupling occurs, with increasing distance, ferromagnetic state becomes favorable and for very large distances the coupling vanishes and paramagnetism is present.

- **RKKY exchange**

RKKY indirect exchange interaction (after Rudermann, Kittel, Kasuya and Yosida) takes over at distances beyond a few atomic spacing. It is mediated by the conduction

electrons(s, p). It becomes efficient when a high concentration of free carriers is present such as in metals for which it was developed.

- **Super-exchange**

Super-exchange describes the interactions between moments on ions too far apart to be connected by direct exchange, but coupled over a relatively long distance through a non-magnetic material. For example, the interaction between magnetic transition metal ions in oxides can be mediated by an intermediate Oxygen.

- **Double exchange**

It couples magnetic ions by virtual hopping of the 'extra' electron from one ion to the other through interaction with p-orbitals. There are basic approaches to understand the magnetic properties of dilute magnetic semiconductors. We will summarize them as follows:

### 1.3.1 Mean Field Theory

The first model is based on mean field theory which originates in the model of Zener[46]. The theories that fall into this general model implicitly assume that the dilute magnetic semiconductor is a more-or-less random alloy. In another word; the doping atoms will substitute randomly for the lattice constituents. Within these theories, there are differences in how the free carriers are assumed to interact with localized spins. The three important ideas behind the model are:

1- In an isolated atom, the lowest energy state is given by the electronic state where an incomplete d-shell has the highest spin - meaning that all the spins are aligned.

2- The exchange integral between d-shells of adjacent atoms always leads to anti-ferromagnetic order.

3- The spin of an incomplete shell is strongly coupled to the conduction electrons/holes. When this coupling dominates over the direct exchange, ferromagnetism is made possible.

The net spin coupling energy in such a system is a combination of the three above terms. In Zener model, the direct interaction between d shells of the adjacent Mn atoms (super-exchange) leads to an antiferromagnetic configuration of the d shell spins because the Mn-d shell is half-filled. On the other hand, the indirect coupling of spins through the conduction electrons/holes tends to align the spins of the incomplete d shells in a ferromagnetic manner. It is only when this dominates over the direct super-exchange coupling between adjacent d shells that ferromagnetism is possible. Accordingly, the mean-field approach assumes that ferromagnetism occurs through interactions between the local moments of the Mn atoms mediated by free holes/electrons in the material. The spin-spin coupling is also assumed to be a long-range, allowing the use of a mean-field approximation.

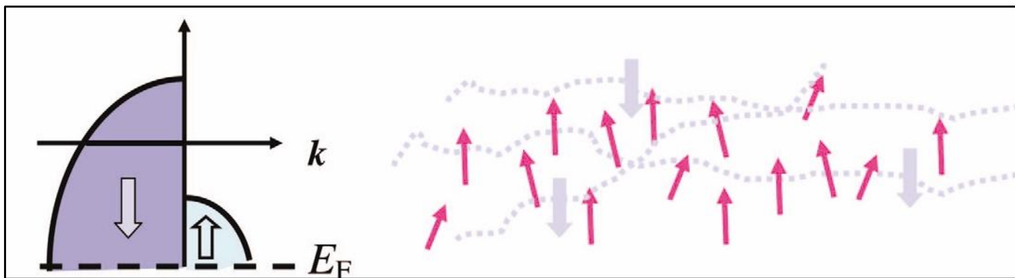


*Figure.1.5. Representation of carrier-mediated ferromagnetism in p-type DMS [46]. A model proposed originally by Zener for metals. Owing to the p-d exchange interaction, ferromagnetic ordering of localized spins (red arrows) leads to spin splitting of the valence band. The redistribution of the carriers between spin subbands lowers the energy of the holes, which at sufficiently low temperatures overcompensates an increase of the free energy associated with a decrease in Mn entropy.*

Dietl et al. [47] have applied Zener's model for ferromagnetism, driven by exchange interaction between carriers and localized spins, to explain the ferromagnetic transition temperature in III–V and II–VI compound semiconductors. The theory assumes ferromagnetic correlations mediated by holes from shallow acceptors in a matrix of localized spins in a magnetically doped semiconductor (Figure.1.5). Specifically, Mn ions substituted in group II or III site provide the local spin. In the case of III–V semiconductors, Mn also provides the acceptor dopant. High concentrations of holes are believed to mediate the ferromagnetic interactions among Mn ions. In this model the d level of Mn energy lie within the top of the valence band or the bottom of the conduction band.

### 1.3.2 Impurity Band Model

This model was proposed to explain the magnetic behavior of (Ga,Mn)As [48]. According to the mean field Zener model, the ferromagnetism in (Ga,Mn)As is mediated by extended hole states with the Fermi energy located in the valence band. That means $T_C$ increases monotonically with both the effective Mn concentration and the hole density. However, the electronic structure calculations using first principles method[49] have argued that ferromagnetism in (Ga,Mn)As is determined by impurity-derived state. Dodrowolska et al. [48] studied the relationship between $T_C$ in Mn doped GaAS and two key parameter; the hole density and the magnetically active Mn concentration. They concluded that $T_C$ does not scale as predicted using Zener model. Rather, they argue that the location of the Fermi level within the impurity band derived from the Mn dopant plays a crucial role in determining the $T_C$ through the degree of localization of the impurity band holes. When the Fermi level is near the top or the bottom of the impurity band, the DOS is lower and

the states becomes localized, suggesting insulating sample with low $T_C$. If the Fermi level lie near the middle of the impurity band, $T_C$ will increase because the states are extended. According to this model, higher values of $T_C$ can be achieved by understanding the role of Fermi energy. For example, controlling the concentration of Mn doping can be used to engineer the location of the Fermi level within the impurity band to best advantage.

### 1.3.3 Bound Magnetic Polaron (BMP)

In addition to the models mentioned above, an alternative model considers whether ferromagnetic ordering of the Mn moments could originate from carriers (holes) that are present in the material, but localized at the transition-metal impurity. Furthermore, ferromagnetism in DMSs has been accounted for by the formation of bound magnetic polaron (BMP). A bound magnetic polaron (BMP) is a collection of electrons (or holes) bound to impurity atoms through exchange interactions within an orbit [50]. These interactions can render carriers parallel or anti-parallel to the magnetic impurity, depending upon the system. These two configurations differ in energy, and this results in a non-zero spin flip energy that is a characteristic of BMPs. The net energy of the system can be lowered if the ions are aligned parallel to each other, since they all interact with carriers the same way.

The basic idea is schematically illustrated in Figure.1.6. The localized holes of the polarons act on the transition-metal impurities surrounding them, thus producing an effective magnetic field and aligning all spins. As temperature decreases, the interaction distance (boundary) grows. Neighboring magnetic polarons overlap and interact via magnetic impurities forming correlated clusters of polarons.

The polaron model is applicable to both p- and n-type host materials [51]. Even though the direct exchange interaction of the localized holes is antiferromagnetic, the interaction between bound magnetic polarons may be ferromagnetic for sufficiently large concentrations of magnetic impurities.

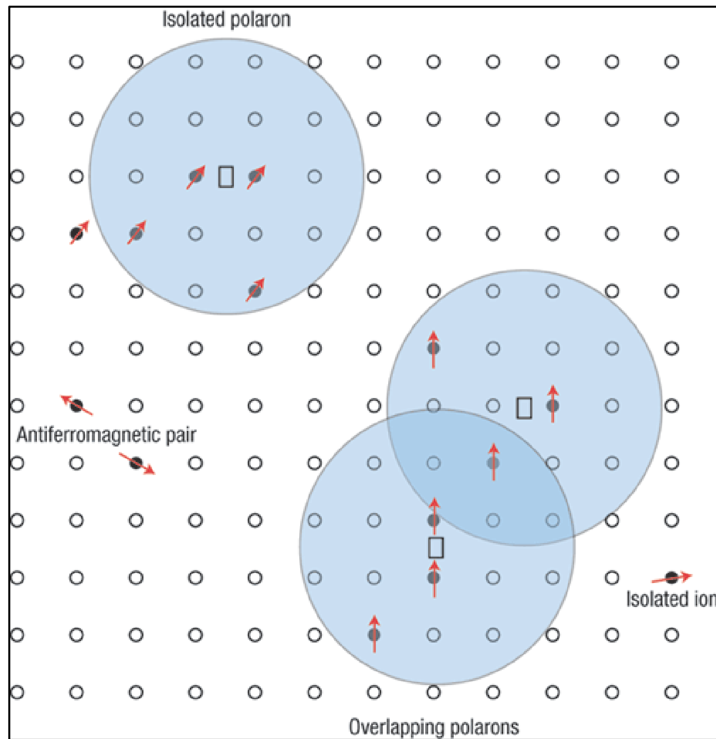


Figure 1.6. Representation of Magnetic Polarons in a semiconductor lattice [52].

In this work we report on Mn implantation and post implantation annealing in 6H-SiC. The dissertation is divided into four main chapters. Chapter two explains briefly the general theory behind implantation and the method of implantation in SiC. The chapter also covers the different experimental techniques used to characterize the structure and magnetic properties of the implanted samples. The characterization techniques include High resolution X-Ray Diffraction (HR-XRD) technique, Rutherford Backscattering and Channeling Spectroscopy (RBS/C), micro Raman Spectroscopy (μRS) and the superconducting quantum interference device (SQUID). In addition to experimental techniques, chapter two explains briefly the *ab-initio* calculations method that have been used to study the magnetism of Mn implanted SiC.

The results and discussions are reported in chapter three, which is divided into two main parts: the first part treats the structural and magnetic characterizations of the as-implanted and annealed samples, while the second part reports *ab-initio* calculations results and correlates the theoretical and the experimental results.

Chapter four will conclude on the results and draw some perspectives.

# Chapter 2. Methodology

This chapter is divided into three main parts. In the first part, we briefly explain the ion implantation process that has been used in this thesis. The second part contains the experimental techniques that have been used to determine the structural and magnetic properties of the implanted samples. The last part describes *ab-initio* calculations techniques that have been used to understand the experimental results. The experimental and theoretical works were performed at five different facilities:

- The ion implantation of stable samples of 6H-SiC with Mn was performed at LMP – CNRS lab at Poitiers University (France). The structural characterization with High Resolution X - Ray Diffraction (HRXRD) was done in this laboratory.
- The structural damage characterization with Rutherford backscattering and channeling spectroscopy (RBS/C) was performed in CSNSM lab in Orsay (France).
- The Micro Raman Spectroscopy (µRS) was conducted at LSPM lab of Paris 13 university (France)
- The magnetic characterization was carried out by using two techniques: Vibrating sample magnetometry (VSM) at Sultan Qaboos University (SQU) and SQUID magnetometry at CAPMAG/LLB lab of CEA-Saclay (France).
- Electrical characterization using Hall effect measurements was performed at SQU (Oman).
- *Ab-initio* calculations were carried out using the high performance computing (HPC) facility at SQU (Oman).

## 2.1 Ion implantation technology in SiC

### 2.1.1 Ion implantation

To obtain SiC based DMS, TM materials such as (Ni, Co, Fe, Mn…) have to be added to SiC polytypes. Contrary to the conventional Si-based semiconductor processing, the doping of SiC cannot be performed by thermal diffusion because of very low diffusion coefficients of dopants [30]. Considerable thermal diffusion can be achieved only above 2000 $^{o}$C that is close to the decomposition and phase transition temperature for SiC. Due to this limitation nowadays ion implantation to high fluences is the only accessible selective doping technique for SiC. Ion implantation means that electrically accelerated energetic ions are shooted into the crystal with energy range 100 keV–1 MeV.

Figure (2.1) shows a schematic representation of the complete ion implantation set up.

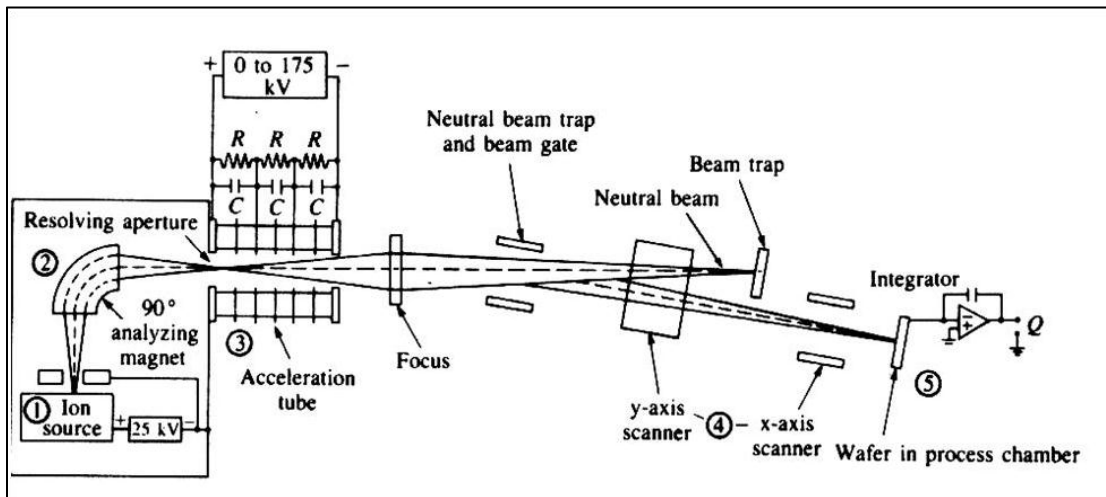


Figure.2.1. Schematic of an ion implanter showing (1) ion source, (2) mass spectrometer, (3) ion electrostatic accelerator (4) beam scanning system and (5) end station, where the target is mounted [53].

The principle is simple: atoms or molecules are ionized in an ion source and accelerated by an electrostatic field to energies between a few thousand electron Volts (keV) and several million electron Volt (MeV). Subsequently, the ions are separated by mass, using

an analyzing magnet. After passing through quadruple magnets for focusing, they are implanted into the desired material. The whole implantation process is executed in high vacuum (~ $10^{-7}$ mbar). Figure (2.2) shows some parts of the ion implanter at CSNSM-CNRS lab where the ion implantation takes place.

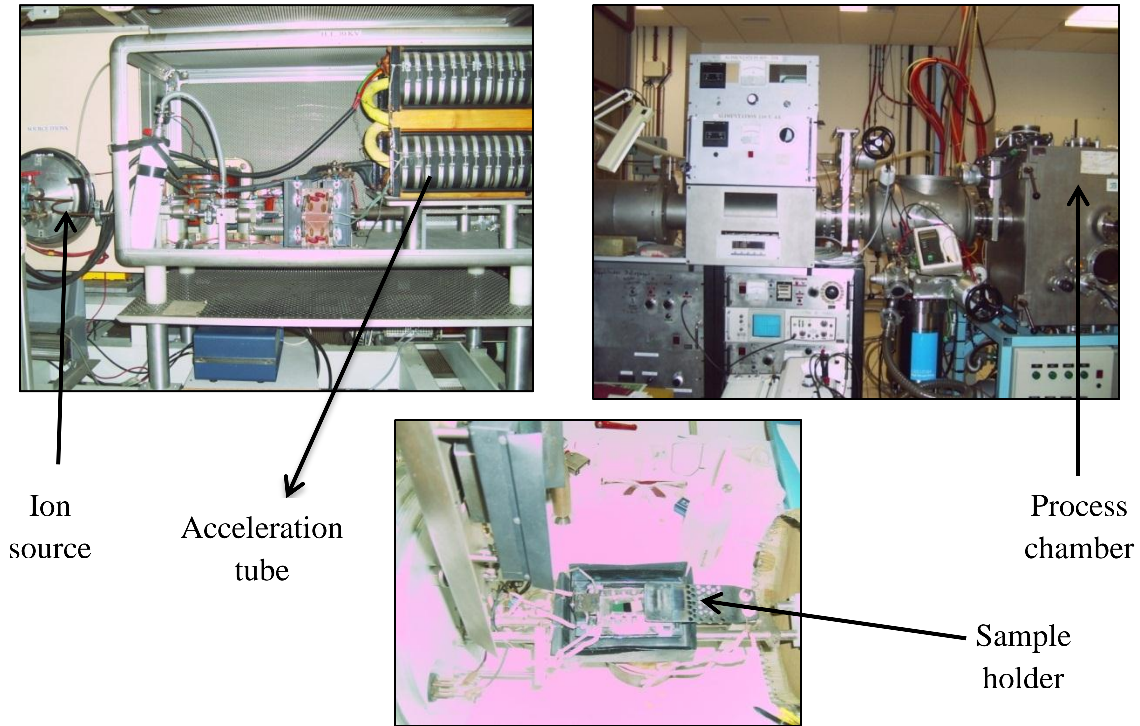


*Figure. 2.2. Some parts of the Ion implanter at CSNSM-CNRS lab.*

Ion implantation process allows the control of doping concentration and doping profile and as a thermally non-equilibrium process, has the advantage that basically all stable elements of the periodic table can be implanted.

However, as a disadvantage, ion implantation causes damage to the crystal structure, depending on the ion mass, ion energy, the implanted fluence and the fluence rate, temperature, and the orientation of the ion beam with respect to the crystallographic axis of the semiconductor.

The existence of inequivalent lattice sites in different polytypes of SiC gives rise to a large variety of possible defects, as mentioned in chapter 1. Among these are the point defects which can be classified as follows:

- Vacancies: the absence of an atom at its lattice site.
- Interstitial: the presence of an atom in a site that should be unoccupied. The interstitial atom can be the same species as the host lattice, and then it is called as self-interstitial, or a foreign atom, then it is called interstitial impurity.
- Antisite: an atom of one sublattice is placed in the other sublattice. These could be silicon antisite ($Si_C$) or carbon antisite ($C_{Si}$) in the case of SiC.
- Impurity, a foreign atom, occupying a regular lattice site. For instance, an aluminum atom in Si site ($Al_{Si}$, which acts as an acceptor), or a nitrogen atom in C site ($N_C$, which acts as a donor).
- a Frenkel pair is formed when a vacancy is located close to a self-interstitial.

A schematic representation of each type of defect is shown in Figure (2.3).

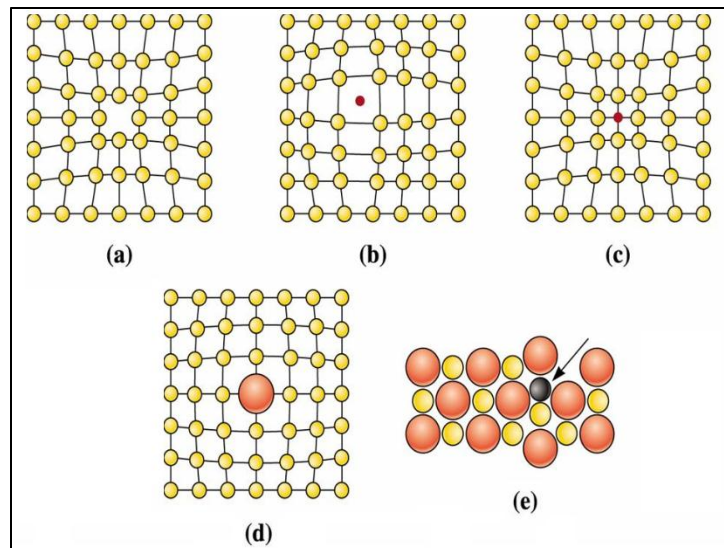


*Figure. 2.3. Point defects: (a) vacancy, (b) interstitial atom, (c) small substitutional atom, (d) large substitutional atom, (e) Frenkel defect–ionic crystals. All of these defects disrupt the perfect arrangement of the surrounding atoms* [54].

### 2.1.2 Physics of ion penetration in solids

In ion implantation, the energetic ion penetrates the material and loses energy in small interactions with electrons or nuclei, slows down and deviates from its original trajectory. It also undergoes major interactions such as large angle scattering, ionization, atomic displacements or sputtering (the ejection of atoms at the surface of the host material). The interaction of the charged ions with materials can be classified as follows:

- Inelastic collisions with the electrons of the target material. These occur when the energy of the ion matches the characteristic energy of atomic energy levels. The energy is lost in the excitation or ionization of the atoms.
- Inelastic collisions with the atomic nuclei. These interactions are the least common since they require very high energies.
- Elastic collisions with bound electrons are only important for very low energies (<1 keV, depending on the ion and target masses).
- Elastic collisions with the atomic nuclei. For small impact parameters, the incident ion undergoes a major change in direction and part of the kinetic energy of the ion is transferred to the atoms involved in the collision.

From the above discussion, it is obvious that the main loss of ion energy is due to the inelastic collisions with electrons and elastic nuclear collisions. Hence, the slowing down process is governed by two mechanisms, electronic and nuclear stopping, and characterized by the stopping power dE/dx (the energy loss per unit distance). The total stopping power can be written as the sum of both electronic and nuclear stopping powers as [55]:

$$\frac{dE}{dx} = \left(\frac{dE}{dx}\right)_n + \left(\frac{dE}{dx}\right)_e \qquad (2.1)$$

The subscripts n and e denote the nuclear and the electronic losses respectively. The nuclear energy loss is the mechanism responsible for lattice disorder through the displacement of atoms, whereas electronic collisions involve smaller energy losses and negligible deflection of the incident particle with almost no atomic displacement. The nuclear energy loss predominates for low energies and high mass of the incident ion while electronic loss is dominant for high energies and low masses (see Figure. 2.4).

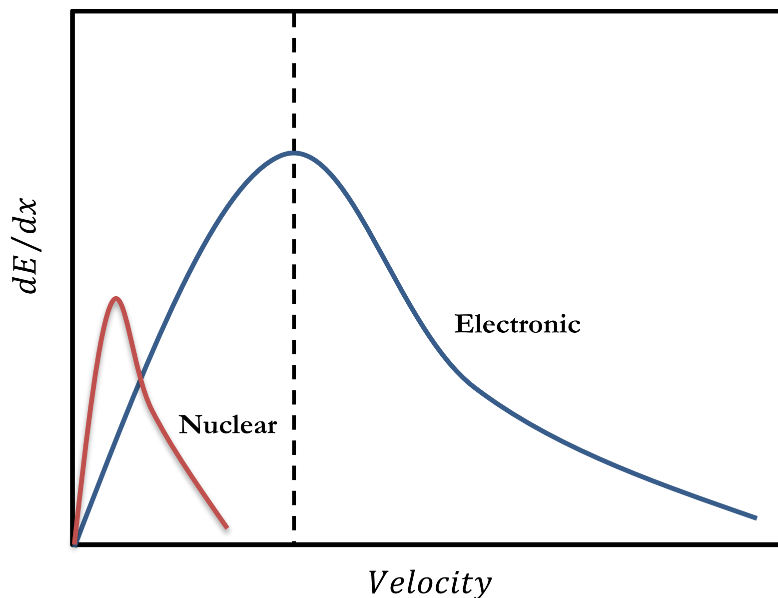


*Figure. 2.4. Schematic graph of typical electronic and nuclear energy loss as a function of velocity.*

Since the implantation process involves a huge number of events, statistical approaches can be used to describe the final distribution of the implanted atoms. The range R of an ion is the total distance that the atom travels before coming to rest. Figure (2.5) illustrates the path of a particle as it comes to rest within the target material. The ion does not travel in a straight line due to collisions with the target atoms. The ion's net penetration within the solid, which is the distance measured perpendicular to the surface of the sample to the

point where the particle comes to rest is called the penetration depth $R_p$. The mean projected range is the most probable location for an ion to come to a rest:

$$R_p = \sum_i x_i / N \qquad (2.2)$$

Where $x_i$ is the projected range of the i-th ion in the incident direction, and N is the total number of implanted ions.

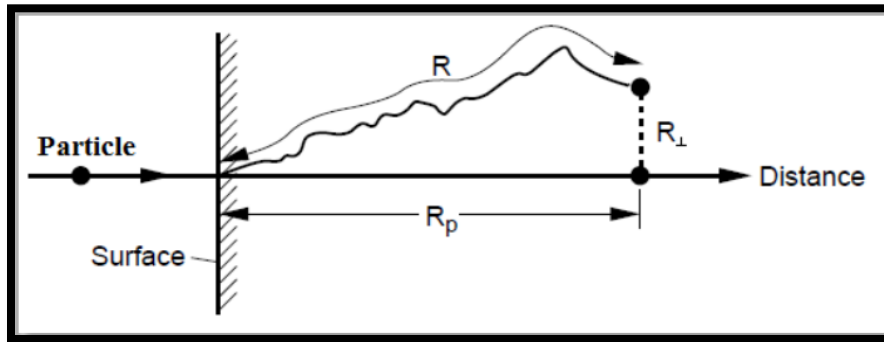


*Figure. 2.5. A particle incident on a solid penetrated with a total path length R, resulting in a projected range $R_p$, along the direction parallel to the incident ion [55].*

### 2.1.3 Simulation of ion implantation profiles

A calculation of implantation distributions can be made either by running computer programs which perform Monte-Carlo simulations of the ion ranges or by calculating the ion distribution functions using fitting parameters.

A transport calculation was developed in detail by Ziegler and Biersack [56] in the PRAL (Projected Range Algorithm) code, which is part of the SRIM (Stopping Ions and Ranges in Matter) software package. This kind of approach allows the calculation of a series of histories, following the paths of the ions in the target material. The particle is assumed to change direction in binary collisions with target atoms and to move in straight paths between the collisions. The ion energy reduces due to nuclear and electronic energy losses, and the history ends when the energy drops below a specified value or when it

leaves the target. The target is considered to be amorphous with atoms at random positions and hence the crystalline structure of the target lattice is ignored.

TRIM (Transport of Ion in Matter) will accept complex targets made of compound materials with up to eight layers, each of different materials. It calculates both the final 3D distribution of the ions and also all kinetic phenomena associated with the ion's energy loss: target damage, sputtering, ionization, and phonon production. All target atom cascades in the target can be followed in detail. The programs are made such that they can be interrupted at any time, and then resumed later. Plots of the calculation may be saved, and displayed when needed.

Another advantage is that the implantation can be simulated for a wide range of targets, including composite materials and layered structures [56, 57].

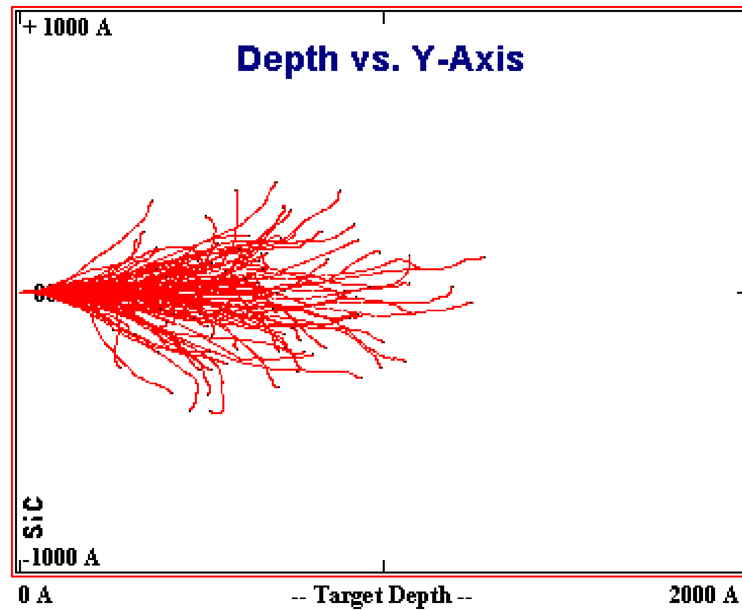


*Figure. 2.6. Simulated penetration trajectories of 10,000 electrons inside SiC for 170 keV.*

## 2.2 Experimental Techniques

The objectives of these techniques are to characterize the structural, electrical and magnetic properties of Mn implanted 6H-SiC samples. As was illustrated in the previous section, the ion implantation is known to create large amount of defects in the crystal which affect the electrical and magnetic properties of the samples. So, we will start first describing the techniques used in this thesis to quantify the lattice damage. We used two complementary techniques; Rutherford backscattering and channeling spectrometry (RBS/C) and High resolution X-ray diffraction (HR-XRD). The amount of disorder, the Mn depth profile and Mn concentration in the implanted samples were deduced from RBS/C experiment. The strain induced in the samples due to the implantation was deduced from HR-XRD experiments. After the structural characterizations, the magnetic characterization techniques will be described. VSM and SQUID techniques were used to characterize the magnetic properties of the implanted samples.

### 2.2.1 Rutherford Backscattering and Channeling Spectrometry (RBS/C)

Rutherford backscattering spectrometry combined with channeling (RBS/C) is a powerful technique to determine the composition, thickness and crystalline quality of thin film materials, as well as the lattice location of impurities in crystals. In this thesis, RBS/C is mainly used to evaluate the induced disorder in 6H-SiC lattice upon Mn implantation, and its recovery after annealing. RBS has its roots in the famous experiment by Geiger and Marsden, where alpha particles were found to be backscattered from a thin gold foil [58]. This experiment has been explained by E. Rutherford in 1911 for the first time [59].

In RBS experiments, accelerating light ions (most commonly $^{4}He^{+}$) hit their target and lose energy by interacting with the material under investigation. When these ions reach the target, they mainly suffer inelastic collisions with the target electrons, as described in section 2.1.2. However, at a certain instant along their inwards trajectory they can experience a head-on nuclear collision with the nuclei of the target atoms. A small percentage of these ions will be backscattered. Placing a particle detector in the backscattering direction allows counting the number, and measuring the energy of the backscattered ions. A silicon surface barrier detector is placed in this backscattering region and particles which collide with it generate an electrical signal proportional to the energy of the ion. The signal from the detector passes through an amplifier, coupled to a multichannel analyzer, which divides the selected energy range up into smaller channels each spanning a range of a several keV.

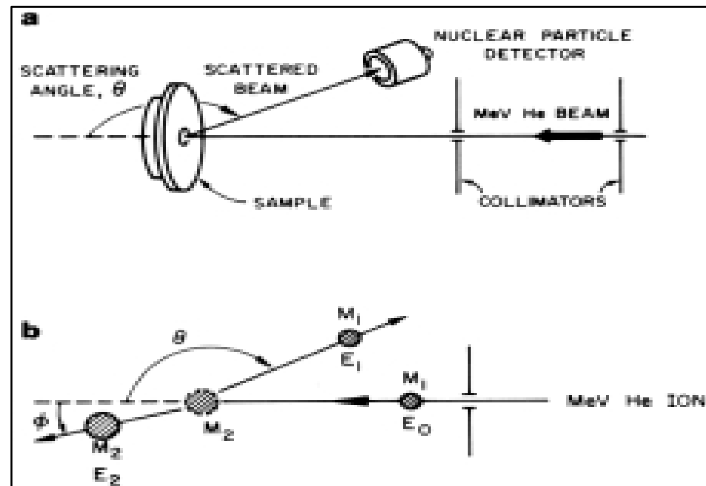


*Figure. 2.7. a) Experimental setup employed in RBS* [60]*, b) Schematic illustration of the RBS principle from the point of view of a classical two-particle collision event* [61]*.*

The number of ions entering the detector in each energy range is summed during the measurement thereby generating an RBS spectrum which is simply the number of backscattered particles as a function of energy. This energy contains information about

(1) the mass of the target atoms and (2) at what depth the collision took place (from the amount of electronic energy loss).

### 2.2.1.1 Channeling and RBS/C

When the trajectory of an incoming positive ion is aligned with a crystallographic axis or plane of a single crystalline target material, the repulsive force between the ion and the positively charged nuclei of the regularly-spaced atomic rows and planes of the single crystalline material will steer the incoming ion in the open space between the rows and planes through many small-angle interactions. This effect is called channeling and is presented schematically in Figure (2.8).

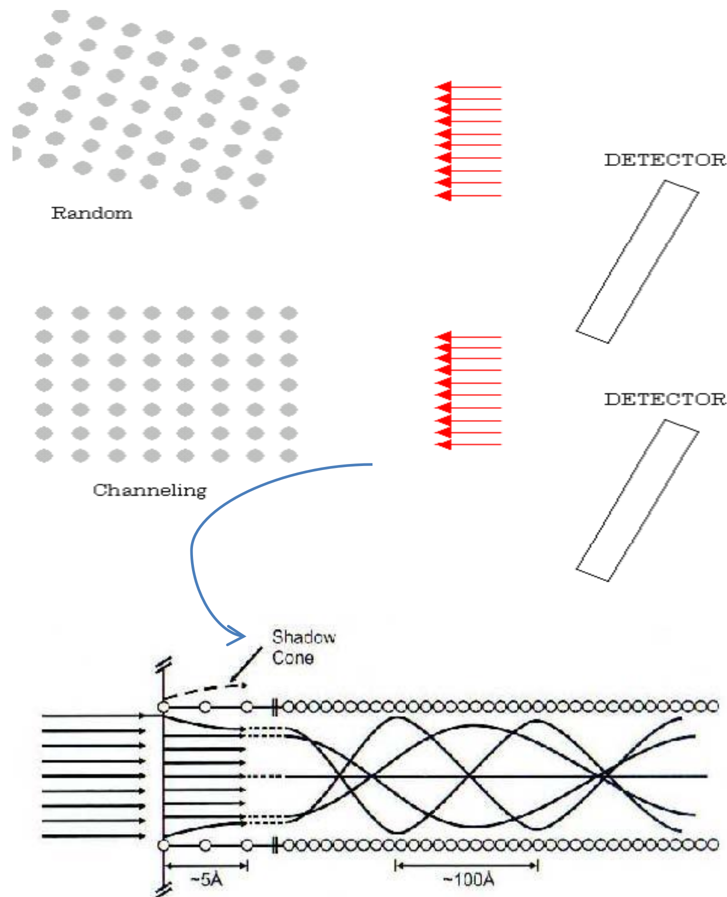


*Figure.2.8. Schematic representation of the channeling effect: incoming positively charged ions aligned with a crystallographic axis of the target material will be steered in between the rows and planes of the single crystalline material* [61].

The incoming ion stays in this open channel until it encounters an obstruction or until it loses almost all of its energy through electronic stopping. However, in order to maintain the channeling motion, the ion must not approach the rows of atoms too closely. As such, there is a critical angle above which ions entering the crystal will no longer be channeled. This channeling effect has been theoretically described by Lindhard [62], whose work is still the basis of the analysis of modern channeling data. More information about channeling can be found in several books and articles [61-63].

When using RBS in channeling geometry (RBS/C), it becomes possible to obtain structural information about the lattice. As mentioned above, when the beam of incoming He ions is aligned with a perfect single crystal axis, the channeling ions will not be backscattered and will continue to penetrate the material until they lose all their energy. However, when structural defects are present, e.g. after ion implantation, such as self-interstitials, interstitial impurities or more extended defects such as dislocations, the channels become obstructed, resulting in an increased amount of He ions that are backscattered. In this way, the backscattered yield provides information about the crystalline quality of the target material.

By using appropriate tools to perform fittings of RBS spectra one can deduce very relevant informations about the sample in study. In particular, it is possible to deduce the sample elemental composition (which elements?), the distribution of elements through the material (where?) and the quantities of those elements in the sample (how much?). These parameters are deducible from three physical concepts, fundamental for this analytical technique: the kinematic factor; the stopping cross section; and the scattering

cross section. A more detailed description on these quantities and concepts can be found in appendix B.

#### 2.2.1.2 Analysis of an RBS/C spectrum

As expected, the backscattered yield of the random spectrum is much higher than the yield of the channeled spectrum. The increased yield of backscattered ions, around 800 KeV in the channeled spectrum in figure(2.9) is referred to as the surface peak. Even when the incoming ion beam is perfectly aligned with a single crystal, a fraction of the incoming ions will impinge on the crystal surface very close to a surface atom, resulting in a large repulsive interaction between the ion and the positive nucleus of the surface atom. These ions will be backscattered, which gives rise to the surface peak.

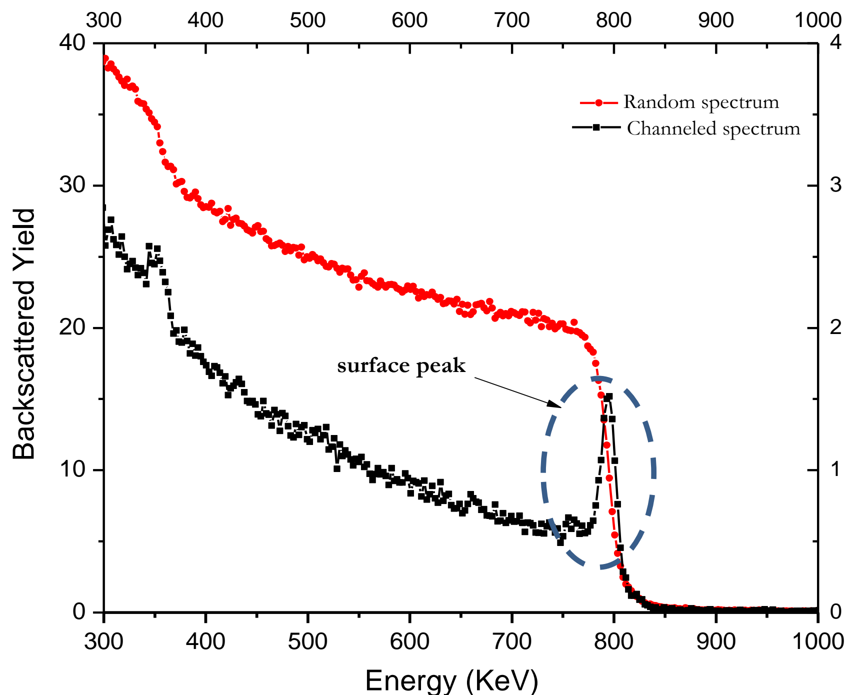


*Figure. 2.9. The random and channeled RBS measurements for virgin 6H-SiC sample.*

In order to quantify the defect density from an RBS/C experiment, it is important to note that there are two contributions to the amount of backscattered He ions: (1) A fraction of

the incoming ions collides directly with defects in the lattice crystal ($f_{def}$) and (2) a second fraction of ions will be dechanneled (scattered by displaced atoms over a small angle). As a consequence, these ions are no longer channeled and the atoms in the crystal act on them with random backscattering probability) ($f_{dech}$). By subtracting the fraction of dechanneled ions as a function of depth, from the total amount of backscattered He ions, it is possible to extract a quantitative profile of the amount of displaced target atoms.

In this work, the compositional depth profile was studied by Rutherford backscattering spectrometry (RBS) using a 1.4 MeV $4He^{2+}$ ion beam delivered by ARAMIS accelerator at CSNSM-Orsay (Figure 2.10). The recorded RBS spectra were processed by the McChasy Monte-Carlo simulation computer program [64].

**(a)**

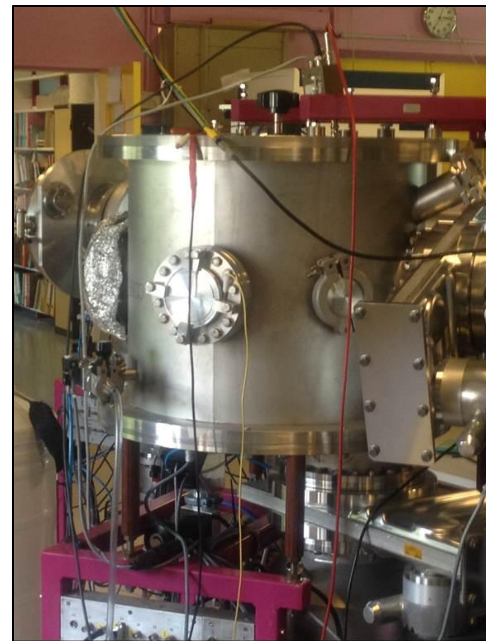

**(b)**

*Figure. 2.10. (a) ARAMIS accelerator in CSNSM lab, (b) the sample chamber.*

### 2.2.2. High-Resolution X-Ray Diffraction (HRXRD)

High-resolution X-ray diffraction (HRXRD) is a well-known method for measuring the composition and thickness of compound semiconductor materials. When dopants or impurities are added substitutionally to a single crystal, the lattice will be strained by the presence of the dopant atoms. The resulting change in lattice spacing due to strain can be detected by HRXRD.

X-rays are electromagnetic radiation with a wavelength between 0.5 and 2.5 Å. This makes them extremely useful for the determination of interatomic distances in a crystalline material, which are of the order of few angstroms. When X-rays are incident on a crystal, they will be scattered by the electrons in all directions. However, under certain geometrical conditions, constructive interference of the scattered X-rays occurs. This phenomenon has been described and explained by W. L. Bragg, resulting in his well-known law of diffraction.

X-rays impinge on the crystal planes at an angle $\theta$ with respect to the surface normal. The condition of positive interference is fulfilled when the scattered X-rays leave the sample at the same angle θ, as shown in Figure (2.11), and when the path difference between X-rays reflected from two different planes is equal to a multiple of the X-ray wavelength. This results in Bragg's law:

$$2d_{hkl}\, sin\theta = n\lambda \qquad (2.4)$$

Where n is the order of diffraction (an integer number 1,2,….), λ is the wavelength of the incident X-Ray, $d_{hkl}$ is the interplanar distance and $\theta$ is the Bragg angle .

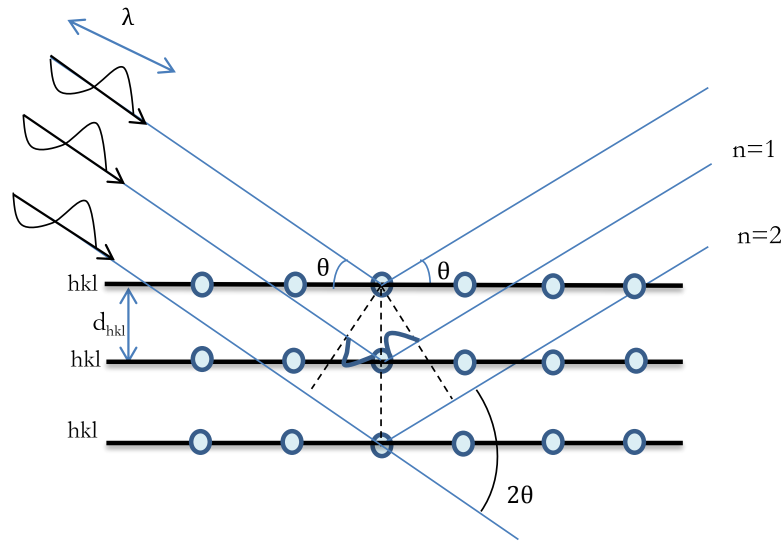


*Figure. 2.11. Diffraction of the X-ray beam at the atomic planes in the crystal.*

A 2θ-θ scan allows the determination of interplanar distance $d_{hkl}$. This distance is a characteristic for a crystal and 2θ-θ scans thus allow the identification of the crystalline phases in a thin film. In the symmetric 2θ-θ scan, the angle θ of the incoming beam with respect to the sample surface is varied while simultaneously keeping the detector at an angle of 2θ, with respect to the incoming beam (see Figure. 2.12).

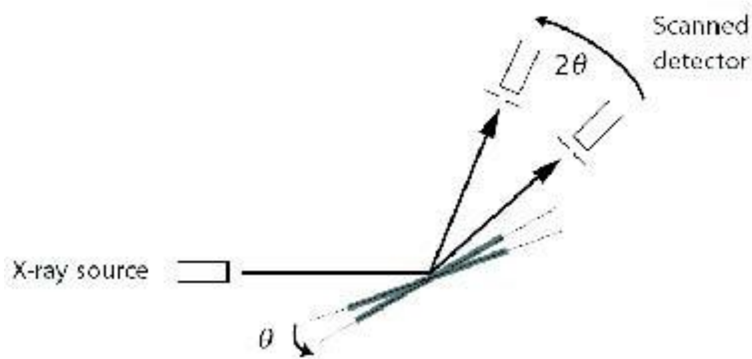


Figure. 2.12. Source, sample and detector configuration during 2θ-θ scan [65].

The value of the angular position θ at which the maximum of diffraction occurs can be replaced in Bragg's equation (2.4) to obtain the value of $d_{hkl}$. The incident beam first passes through a set of monochromating crystal to allow a certain value of wavelength,

and the exist-diffracted beam passes through a set of slits. In that case, one peak of high resolution XRD is obtained.

In this work, XRD measurements were conducted in the Bragg (reflection) geometry. Scans along the surface normal are obtained with a high resolution X-ray experimental setup: four-circles Seifert D3000 goniometer, using the Cu-$K_{\alpha 1}$ radiation ($\lambda$ =1.54 Å) with a vertical linear focus in combination with a two Ge (220) monochromator.

#### 2.2.2.1 Analysis of an XRD spectrum

In Figure 2.13, typical X-ray diffraction spectra of the (0006) planes of a virgin 6H-SiC crystal and a 80 keV Mn-implanted 6H-SiC sample to a fluence of $5\times10^{15}$ at/cm$^2$ are shown.

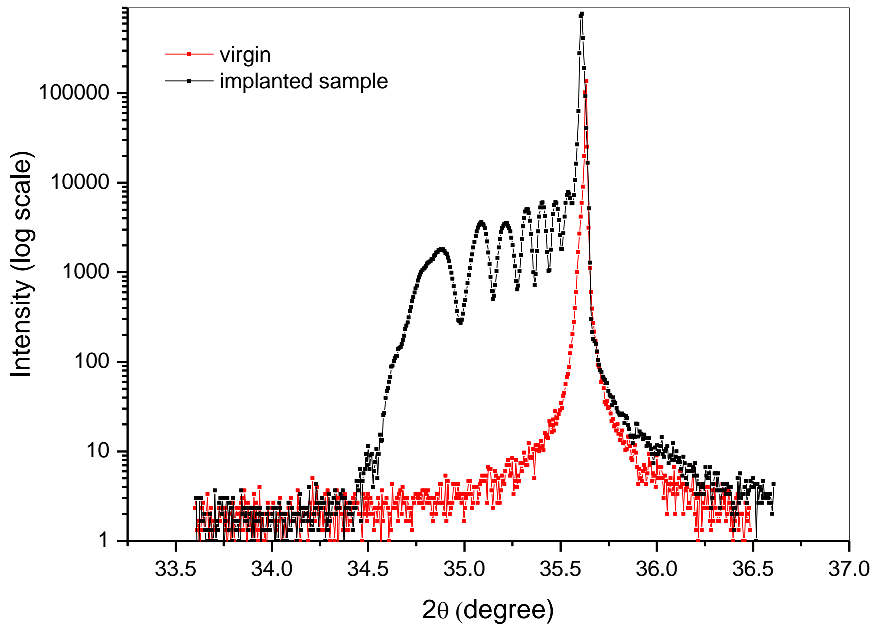


*Figure. 2.13. X-ray diffraction spectra of a virgin SiC sample and of a 80 keV Mn-implanted SiC sample to a fluence of $5\times10^{15}$ at/cm$^2$.*

It is clear from the figure that X-ray diffraction on a virgin 6H-SiC sample exhibits a single diffraction peak at a 2θ value of $35.6^{\circ}$ which corresponds to the bulk 6H-SiC.

As expected, the X- ray diffraction spectrum after ion implantation has extra features compared to the virgin sample, due to the implantation- induced strain.

It can be derived that ion implantation induces an expansion of the lattice in a direction perpendicular to the SiC surface. The cause of this expansion may be the heavy Mn ions which principally occupy substitutional Si or C sites after implantation or it can be due to the interstitial atoms (Si, C or dopant atom) in the SiC lattice. As a consequence, the strain distribution is expected to exhibit the same depth profile as the defect distribution.

The defects have a Gaussian distribution profile as obtained from SRIM. We can then expect that the lattice parameter to have its maximal value where the concentration of defects is higher. Also, a Gaussian distribution of lattice parameters in the implanted region can be assumed. Consequently, to such distribution of lattice parameter values, a similar profile of values for the Bragg angle will be associated, with the minimum value of θ corresponding to a maximum value of the lattice parameter. The diffraction intensity strongly depends on the lattice quality. A strongly disordered lattice will produce a less intense diffraction peak than that resulting from an expanded but still ordered crystalline lattice. However, the intensity of diffraction from the expanded lattice, will be considerably lower than that of the undamaged bulk material

The strain depth profiles was deduced from XRD patterns (Figure.2.13) using Bragg's equation (2.4) assuming the maximum strain occurs at the maximum defect profile. For the strain-free crystal, equation (2.4) can be written as:

$$2d_0 \sin\theta_0 = \mathrm{n}\lambda$$

When a strain in the plane normal direction $\varepsilon_n$ is applied to the crystal, the d-spacing changes from $d_o$ to d and equation (2.4) can be written as:

$$2d\sin\theta = n\lambda$$

The normal strain can then be given by the following relations based on the engineering strain:

$$\varepsilon_n = \frac{d}{d_0} - 1 = \frac{\sin\theta_0}{\sin\theta} - 1 \qquad (2.5)$$

where $\theta$ is the diffraction angle measured from strained crystal.

The strain calculation equation is obtained by taking the first derivative of the Bragg's equation (2.4).

$$2d\cos\theta_0\Delta\theta + 2\sin\theta_0\Delta d = 0 \qquad (2.6)$$

When both $\Delta d$ and $\Delta\theta$ are very small, we have

$$\varepsilon_n = -\Delta\theta\cot\theta_0 = -(\theta - \theta_0)\times\frac{1}{\tan\theta_0} \qquad (2.7)$$

## 2.2.3 Micro Raman Spectroscopy (μRS)

Raman scattering spectroscopy is another technique which employ light-matter interaction to probe certain materials properties. Specifically, Raman scattering measures the interaction of light *via* inelastic scattering from an incident laser beam of a material. One of the processes of inelastic scattering is to transfer this energy into lattice vibrations. The energy of these lattice vibrations is quantized (phonons) and function of

the local bonding and the atoms involved in the scattering. Thus, by measuring the energy transferred to or from phonons to photons, which is manifested as a Stokes or Anti-stokes shift in the inelastically scattered light source, valuable information regarding the quality of the crystal can be gained. These generally appear as a weak peak, several orders of magnitude weaker than the laser line, which must be filtered out in order to observe the Raman signal.

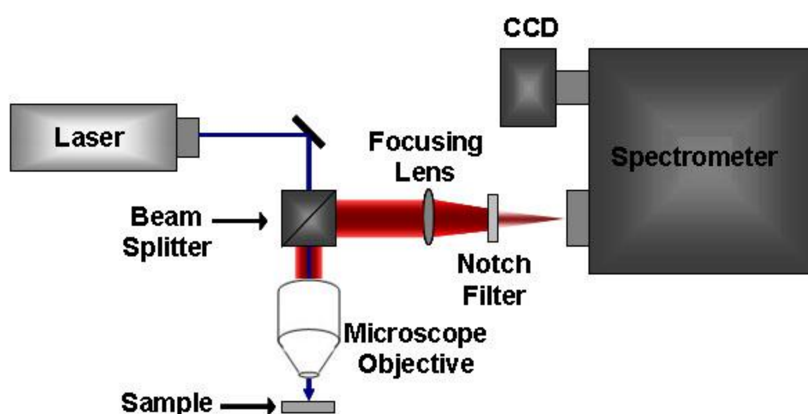


*Figure. 2.14. Schematic of a micro-Raman spectrometer where illumination and collection are performed through microscope objective.*

The modes that can be observed are highly sensitive to the polarization of the incident light and the orientation of the crystal upon which the laser light is incident. Raman spectroscopy measurements in this work were performed to determine the crystalline quality using a Renishaw micro-Raman system with a 488 nm excitation source.

### 2.2.4 Magnetometry techniques

Two magnetometry techniques were used in this thesis: VSM and SQUID measurements. These techniques give information about the magnetic response of a sample to an external magnetic field by measuring the magnetization or a quantity proportional to the magnetic moment.

#### 2.2.4.1 Vibrating Sample Magnetometry (VSM)

A popular method for determining the magnetic properties of a wide variety of magnetic systems is vibrating sample magnetometry (VSM). This technique is based on the induction of electrical signals by the oscillation of a magnetic sample inside a coil. The amplitude of the signal is proportional to the magnetic moment of the sample. The material under study is inserted in the sample holder which is situated between a pair of pick-up coils. The sample is vibrated at a fixed frequency when a DC magnetic field is applied. As a consequence, an AC voltage with the same frequency and proportional to the sample magnetization is induced in the coils. A lock-in amplifier is used to provide the frequency of vibrations and to detect the signal. Using the computer interface, the magnetic field and the signal proportional to the magnetic moment can be simultaneously recorded (hysteresis loops). A schematic representation of the VSM is given in figure (2.15). In order to infer the exact magnetic moment (m) from the measured signal, the system has to be calibrated with a sample with known magnetic properties, e.g. Ni. Inside the coils, a small cryostat is fitted to perform measurements at temperatures down to 4 K. Since VSM is an integral technique, the magnetic response of the substrate and the sample holder are also measured. Therefore, the measured paramagnetic effects are subtracted from the data.

In this work, we studied the temperature dependence of the magnetization at a constant field and the sample response to the variation of the external field at a constant temperature.

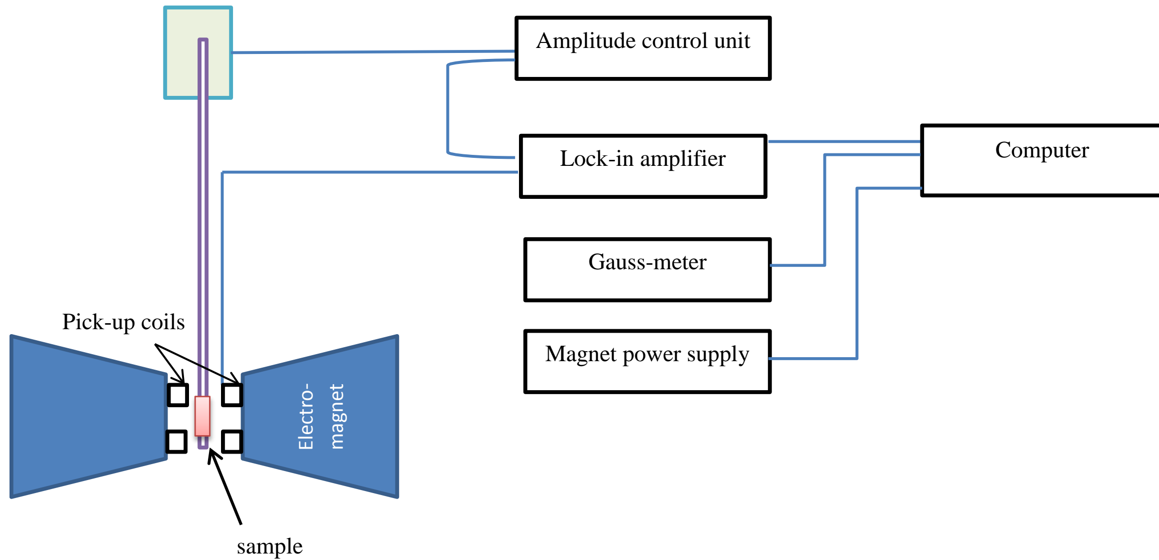


*Figure. 2.15. Block diagram of the VSM.*

### 2.2.4.2 SQUID Magnetometry

Because we are dealing with diluted magnetic semiconductors, the Mn concentration is very small to be detected with VSM technique especially for the low Mn fluences. More sensitive device is required in this case. SQUID is one of the most sensitive methods to detect magnetic fields.

As shown in figure 2.16, the central element of a SQUID consists of two superconductors separated by thin insulating layers to form two parallel Josephson junctions on a superconducting loop and biased by a direct current. Maintaining constant biasing current in the SQUID device, the measured voltage oscillates with the changes in phase at the two junctions, which depends upon the change in the magnetic flux. Counting the oscillations allows evaluating the occurring flux change. Functionally, the device acts as

a magnetic flux to voltage converter. This voltage is then amplified and read out by the magnetometer's electronics. The SQUID is the most sensitive flux detector known today, which has the flux-quantum-limited sensitivity [66].

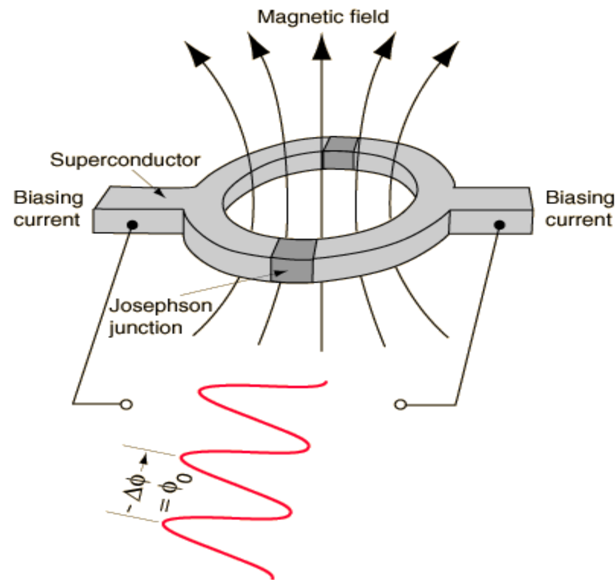


*Figure. 2.16. A scheme for a SQUID[66].*

In order to determine its magnetic moment, the sample is moved along the symmetry axis through the pick-up coils, and the resulting flux changes are recorded (DC-mode). The software fits the observed curve (which has to be symmetric around the coil center) with the expected curve of a dipole.

In this work, two kind of magnetic measurements were performed

1. Measurements of magnetization vs. temperature ($m(T)$curves).

2. Measurements of hysteresis: magnetization vs. field ($m(H)$ curves).

The SQUID measurements were done with temperatures ranging from 4 K to 250 K, and magnetic fields available up to 10 kOe. Samples are mounted within a plastic straw and

connected to one end of a sample rod which is inserted into the dewar /probe. The signal is fitted to an ideal dipole response using a non-linear least-squares routine. Figure 2.17 shows the SQUID system and the sample rod used in this thesis.

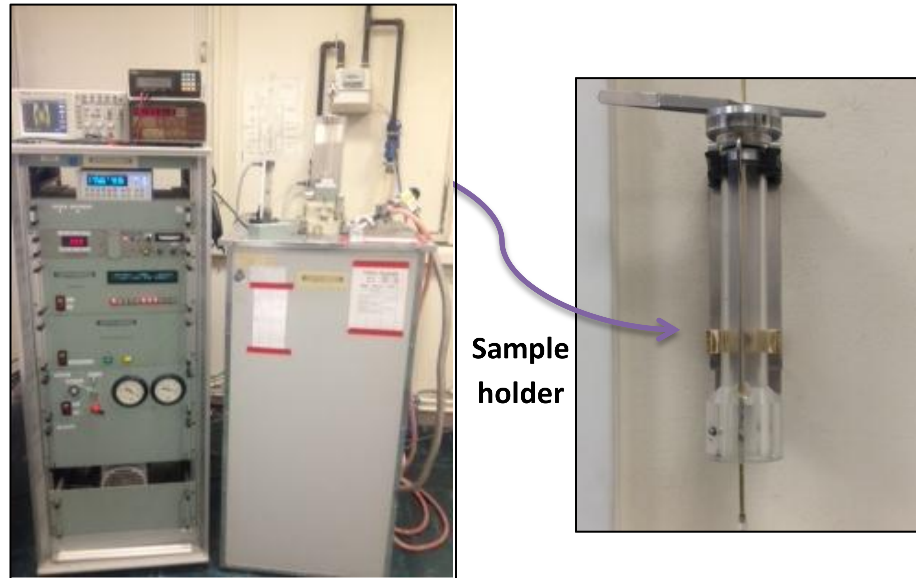


*Figure.2.17. SQUID magnetometer technique at CEA Saclay with magnified sample rod.*

### 2.2.5 Hall effect measurements

Resistivity, carrier concentration and carrier mobility are among the most important properties of semiconductor materials as far as device applications are concerned. Even if these quantities are only measured at a single temperature (e.g. room temperature), much information about the electrical properties of a material can be inferred. The electrical behavior of the SiC samples was studied using Hall effect measurements. We tried to study the effect of Mn implantation into 6H-SiC. As we know the intrinsic and extrinsic defects have a strong effect on the electrical properties of the semiconductors. Shallow electric defects have a strong effect on the carrier concentration while deep defects can indirectly affect the carrier concentration by acting as charge

trapping centers. Defects also have significant impact on the mobility of carriers. Hall effect measurements are powerful technique to measure the mobility, resistivity and carrier concentration of the semiconductor material. If in addition the temperature dependence of the carrier concentration is studied, further separation into various donor and acceptor contribution is possible.

The Hall effect arises from the interaction of charge carriers in a semiconductor with an applied magnetic field. Figure (2.18) shows a schematic representation of the setup, where a potential ($V_{app}$) and a magnetic field (B) are applied across a semiconducting samples along the orthogonal directions. An electron moving with a velocity $\vec{v}$, in the potential applied feels a Lorentz force given by:

$$F = e\overrightarrow{v \times B} \qquad (2.8)$$

Holes in the semiconductors experience a similar force along the opposite edges of the semiconductor leading to accumulation of charge carriers along opposite edges of the semiconductor. This, in turn, gives rise to electrostatic force, which at equilibrium, is equal and opposite the Lorentz force. Thus a potential develops along this direction, perpendicular to the applied voltage. This potential is known as the Hall voltage, and is given by:

$$V_H = \frac{IB}{nqd} \qquad (2.9)$$

Where, n is the density of charge carriers, q is the charge and d is the thickness of the film. The information about carrier type is contained in q.

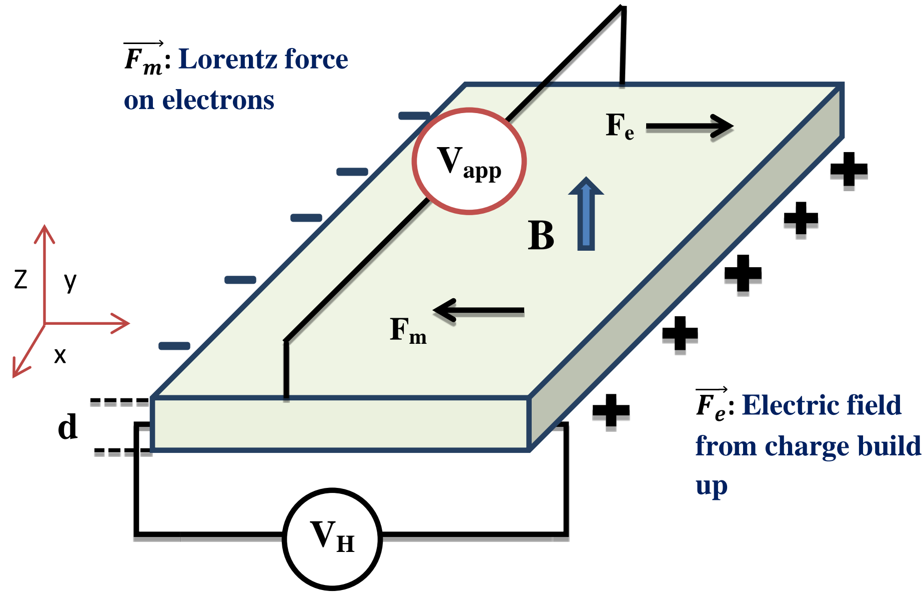


*Figure. 2.18. Hall Setup.*

The Hall coefficient $R_H$ is defined by:

$$R_H = \frac{1}{nq} \qquad (2.10)$$

This implies that the sign of $R_H$ is determined by the charge dominant carrier type, i.e. it is positive for holes and negative in the case of electrons.

In this thesis, we tried to measure the electrical properties of the Mn implanted 6H-SiC using Temperature Dependence Hall (TDH) system. The first step was the construction of the system at SQU, the schematic diagrams of which is shown in Figure (2.19). The TDH setup was designed and constructed around a few key components that were available. The main components of our Hall measurements setup are the current source, the magnet, the vacuum system and a suitable software.

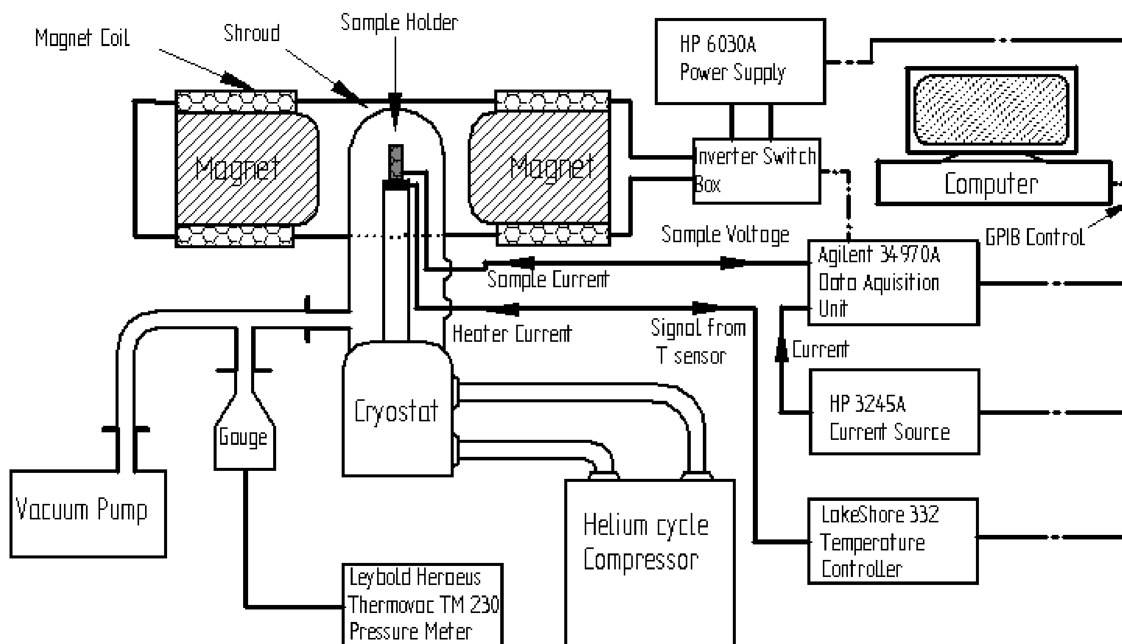


Figure.2.19 Schematic representation of the Temperature Dependent Hall setup [67].

An HP 6030A System power supply was chosen as a current source for the magnet. To obtain a magnetic field of 0.4T, a current of about 9A is sufficient. Since the power supply can apply a voltage in one direction, an inverting switch unit is needed so that the magnetic field can be inverted. To achieve the low temperatures needed for TDH measurements, a cryostat powered by a $N_2$ cycle compressor, was employed. The tip of the cryostat shaft was fitted with a Gold / Chrome (0.07% Fe) thermocouple which in turn was connected to a Lakeshore 332 temperature controller. A heating element at the tip of the shaft powered by the temperature controller provides the means for stabilizing the temperature at any set point in the 20 K to 370 K range. The cryostat is enclosed with a shroud and a pump is used to obtain vacuum. A specialized sample holder was fabricated to enable quick and convenient sample loading.

Two instruments were used to achieve the electrical measurements on the sample: An HP 3245A universal current source and a Agilent 34970A data acquisition unit. The former supplies the current necessary for Hall measurements while the latter is responsible for both creating the contact configurations and measuring the voltage.

All instruments except the power supply unit are controlled directly via a GPIB interface. Automation through the GPIB is controlled by a program written in LabView$^{TM}$.

## 2.3 *Ab-initio* calculations

To obtain complementary information about the lattice location of impurities in single crystals and the magnetic properties of the implanted SiC samples, we have performed *ab-initio* calculations. The calculations were carried out using the FP-LAPW method within Density Functional Theory (DFT), as implemented in the WIEN2k code[68]. In this section we will give a short description of density functional theory and the APW method.

### 2.3.1 Density Functional Theory (DFT)

The aim of this section is to describe the basic principles of *ab-initio* calculations. Such calculations allow us to investigate and to predict different electronic properties of solids. Progress in computer technology made it possible to investigate atomic systems which contain several hundred atoms. That is why the *ab-initio* calculations became so popular in the scientific community and they are widely used as a complimentary component of experimental investigations. The electronic structure of a crystal can be calculated using a multi-particle Hamiltonian in the Schrödinger equation [69]:

$$\boldsymbol{H} = -\frac{\hbar^2}{2}\sum_i \frac{\nabla_i^{\,2}}{m_e} - \frac{\hbar^2}{2}\sum_i \frac{\nabla_i^2}{M_i} - \frac{1}{4\pi\varepsilon_o}\sum_{i,j}\frac{e^2 Z_i}{|R_i - \boldsymbol{r}_j|} + \frac{1}{8\pi\varepsilon_o}\sum_{i\neq j}\frac{e^2}{|r_i - r_j|} + \frac{1}{8\pi\varepsilon_o}\sum_{i\neq j}\frac{e^2}{|R_i - R_j|}, \quad (2.11)$$

here $M_i$ is the mass of the nucleus at point $R_i$, $m_e$ is the mass of the electron at point $r_i$. The first two terms are kinetic energy operators for electrons and nuclei, respectively.

The last three terms describe electrons-nuclei, electrons-electrons and nuclei-nuclei coulomb interactions. It is not possible to solve the Schrödinger equation containing this Hamilton operator for several hundred particles. Therefore no exact solution of the problem can be found. However we do not need an exact solution of quantum mechanical problems to perform a comparison between theoretical predictions and available experimental data because the experimental data always contain an error and an acceptable error of numerical calculation can be of the same order as the experimental error. Therefore some approximations are accepted to simplify the problem of electronic structure calculation.

As a first step, the position of the nuclei is fixed (Born-Oppenheimer approximation). This allows reduction of problem to the motion of electrons in the external field of the nuclei. This problem is still complex because the Schrödinger equation should be solved for several hundred electrons. Therefore further simplifications are necessary.

The next approximation was proposed by Hohenberg, Kohn and Sham [70]. According to this approach the ground state of an electronic system can be described by an electron density functional of E[ρ]. The exact form of the functional is unknown, but there are good approximations for the functional for different electronic systems. This approach allows the replacement of the multi-particle Schrödinger equation by a single-particle equation where an external effective field describes the interaction between electrons. According to the electron density functional theory all properties of the ground state of an electron system can be described by the electron density functional. The energy electron density functional can be written in the form:

$$E(\rho) = \int dr\rho(r)V_{ext}(r) + \frac{1}{8\pi\varepsilon_o}\iint drdr'\frac{\rho(r)\rho(r')}{|r-r'|} + G[\rho], \quad (2.12)$$

Here $V_{ext}$ is an external field which includes the electric field of the nuclei, the functional $G[\rho]$ includes the kinetic and exchange correlation energy of electrons. The ground state of an electron system can be found by minimization of the electron density functional and the total energy of the ground state is the minimum of the electron density functional. It was proposed that the $G[\rho]$ functional can be rewritten in the form:

$$G(\rho) = T[\rho] + +V_{xc}[\rho], \qquad (2.13)$$

Where $T[\rho]$ is the kinetic energy of non-interacting particles and $V_{xc}[\rho]$ is the exchange correlation part of the kinetic energy. The electron density could be presented as a sum of squared wave functions of electrons:

$$\rho(r) = e\sum_{i=1}^{N}|\varphi_i(r)|, \qquad (2.14)$$

Where N is the number of electrons. Then using equation (2.14) and taking the functional derivative in Eq. (2.11) a set of effective single-particle equations called the Kohn Sham equations [69, 71] are obtained:

$$\left[-\frac{\hbar^2}{2m_e}\nabla^2 + \frac{1}{4\pi\varepsilon_o}\int\frac{\rho(r')}{|r-r'|}dr' + V_{ext}(r) + V_{xc}(r)\right]\varphi_i = \varepsilon_i\varphi_i\,, (2.15)$$

The only unknown contributor to this problem is the exchange-correlation potential and available approximations for this functional will be treated in the next section.

Assuming the exchange correlation potential is known, The Kohn-Sham equation has to be solved self-consistently. Usually one starts with an initial guess for the density $\rho$(r), then one calculates the corresponding effective potential and solves the Kohn-Sham equations. From these one calculates a new density and starts again. This procedure is then repeated until convergence is reached.

Constructing an exchange-correlation potential is the main problem of the electron density functional theory. Several good approximations for the exchange-correlation potential were found during the last decades.

### 2.3.2 The exchange – correlation potential

As mentioned in the previous section, the Kohn-Sham equation can be solved if the exchange-correlation is known. Given the fact that an exact expression is not available, the introduction of an approximation is needed. Two such often used approximations are LDA (Local Density Approximation) and GGA (Generalized Gradient Approximation).

#### 2.3.2.1 The Local Density Approximation (LDA)

The most commonly used and successful approximation is the LDA, where the exchange correlation energy depends only on the density at the coordinate where the functional is evaluated. According to this approximation, the exchange-correlation energy can be calculated using the formula [69]:

$$E_{xc}^{LDA} = \int \rho(r)\varepsilon\big(\rho(r)\big)\, dr, \qquad (2.16)$$

where $\varepsilon(\rho)$ is the exchange and correlation energy per particle of a uniform electron gas of density $\rho(r)$. The exchange-correlation energy due to a particular density $\rho(r)$ could be found by dividing the material in infinitesimally small volumes with a constant density. Each such volume contributes to the total exchange correlation energy by an amount equal to the exchange-correlation energy of an identical volume filled with a homogeneous electron gas [69]. It is expected that this approximation should be sufficiently good in electron systems where the electron density $\rho(r)$ changes slowly. Numerous

practical calculations show that the local density approximation provides good results for different materials.

The accuracy of LDA is certainly insufficient for most applications at atomic or molecular scales as in chemistry. LDA also fails in strongly correlated systems.

### 2.3.2.2 The Generalized Gradient Approximation (GGA)

The first attempt to go beyond the LDA is the use of not only the information about the density $\rho$(r) at a particular point r but also the information about the density gradient $\nabla\rho$(r) in order to account for the non-homogeneity of the true electron density. The resulting approximation is called the generalized gradient approximation (GGA) which is given as:

$$V_{xc}[\rho] = \int \rho(r)\, v_{xc}[\rho(r), \nabla\rho(r)]dr, \qquad (2.17)$$

For systems where the charge density is slowly varying, the GGA has proved to be an improvement over LDA. For many magnetic systems, GGA predicts the correct ground state, although the magnetic moments are often overestimated.

In this thesis, the Kohn-Sham equations were solved using the Perdew-Burke-Ernerhof GGA approximation [72].

### 2.3.2 GGA+U

Although exact DFT should be capable of obtaining ground state properties correctly, the LDA and GGA are not successful for all systems. LDA and in many cases GGA fails in describing the electronic structure of strongly correlated materials which usually contain transition metal or rare-earth metal ions with partially filled d (or f) shells. Such transition metal oxides and rare- earth metal compounds normally have localized d(f) electrons and

a sizable energy gap between occupied and unoccupied subbands. When such a system is treated with LDA, which has an orbital–independent potential, a partially filled d(f) bands with a metallic type electronic structure and itinerant d(f) electrons is found. This behavior arises because in LDA the spin and orbital polarization are driven by the exchange interactions of the homogenous electron gas instead of the screened on-site Coulomb interactions [73, 74]. As a consequence, LDA fails in describing orbital polarization correctly.

We can say that LDA+U is an improvement on LDA that takes into account the on-site Coulomb interaction U, i.e. the Coulomb-energy needed to place two electrons at the same site.

The main idea behind LDA+U method is to treat the correlation of the localized d(f) electrons explicitely. This is done by adding the relevant electron-electron interaction terms to the total energy functional, meanwhilest avoiding double counting of the interaction that was already present in LDA. An expression which includes on-site Coulomb and exchange interactions was proposed by Anisimov et al. [73].

$$E^{LDA+AFM} = E^{LDA} + \frac{1}{2}\sum_{m,m',\sigma} U(n_{m\sigma} - n^0)(n_{m'-\sigma} - n^0)$$
$$+ \frac{1}{2}\sum_{m,m',m\neq m',\sigma} (U - J)(n_{m\sigma} - n^0)(n_{m'\sigma} - n^0)\,, (2.18)$$

Where $n_{m\sigma}$, with m=-2,…,+2 (d) or -3,…,+3 (f) and $\sigma$ the spin, are occupation numbers of the localized orbitals, $n^0 = \frac{1}{2(2l+1)}\sum_{m\sigma} n_{m\sigma}$ and AFM stands for *around mean field*. U and J are screened Coulomb and exchange parameters. Several improvements have been made to the previous formula. First improvement was done by Czyzyk et al. [75], they

replaced $n^0$ by $n_\sigma^0 = \frac{1}{2(2l+1)}\sum_m n_{m\sigma}$ in order to take the average of each spin separately. As a consequence of this change additional degree of freedom for spin split solutions are introduced. As a second improvement, they replaced U and J by matrices $U_{mm'}$ and $J_{mm'}$ in terms of Slater integrals and Gaunt's numbers [76].

## 2.3.3 Solution of Khon-Sham equations

After these approximations, the initial multi-particle Schrödinger equation (2.11) can be reduced to a set of simplified one-particle equations with the following form [77]:

$$\left[-\frac{\hbar^2}{2m_e}\nabla^2 + V(r)\right]\psi(r) = E\psi(r), \quad (2.19)$$

Where V(r) is the periodic potential of the crystal. To solve equation (2.19) using computational method, the one particle wave function $\psi(r)$ is represented as a linear combination of basis functions $\varphi_j(r)$:

$$\psi(r) = \sum_j C_j \varphi_{j\,(r)} \quad (2.20)$$

This wave function (2.20) is substituted into (2.19) and the obtained equation is multiplied by $\varphi_i^*(r)$, and integration in the real space is performed [77]:

$$\sum_{j=1}^{N} C_j \left(H_{ij} - EO_{ij}\right) = 0, \; j = 1,..N \quad (2.21)$$

where $N$ is the number of basis wave functions, $H_{ij}$ and $O_{ij}$ are matrix elements:

$$H_{ij} = \int \varphi_i^*(r)\, H\varphi_j(r)dr \quad (2.22)$$

$$O_{ij} = \int \varphi_i^*(r)\, \varphi_j(r)dr$$

Where H is the Hamiltonian in equation (2.18).The eigenvalues of energy E(k) are the roots of the secular equation:

$$det\|H_{ij} - EO_{ij}\| = 0, \quad (2.23)$$

Different computation methods differ by the choice of the basis wave functions. The choice of a good basis set will be very important because the accuracy of the approximation as well as the needed computation time will strongly depend on it. The calculated $\psi(r)$ will approach the real solutions better if a larger basis set is used, but this will increase the computation time because of the increased matrix size. Using a smaller basis set means a smaller matrix and consequently less computation time. However, this kind of basis set is not generally applicable because every system needs its own optimized basis set. Such basis set is efficient for a specific system, but the resulting wave functions adopt many properties from the basis, therefore it is called biased. In practice, good basis sets are simultaneously efficient and unbiased. One important example will be described in the following section.

### 2.3.3.1 Augmented Plane Wave method (APW)

The idea of APW basis set is to divide the crystal space into two parts. First a sphere of radius $R_\alpha$ around each atom. Such a sphere is often called a Muffin Tin (MT) sphere, the part of space occupied by the spheres is the MT region. The remaining space outside the spheres is called the interstitial region (denoted by I). The electron wave function is expanded in different basis in these two parts. The electron wave function changes rapidly near atomic nuclei, therefore it is quite natural to use a solution of the Schrödinger equation for atom to represent the wave function in the MT-spheres. In the interstitial part of the crystal electrons are quasi-free, and the electronic wave function

can be well represented by a set of plane waves. Thus the basis functions have the following form [69]:

$$\varphi_K^k(r,E) = \begin{cases} \frac{1}{\sqrt{V}} exp[i(k+K)r], & r \in I, \\ \sum_{l,m} A_{l,m}^{\alpha,k+K} u_l^\alpha(r',E) Y_{l,m}(r'), & r \epsilon R_\alpha, \end{cases} \quad (2.24)$$

Where V is the crystal volume, K is the translation vector in the reciprocal space, $Y_{l,m}$ are spherical harmonics, $u_l^\alpha$ is radial solution of the Schrödinger for an atom at $r_\alpha$

$$r' = r - r_{\alpha,} \quad 2.25$$

The A coefficients in (2.24) can be determined if we impose the condition of continuity of the basis functions on the MT-spheres.

Unfortunately, the APW method has an important drawback: the energy dependence of $u_l^\alpha(r',E)$. In order to describe an eigenfunction $\psi(r)$ properly, the corresponding eigenvalue $\varepsilon_r$ must be used for E. Since $\varepsilon_r$ is not known yet a guess must be made for the value of E. For this value of the eigenvalue, the APW basis can be constructed and the Kohn-Sham equation can be solved. The guessed E should be a root of this equation. If not, a new value of E must be tried until the chosen value turns out to be an eigenvalue of the equation. This procedure has to be repeated for every eigenvalue and is therefore very time consuming.

### 2.3.3.2 Linear Augmented Plane Wave Method (LAPW)

The energy dependence of the determinant in APW method can be eliminated if we expand the radial part of the basis functions in Taylor series near a fixed energy $E_o$ [69]:

$$u_l^\alpha(r',E_o) = u_l^\alpha(r',E_o) + (E_o - \varepsilon_k^n)\dot{u}_l^\alpha(r',E_o) + O(E_o - \varepsilon_k^n)^2, \quad (2.26)$$

Where $\varepsilon_k^n$ are the eigenvalues that we want to find, and the derivative of $\dot{u}_l^\alpha$ function is calculated at the fixed energy $E_o$. The difference $E_o - \varepsilon_k^n$ is not known, so we can replace it by coefficient B:

$$\varphi_K^k(r,E) = \begin{cases} \frac{1}{\sqrt{V}} exp[i(k+K)r], & r \in I \\ \sum_{l,m} [A_{l,m}^{\alpha,k+K}\, u_l^\alpha(r',E_o) + B_{l,m}^{\alpha,k+K}\, \dot{u}_l^\alpha(r',E_o)] Y_{l,m}(r'), & r \epsilon R_\alpha \end{cases}, \quad (2.27)$$

The two coefficients A and B can be found if we impose the condition of continuity for the u function and its derivative at the MT-spheres.

Because different atomic orbitals have different energies, it would be reasonable to take different linearization energies for different orbital. Therefore the basis functions of the LAPW method is represented in the following form [69]:

$$\varphi_K^k(r,E) = \begin{cases} \frac{1}{\sqrt{V}} exp[i(k+K)r], & r \in I \\ \sum_{l,m} [A_{l,m}^{\alpha,k+K}\, u_l^\alpha(r',E_l^\alpha) + B_{l,m}^{\alpha,k+K}\, \dot{u}_l^\alpha(r',E_l^\alpha)] Y_{l,m}(r'), & r \epsilon R_\alpha \end{cases} \quad (2.28)$$

The LAPW method was realized in the WIEN2k code [68]. In addition the crystal potential is represented according to formula:

$$V(r) = \begin{cases} \sum_{L,M} V_{L,M}(r) Y_{LM}(r) & r < R_{MT} \\ \sum_K V_K e^{iKr}, & r > R_{MT} \end{cases} \quad (2.29)$$

Therefore there is no imposed restriction to the shape of the potential and this method is referred to as the full-potential approach.

### 2.3.3 The WIEN2k Code

To perform an actual calculation a software package is needed in which this theory is implemented. All calculations performed in this work are executed using the WIEN2k code. The input routine starts from a structure file containing information on the atomic configuration of the system such as lattice parameters, atomic species, atomic positions, muffin-tin radii, etc. Based on this file the subroutines NN, SGROUP and SYMMETRY check for overlap between the different muffin-tin spheres and determine the symmetry of the unit cell. In the next step LSTART calculates the atomic densities for all atoms in the unit cell which KGEN uses in combination with the other input files to determine a suitable k-mesh. And in the final initialization step, DSTART, the starting electron density $\rho$ is constructed based on a superposition of the atomic densities. During this initialization all the necessary parameters are fixed as well: the exchange-correlation approximation (LDA, GGA), $R_{MT}K_{max}$, $l_{max}$ and the energy parameter that separates the core states from the valence states.

Once the starting density is generated the self-consistent calculation can start. This process is divided into several subroutines which are repeated over and over until convergence is reached and the calculation is self-consistent. LAPW0 starts with calculating the Coulomb and the exchange-correlation potential. Next LAPW1 solves the secular equation for all the k-values in the k-mesh and finds by diagonalization of the Kohn-Sham equation the eigenvalues and eigenfunctions of the valence states. The following subroutine, LAPW2, determines the Fermi-energy which separates filled from unfilled states. Once this energy is known the eigen functions resulting from LAPW1 can be used to construct a valence density$(\rho_{val})$.

The states and energies of the core electrons are calculated separately in the LCORE subroutines which results in a total core density ($\rho_{core}$).The densities $\rho_{val}$ and $\rho_{core}$ are combined to give the total density $\rho_{tot}$. Since the total new density is often different from the old density $\rho_{old}$, they are mixed by MIXER to avoid large fluctuations between iterations that would lead to divergence. Once the end of the cycle is reached, WIEN2k checks for convergence between the old and the new densities. If they are different up to a specific factor, a new iteration will started with the new density as input density. This procedure is repeated until the old and the new densities are consistent. In this case, the self-consistency cycle ends and the self-consistent solution of the equation equals $\rho_{new}$ (also $E_{tot}$ is calculated and compared).

In this work, we used the FP-LAPW method as implemented in WIEN2k package [68] to study the magnetic properties of Mn-doped 6H-SiC. The embedded impurities in SiC are modelled by a 2×2×1 supercell (Figure.2.20). The muffin-tin radii (RMT) have been chosen as 1.66 au for Si and C and 1.77 au for Mn. An optimum number of k-points were reached by testing the convergence of the total energy and the electric field gradient for the basic unit cell of 6H-SiC with two Mn as substitutional atoms. The supercell calculations were performed with an energy cut-off such that $R_{MT}K_{max}$ = 6.0 and a k sampling with a 8×8×2 Monkhost-Pack mesh. The Kohn-Sham equations were solved using the Perdew-Burke-Ernerhof GGA

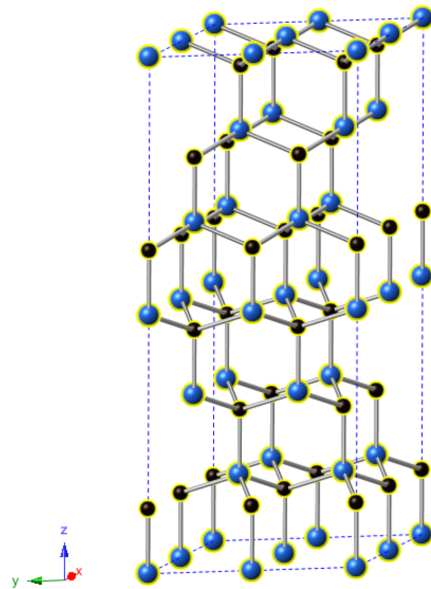


*Figure 2.20. The supercell used in the calculation*

approximation. The self-consistent cycles were stopped when the total energy difference between successive cycles is less than 0.0001 Ry and the charge density difference between successive cycle is $10^{-4}$.

# Chapter 3. Results and Discussions

In this chapter, we present the results obtained during this PhD research. Four major parts have been explored, all related to ion implantation in 6H-SiC. First, we present the characterization study of the Mn implantation induced structural damage in the 6H-SiC lattice. The second part deals with the magnetic characterization of the implanted samples while the third is devoted to the effect of the thermal annealing on the structural and magnetic properties of the implanted samples. In the final part, *ab-initio* calculation results are used for an attempt in understanding the magnetic properties of the implanted samples.

A detailed explanation and a more elaborate discussion of the presented results in this chapter can be found in the articles that have been published in, or submitted to international peer-reviewed journals. These articles have been added at the end of this thesis.

## 3.1 Ion implantation-induced lattice damage

The Mn implantation-induced damage in 6H-SiC has been structurally characterized using X-ray diffraction to determine the macroscopic strain, while the RBS/C technique has been used to determine the profile of displaced Mn atoms, as previously explained in chapter 2. In particular, the investigation of defects accumulation by increasing the implantation fluence is emphasized. In order to evaluate the level of structural damage produced on a sample by ion implantation, one has to define a standard of quality for the crystalline structure. Such a standard can be obtained by comparing the random RBS/R and channeled RBS/C spectra for the as-grown and unprocessed sample. Figure 3.1 shows RBS/R and RBS/C measurements obtained from the virgin 6H-SiC sample.

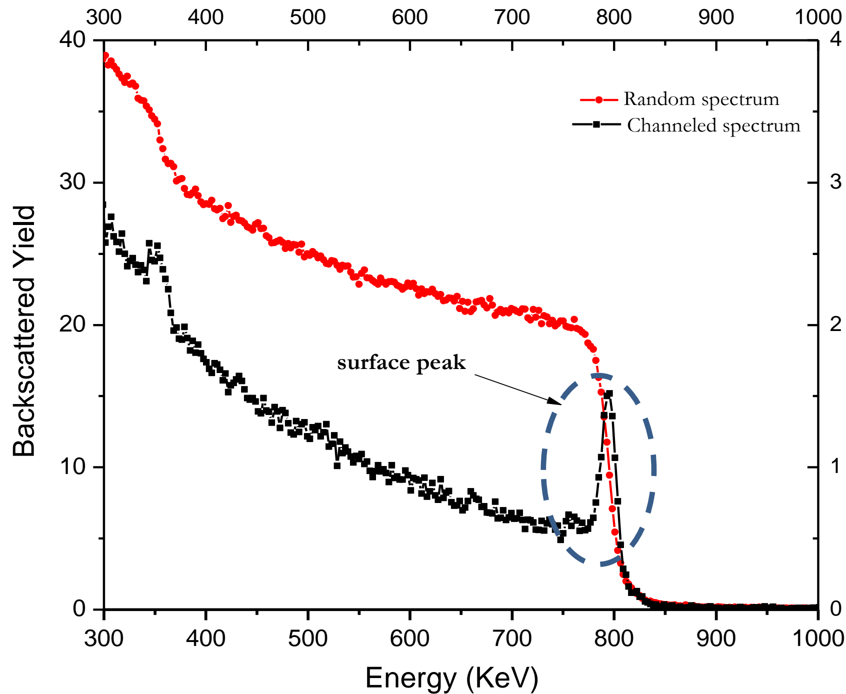


*Figure. 3.1. Random and channeled RBS spectra obtained from virgin 6H-SiC sample.*

In fact, if the incident ion is well aligned with a channel from a perfect lattice, the probability of a close encounter event, resulting on the backscattering of that ion is very

small. However if the lattice is damaged, the channeled particles interact strongly with host atoms on non-regular lattice positions that obstruct the channel. As a consequence, the yield of backscattered particles increases. As observed from Figure 3.1, the remarkable difference between the backscattered yields from the two alignment directions is an indication of the sample excellent crystalline quality. The structural defects generated in the crystal structure upon ion-implantation drastically alter the shape of the channeled RBS spectrum. This can be seen in figures 3.2 where the yields from virgin and implanted sample are shown.

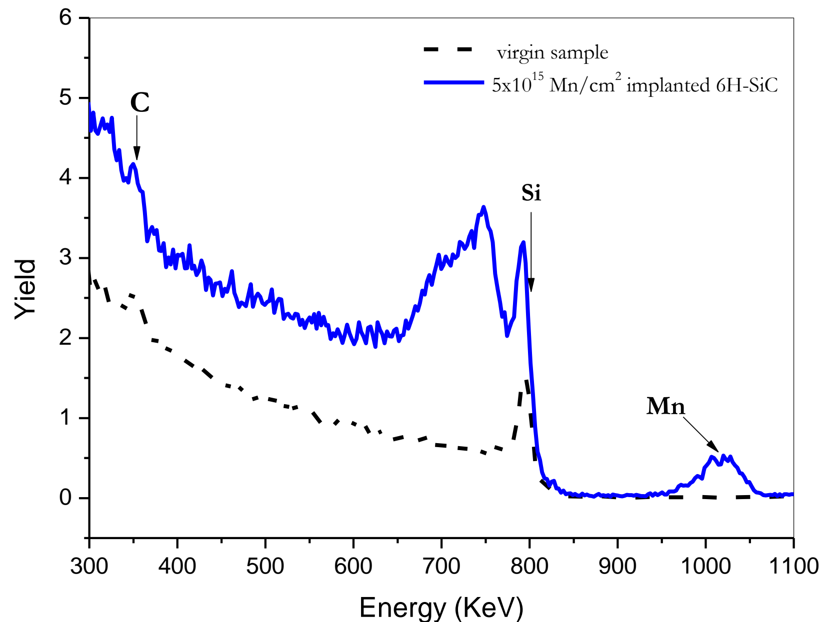


*Figure. 3.2. Channeled RBS spectra obtained from virgin 6H-SiC sample and 5×10^15 Mn/cm^2 implanted 6H-SiC.*

The increased backscattering yield at the region close to the surface is an indication of the amount of Mn atoms displaced during implantation. A second peak, which appears close to the surface, can be observed in the spectra. It reflects the presence of a thin, highly disordered layer at the surface of the 6H-SiC film. Furthermore, in the same spectrum, the yield below 700 keV (undamaged crystal) is considerably higher than the equivalent region of the unimplanted sample spectrum. This yield increase at the undamaged lattice

is a consequence of the $^4He^+$ ions dechanneling at the surface damaged region on the implanted sample. The incoming He-ions are first dechanneled by the displaced host atoms and are then backscattered during other collision events with host atoms from the undamaged region. The dechanneled fraction of ions has to be taken into account for the quantitative evaluation of the lattice disorder. Usually, a linear increase of the dechanneling fraction is assumed [78], but a more correct treatment of this analysis was proposed by Schmid in 1973, as described in reference [79]. Schmid developed an iterative procedure to calculate the dechanneled fraction, assuming a linear relation between the dechanneled fraction and the defect fraction in a certain depth window ($f_{dec}/f_{def} = C$), and using the straight line approximation as a first input. The iterative procedure optimizes the proportionality factor C and gives rise to a more accurate dechanneled fraction. For a more detailed explanation of this procedure, we refer to the literature [79].

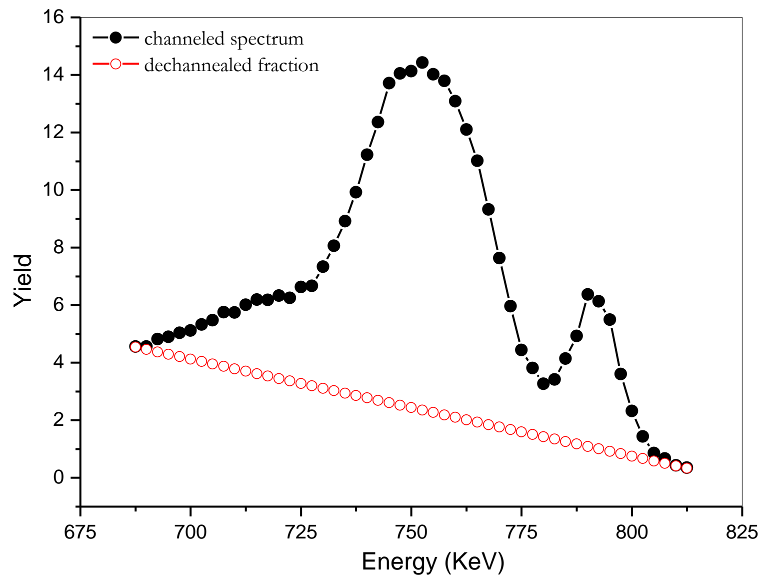


*Figure. 3.3. Channeled RBS spectra of 80 keV Mn-implanted 6H-SiC, the red open circles represent the total dechanneled fraction.*

In this work, we assume a linear increase of the dechannelimg fraction and we subtract this fraction from the RBS spectrum as shown in Figure 3.3. The dopant fluence has a

strong weight in the generation of structural damage on the host lattice. It is thus important to assess how this damage builds up with increasing dopant fluence. For this purpose, a set of 6H-SiC samples was implanted with Mn atoms using four different fluencies of $1\times10^{12}$ (sample A) , $5\times10^{15}$ (sample B), $1\times10^{16}$ (sample C) and $5\times10^{16}$ (sample D) Mn/cm$^2$. The implantation was carried out using Mn ions of energy 80 keV at 365°C (to allow for crystallization).

### 3.1.1 Structural characterization

#### 3.1.1.1 Defects and Mn profiles

After the implantation, each sample has been characterized by RBS/C. Figure 3.4 presents the RBS/C spectra from the set of the implanted samples as compared to the randomly aligned backscattering yield. As can be seen in this figure, the spectrum height increases monotonically with fluence. This reveals that damage accumulation occurs during irradiation. The spectra recorded in the axial direction on crystals implanted with Mn ions exhibit a strong increase of both the Si yield (around 750 keV) and the C yield (around 350 keV), due to the creation of radiation damage in the near-surface region of the target. The presence of Mn atoms implanted into SiC is shown by the peak appearing around 1000 keV. It is clear from Figure 3.4 that the C yield is much lower than the Si yield for all fluences. This behavior can be described by the differential cross section (appendix B). Since the differential cross section scales with $Z^2$, standard RBS is more sensitive for the detection of elements with high Z.

Since the kinematic factor $K_1$ (The energy ratio ($E_1/E_0$) between the scattered particle and the incident particle) is larger for Si than for C, the $He^+$ backscattering yield of C can be detected at lower energies.

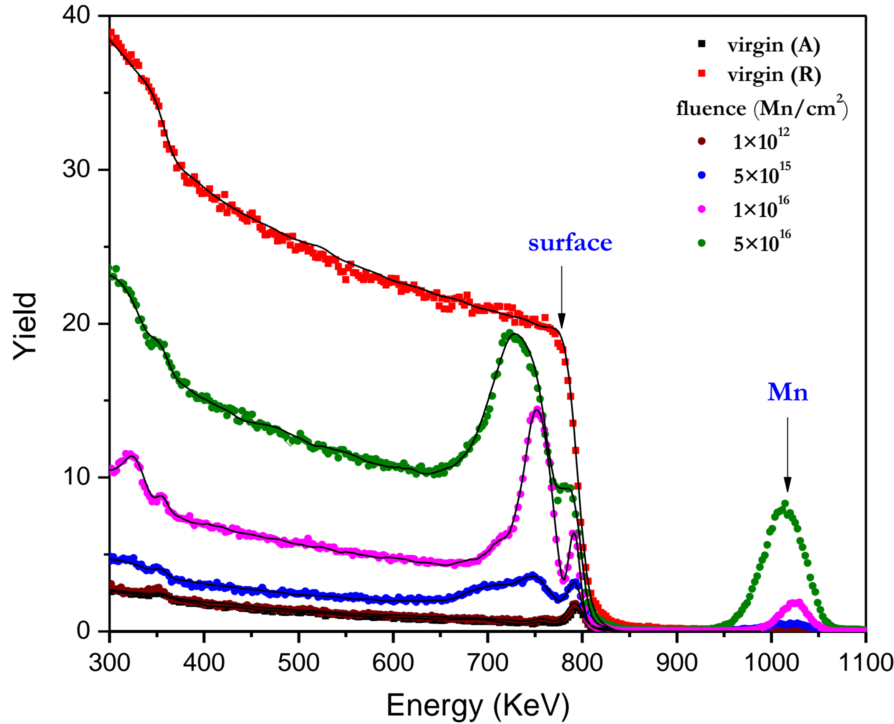


*Figure. 3.4. The RBS/channeling spectra (A) and corresponding McChasy fits (solid lines) for samples A, B, C and D. The random RBS spectrum (R) for the virgin is also included for comparison.*

Consequently, the carbon yield overlaps with a broad silicon background originated from the bulk material. These conditions make the detection of backscattering yield from the carbon sublattice of SiC quite difficult. So, the analysis of the Si RBS spectrum (Yield-Energy) provides us with information about the type of defects introduced due to Mn implantation. The change in the yield (quantity and shape) is a good indication about the accumulation of the defects and the type of the defects. Figure 3.5 shows the individual spectrum for each fluence after the subtraction of dechanneled fraction. The channeled spectrum can be fitted using Gaussian function. The best fit is obtained using three peaks that may be attributed to different type of defects.

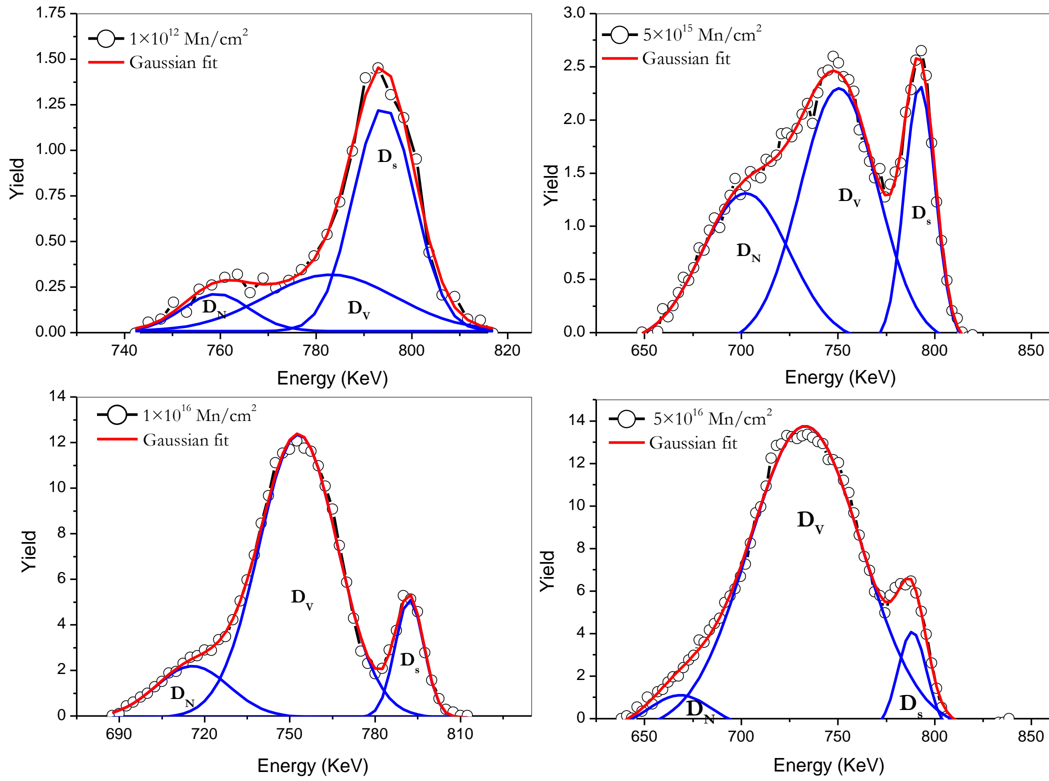


*Figure.3.5. The RBS/C spectra for samples a, B, C and D. The solid lines are the Gaussian fitting of each spectrum.*

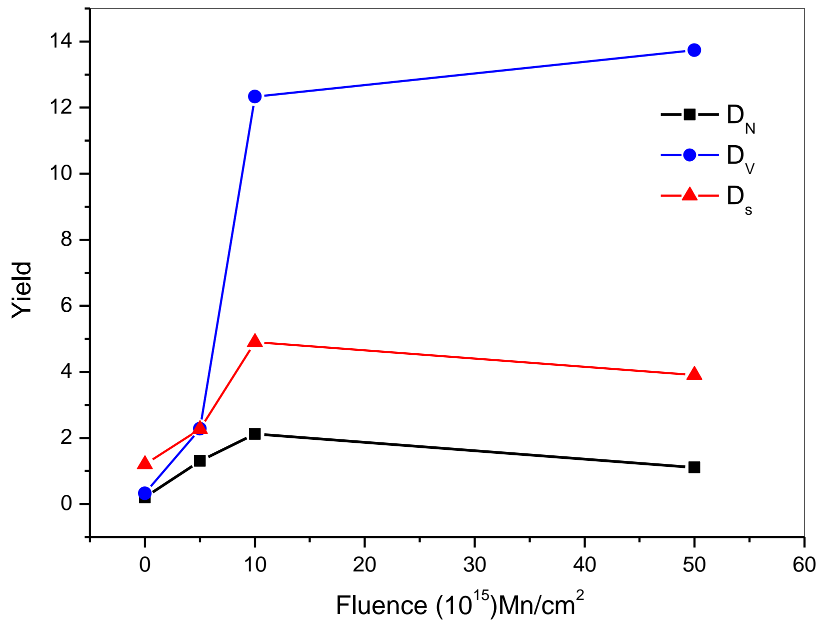


*Figure. 3.6. Maximum yield of different types of defects versus fluence as deduced from Figure. 3.5.*

Since Mn has a large atomic radius, its implantation into SiC is expected to result in a high density of Si and C vacancies ($Si_V$,$C_V$) and interstitials ($Si_I$, $C_I$). While the vacancies are likely to stay closer to the surface, the interstitials are supposed to be in excess at the end range of the implanted ions [80]. It is also expected that the distribution profile for the ($C_I$) will be displaced to a greater depth with respect to that of the Si interstitials ($Si_I$), considering respective atomic mass of C and Si. So, we can assume that the three peaks observed in Figure 3.5 are stemming from the different parts of the vacancies and interstitial dominated zone; (i) the higher energy related peak 1 ($D_s$) is originating from the surface region, (ii) an intermediate peak 2 ($D_V$) is originating from the region which is dominated by both $Si_V$ and $C_V$ with a small concentration of interstitial atoms ($Mn_I$, $Si_I$, $C_I$), (iii) while the origin of lower energy related peak 3 ($D_N$) is the tail section of the $C_I$ distribution profile, as illustrated in Figure 3.7.

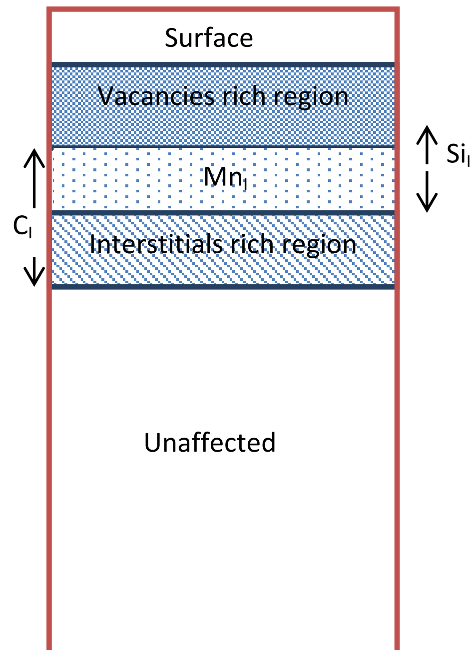


*Figure. 3.7. Schematic representation of the distribution of the vacancies and interstitials in the implanted layer.*

From figure 3.6, we can see that the surface damage increases as the fluence increases; the increase in the surface defect is accompanied with increasing of vacancy related defects ($D_v$). The surface defects saturate at fluence of 1x10$^{16}$ Mn/cm$^2$ whereas $D_v$ continue increasing but at smaller rate. For low implantation fluences (< 5x10$^{15}$ Mn/cm$^2$) the damage concentration is still very limited and located in the vicinity of the surface. At these low fluences the density of collision cascades is still negligible. The damage is mainly composed of point defects such as Si and C interstitials and vacancies, and small clusters that failed to recombine while the energy within the cascades was being dissipated. These point defects are mobile at room temperature and higher temperature of substrate enhances this diffusion process. They are thought to migrate and accumulate at the host surface which acts as effective sink. Increasing the fluence leads to a more frequent overlapping of collision cascades from ion entering the target along trajectories that are close to each other. As a result, the concentration and the size of defects increases giving rise to the $D_V$ peak for fluences above 1×10$^{12}$ Mn/cm$^2$. The vacancy related peak ($D_v$) centered about the same position regardless of the dose, while its concentration increases with increasing fluence. This is expected because as the implanted ion fluence increases, more vacancies are created. The fraction of accumulated disorder ($f_D$) as a function of depth in the crystals was extracted from simulations of RBS/C spectra with the McChasy Monte-Carlo package and summarized in Figure 3.8a. The parameter $f_D$ is evaluated by taking the ratio of Si yield in axial (A) and random (R) directions, respectively.

$$f_D = \frac{Si\ yield_A}{Si\ yield_R} \qquad (3.1)$$

It is worth to notice that the parameter $f_D$ actually takes value of 0 and 1 for single crystal and amorphous system, respectively, and therefore defines the degree of structural order/disorder of the system.

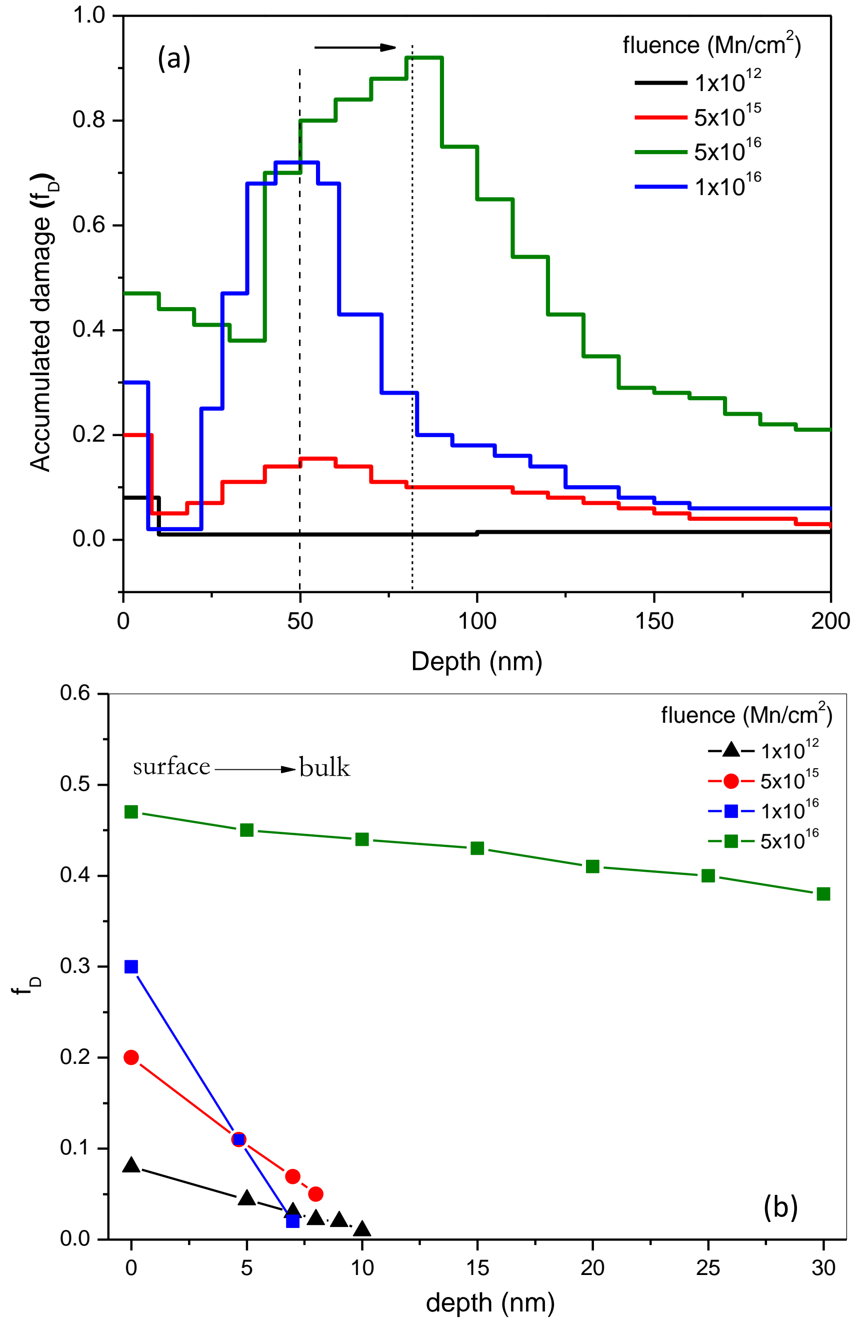


*Figure. 3.8 (a) Defects profile deduced from RBS spectra using McChasy fitting, (b) Accumulated damage at the surface region.*

We see from Figure 3.8a that the accumulated damage increases with increasing fluence ( 0.16 for $5\times10^{15}$, 0.7 for $1\times10^{16}$ and 0.9 for $5\times10^{16}$ Mn/cm$^2$). The accumulated damage is very small for the lowest fluence ($1\times10^{12}$ Mn/cm$^2$) which is mainly attributed to surface defects (see Figure 3.6), but substantially increases as the fluence increases from $5\times10^{15}$ Mn/cm$^2$ due to the increase in the vacancies and interstitials concentrations. Indeed, the sample is almost amorphous for the highest fluence. The accumulated damage is high at the surface for all fluences and decreases to 0 at ∼10 nm depth (Figure.3.8b). This may be described by the formation of a thin amorphous layer at the surface resulting from migrating point defects, which become trapped at the SiC surface. For the fluence of $5\times10^{16}$ Mn/cm$^2$, the surface defects saturate at about 0.4%. This can be due to the extension of the amorphous layer from the surface toward the bulk which then overlaps with vacancies and interstitial rich regions.

The accumulated damage as a function of depth was fitted using Gaussian functions to determine the accumulated damage of different type of defects. From the fitting (Figure 3.9), two broad peaks can be distinguished centered around 42 nm ($D_v$) and 90 nm ($D_N$), respectively. The first peak ($D_v$) coincides with the end of range of the implanted Mn ions, $R_p$= 47 nm, as extracted from Mn concentration versus depth graph (Figure 3.10) and also from the one calculated with SRIM (Figure 3.11).

In this region, the Mn ions lose most of their energy in nuclear collision, causing many displacements in the lattice. The damage build–up is dominated by simple point defects such as Mn, Si and C interstitials and vacancies (Si and C vacancies as calculated from SRIM).

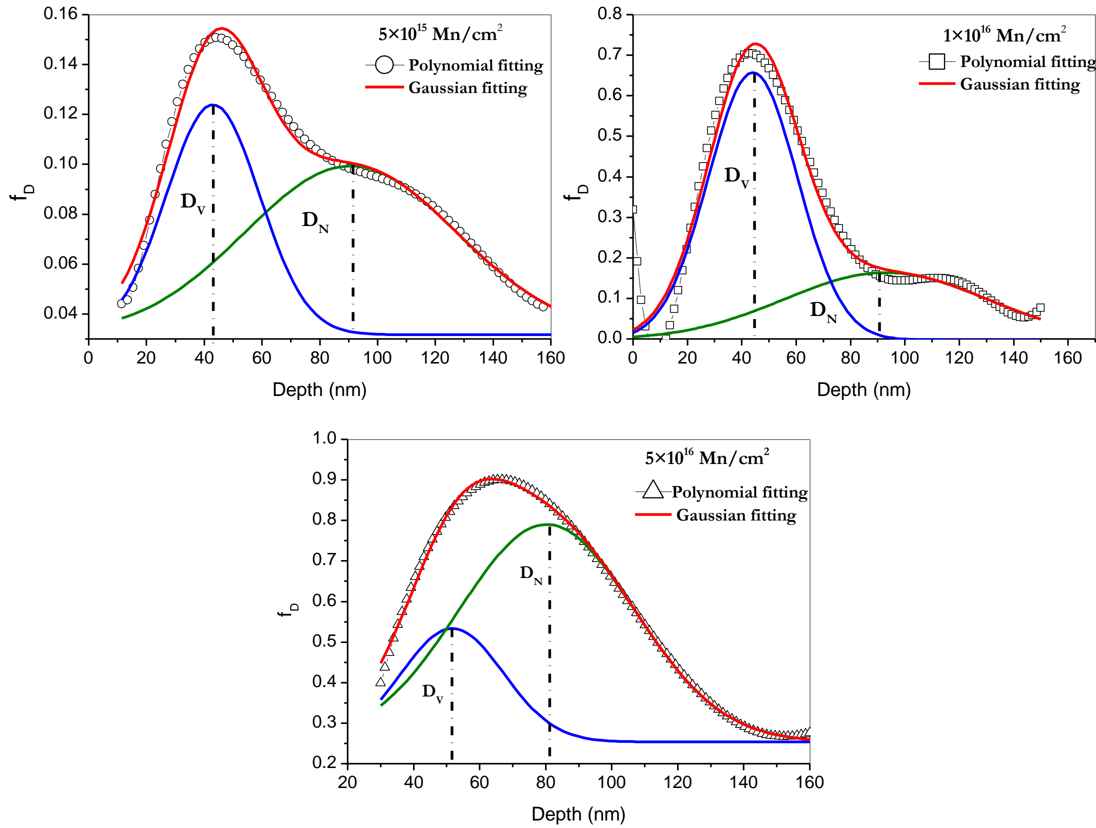


*Figure. 3.9. Polynomial and Gaussian fit of accumulated damage versus depth.*

As it is clear from Figure (3.11), the amount of lattice disorder predicted by SRIM Monte Carlo calculations is much higher compared to the experimentally determined disorder, indicating that these defects are mobile and their mobility is enhanced by the substrate temperature (365$^{o}$C) during implantation process. For the highest fluence (5×10$^{16}$ Mn/cm$^{2}$) the $D_N$ peak is the most dominant due to the cascades of the simple defects.

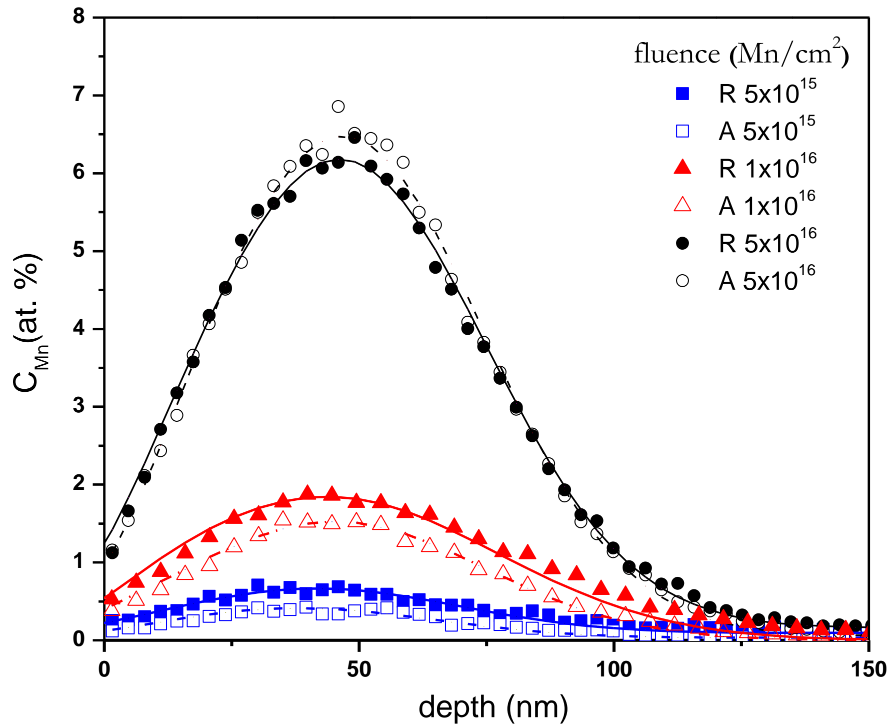


*Figure. 3.10. Mn distribution vs depth for samples B, C and D random (R) and axial (A) directions respectively*

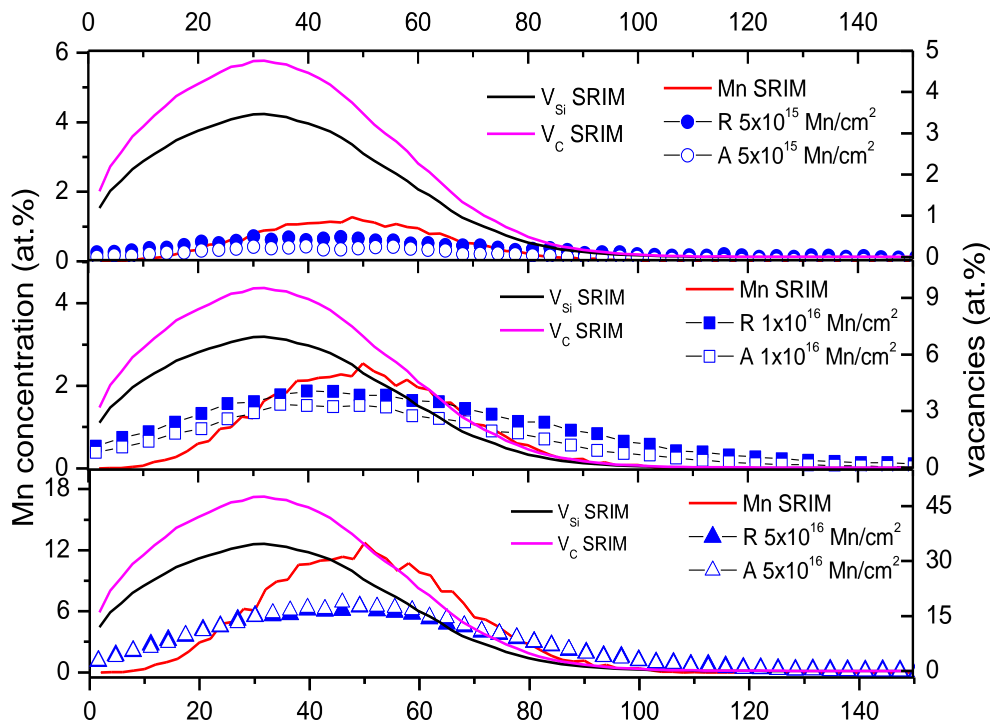


*Figure. 3.11.Mn and vacancy distribution calculated by SRIM for samples B, C and D.*

The concentrations of Mn as deduced from figure 3.10 are 0.7 at%, 1.7 at% and 7 at% for $5\times10^{15}$, $1\times10^{16}$ and $5\times10^{16}$ Mn/cm$^2$, respectively.

As discussed earlier in section 2.1, implanted ions can occupy several positions in the SiC lattice. One of the crucial and open questions about the magnetism observed in this type of DMS is to know the position of Mn and the corresponding percentage in substitutional and interstitial sites. The fraction $f_s$ of Mn atoms that occupy substitutional sites (Si and/or C) is calculated using equation:

$$f_{s}= \frac{1-\left(\frac{Y_A}{Y_R}\right)_{Mn}}{1-\left(\frac{Y_A}{Y_R}\right)_{Si}} \qquad (3.2)$$

Where $Y_A$ and $Y_R$ stand for the yields in aligned and random configurations respectively. More details about the determination of lattice site positions by RBS/C can be found in references [78-79][78, 79]. The results are summarized in table 3.1 below.

***Table 3.1.*** *Ratio of Mn atoms that occupy substitutional (Si and/or C) sites for samples B,C and D.*

| Fluence Mn/cm$^2$ | $(Y_A/Y_R)$ Si | $f_D$ | $(Y_A/Y_R)$ Mn | $f_s$ |
|---|---|---|---|---|
| $5\times10^{15}$ | 0.19 | 0.16 | 0.65 | 0.41 |
| $1\times10^{16}$ | 0.71 | 0.72 | 0.80 | 0.63 |
| $5\times10^{16}$ | 1.00 | 0.92 | 1.00 | 0 |

It is clearly seen from table 3.1 that the accumulated damage increases with increasing fluence and the ratio of Mn atoms that occupy the substitutional sites increases to a specific amount and then starts to decrease again for fluencies greater than $1\times10^{16}$

Mn/cm$^2$ indicating that more Mn atoms occupy interstitial positions. Indeed, for the sample 5×10$^{15}$ Mn/cm$^2$, about 41 % of Mn occupy substitutional (Si and/or C) sites, which is in agreement with the result obtained in Fe implanted 6H-SiC with a fluence of 2.2×10$^{16}$ Mn/cm$^2$ [21]. Unexpectedly, the amount of Mn at substitutional sites increases with increasing the fluence to 1×10$^{16}$ cm$^{-2}$. Since the amount of Mn at Si sites (column 4 of table 3.1) decreases with increasing the fluence, we argue that more Mn atoms occupy C sites with increasing fluence. This explanation is plausible based on the fact that C atoms relatively penetrate deeper in SiC matrix as compared to Si atoms due to Mn scattering. The C atoms are indeed lighter and therefore more C vacancies ($C_v$) at Mn maximum concentration are expected to be available. The vacancies are in general very unstable and the mechanism of possible Mn-$C_v$ recombination is unclear at this stage. The annealing performed on these samples can provide some highlight on the diffusion of Mn and vacancies, as discussed later in this chapter. The drastic decrease of the fraction of Mn atoms occupying a regular substitutional site for the fluence to 5×10$^{16}$ cm$^{-2}$ is attributed to the degradation of the crystal lattice caused by a substantial enhancement of defects concentration.

From this study, we conclude that the maximum amount of Mn at substitutional sites is also accompanied with increasing implantation-induced defects concentration. A fundamental question that may arise from this aspect is what role these defects play on magnetism. Besides, the annealing effect investigated below, *ab-initio* calculation has been performed to tackle a number of configurations considering Mn at different sites with various types of vacancies.

### 3.1.1.2 Implantation induced Strain

As mentioned in the previous chapter, high resolution X-ray diffraction (HRXRD) was also performed in order to complement the structural characterization obtained by RBS/C. Figure 3.12 shows the (0006) reflection peaks of implanted 6H-SiC samples. It is clear from this figure that the HR-XRD spectrum of the implanted sample with the lowest fluence of $1\times10^{12}$ $cm^{-2}$ and virgin 6H-SiC sample results in a single sharp diffraction peak at 2θ-value of $35.6^{o}$, which corresponds to the (thick) unperturbed part of the sample. This was expected since the depth probed by X-rays in this configuration reaches ~4 μm as compared to the ~0.1μm damaged thickness. The interference fringes indicate that the Mn-implanted 6H-SiC is still partly crystalline, their absence for the highest fluences reveals a loss in the crystallinity of the implanted region of the samples.

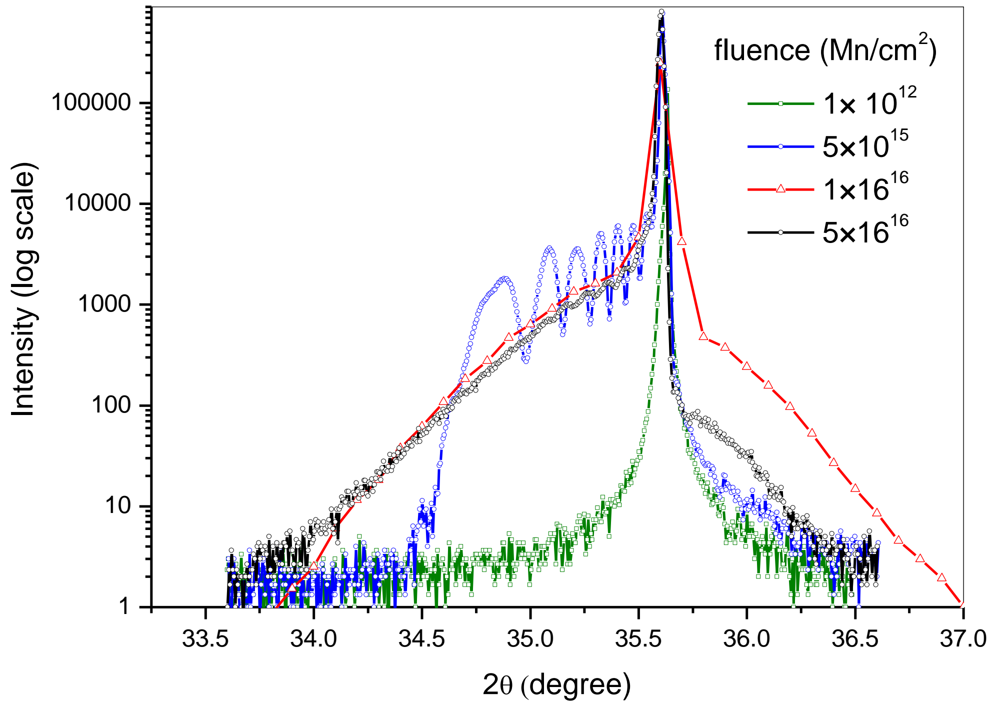


*Figure.3.12. X-ray diffraction patterns of the four Mn-implanted 6H-SiC samples.*

As the fluence increases, a shoulder at the vicinity of the main 6H-SiC (0006) reflection peak with a long tail falling to the lower angle side appears on the spectra measured on the implanted samples. The significance of this shoulder can be understood taking into account the Bragg's law (2.4), from which it is possible to conclude that a smaller $\theta$ angle corresponds to diffractions from planes with larger inter-planar distances. The larger inter-planar distance reveals lattice expansion caused by the implantation process. The cause of this expansion as mentioned in section 2.2.2.1 may be the heavy Mn ions that principally occupy substitutional Si or C sites after implantation or it can be due to the interstitial atoms (Si, C or Mn) in the SiC lattice. It is then expected that the lattice strain profile follows the same distributional behavior as the implantation induced defects. Considering the Gaussian distribution defect profile, as obtained from SRIM and RBS/C measurements, one can expect the lattice parameter to have its maximal value, corresponding to the maximum strain, centered at the peak of the concentration of defects. Previous studies have shown that the strain induced by implanted ions is strongly localized along the direction perpendicular to the implanted surface [81, 82].

The presence of interference fringes is due to the coherent diffraction between two zones of same strain on either side of a region with a different strain [82]. The strain depth profiles for the samples B, C and D are deduced from HRXRD patterns (Figure 3.13) using equation (2.7) and assuming the maximum strain occurs at the maximum defect profile.

As it is clear from figure (3.13), the strain increases with increasing fluence, from 2% for $5\times10^{15}$ to 4% for $1\times10^{16}$, reaching a value of 5% for $5\times10^{16}$ $Mn/cm^2$. Previous work performed by Bai et al [83] observed similar effect in the XRD spectra of self-implanted Si.

They came to the conclusion that the strain distribution is dominated by interstitial-like defects [84].

Combining results obtained from RBS/C and HR-XRD measurements, we conclude that implantation damage is distributed throughout two major defect regions, one at the surface and another close to the ion end of range.

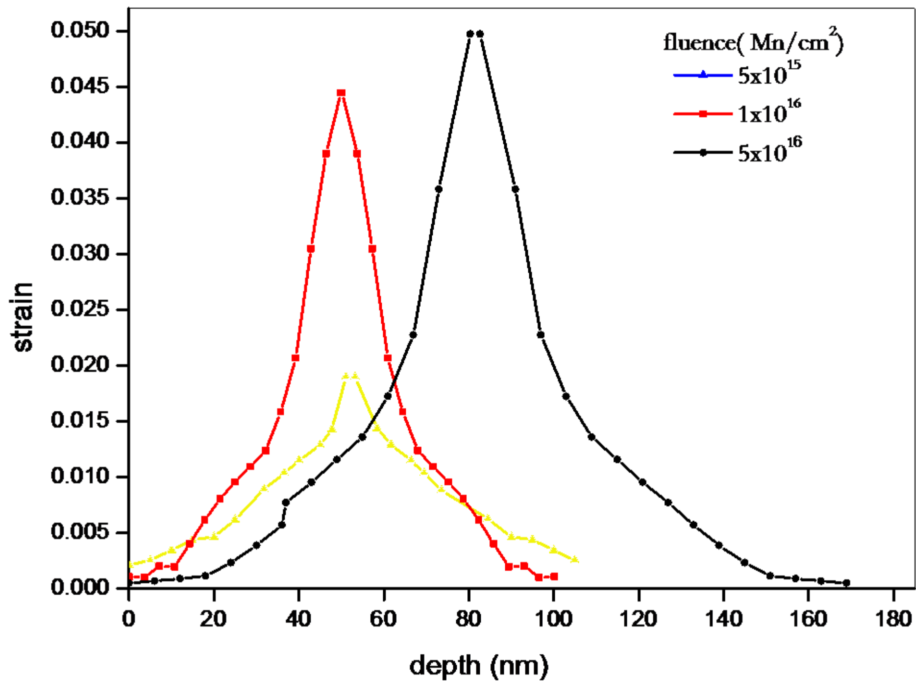


*Figure.3.13 Strain depth profiles for samples B, C and D deduced from HRXRD patterns by using equation (2.7).*

This damage generates strain along the direction perpendicular to the surface. At room temperature the defects are mobile and tend to recombine or migrate towards the crystal surface. Remaining defects in the end of range region generate lattice expansion. By increasing the fluence, more complex defects are formed due to the increase in the density of the collision cascades. Theses defects further expand the lattice in the region of implantation. The defects keep migrating and accumulating at the surface, forming a completely disordered region. Further increase in the ion fluence leads to further lattice

expansion accompanied by deterioration of the crystalline structure. At the same time, the concentration of point defects at the surface keeps increasing and consequently the thickness of the amorphous region increases inwards. It is important to notice that the strain at the maximum concentration Mn profile (about 50 nm) is higher for the lowest and essentially for the intermediate fluence. This is understood by the observation that for the highest dose, the crystal structure for the Mn-rich region is strongly damaged and the strain is rather localized since only short-distance order is preserved from one hand, and the XRD analysis provides the macroscopic strain only. The defects-rich region for $5\times10^{16}$ Mn/cm$^2$ fluence retains relatively its crystalline integrity due increasing lattice parameter perpendicular to the plane of the film.

From this study, we deduce that the defects and Mn profile are related (since their depth profiles are both centered at the same position of around 50 nm) for the two lowest doses. For the highest dose, another type of Mn related defects is expected (since the defects profile is centered at around 80 nm and Mn profile at 50 nm). In this respect, defects complexes may have different electrical features and the supposed carriers-mediated magnetism may strongly be affected.

The electrical properties were addressed using micro-Raman spectroscopy technique. The results are presented in the next section.

### 3.1.1.3 Micro-Raman spectroscopy (μRS) measurements

The Raman parameters such as intensity, width and peak frequency shift provide valuable information on the crystal quality. In fact, Raman analysis of the stacking structure of polytypes, stacking disorder, strain and damage in ion implanted SiC were widely investigated [85-88].

In particular, Raman measurements enable detection of coupled modes of LO phonon and plasmons. Indeed, collective oscillations of free carriers are accompanied by a longitudinal electric field. This collective motion couples with LO phonons oscillations in polar semiconductors via the macroscopic polarization field, and forms LO phonon-plasmon coupled (LOPC) modes. This LOPC mode depends strongly on the carrier's concentration and carriers damping.

The effect of Mn doping on the Raman shift is attributed mainly to the difference in atomic sizes; the radius of Mn ion is larger than the radius of Si and C atoms. In Mn implanted SiC, Mn will occupy Si or C lattice positions, or alternatively Mn can go to interstitial sites. The size difference is expected to result in an increase of the lattice parameter. The interatomic distance of Si-C bond will increase which results in an increase of the phonon oscillation frequencies. This happens because Raman scattered light occurs at wavelengths that are shifted from the incident light by the energies of molecular vibrations. These molecular vibrations are due to the displacement of one or more atoms connected to each other from their equilibrium positions which give rise to a set of vibration waves propagating through the lattice with a specific frequency. If the interatomic distance changes, the frequency also changes and the Raman peaks shift to

higher frequencies. SiC is weak polar system [11] and hence the LOPC mode may be detected, essentially for high carrier's concentration. Micro-Raman spectroscopy (μRS) measurements were performed on Mn-implanted samples in attempt to deduce the effect of ion implantation on the structure of SiC. Figure 3.12 and Figure 3.13 show respectively the first order and second order Raman spectrum of a virgin sample. The first order Raman spectrum exhibiting three intense bands at 766, 787 and 966 $cm^{-1}$, typical fingerprint of 6H-SiC[87, 89].

The Raman peaks of the second-order Raman spectra are marked as a (1477$cm^{-1}$), b (1514$cm^{-1}$), c (1530$cm^{-1}$), d (1543$cm^{-1}$), e (1580$cm^{-1}$), f (1618$cm^{-1}$), g (1651$cm^{-1}$), h (1683$cm^{-1}$) and i (1712$cm^{-1}$). The first order Raman spectra of SiC are polytype dependent and the Raman frequency peaks depends on the doping concentration, whereas the doping concentrations have no influence on the second order Raman scattering of SiC crystals [85, 86]. It is found that the first order Raman peaks of doped 6H-SiC shift to different frequencies, especially the peak at ~ 964 $cm^{-1}$ [87, 88] depending on the type and concentration of free carriers. So, we expect significant changes in the shape and position of this peak as a function of doping concentration.

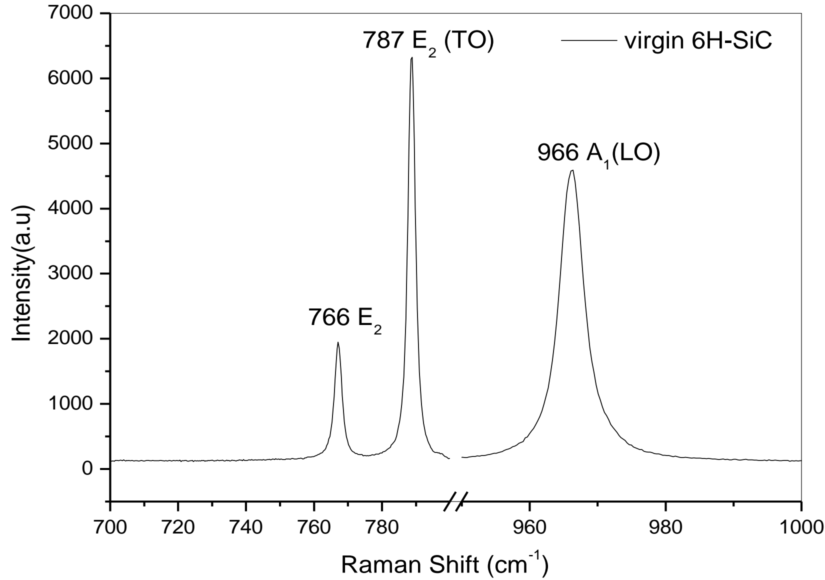


*Figure. 3.14. First-order Raman spectra of undoped 6H-SiC sample.*

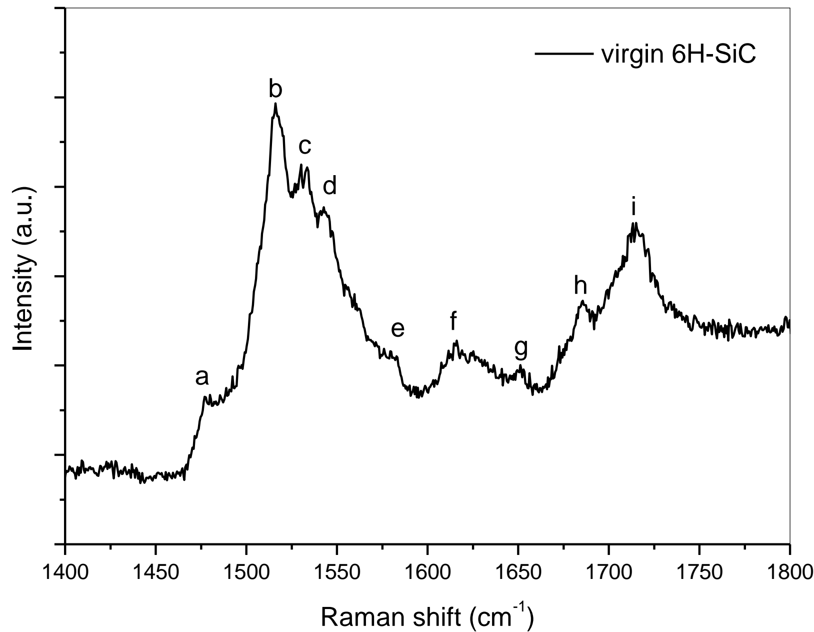


*Figure. 3.15. Second-order Raman spectra of undoped 6H-SiC sample.*

Figure 3.14 show the A1(LO) modes of the three samples (virgin, $5\times10^{15}$ and $1\times10^{16}$ Mn/cm$^2$) were carried out under two configurations: axial and polarized direction. It is observed that all peaks of doped samples are centered at the same position as that of undoped one. No shifts or broadening of the lines were observed. There was no evidence

of additional lines or bands appearing after implantation. The Mn concentrations have no influence suggesting that the Raman signal comes principally from the crystalline substrate underneath the implanted layers. This was also observed in 370 keV Si ions implanted 6H-SiC to dose ranging from $5\times10^{15}$ to $1\times10^{16}$ $cm^{-2}$ [90].

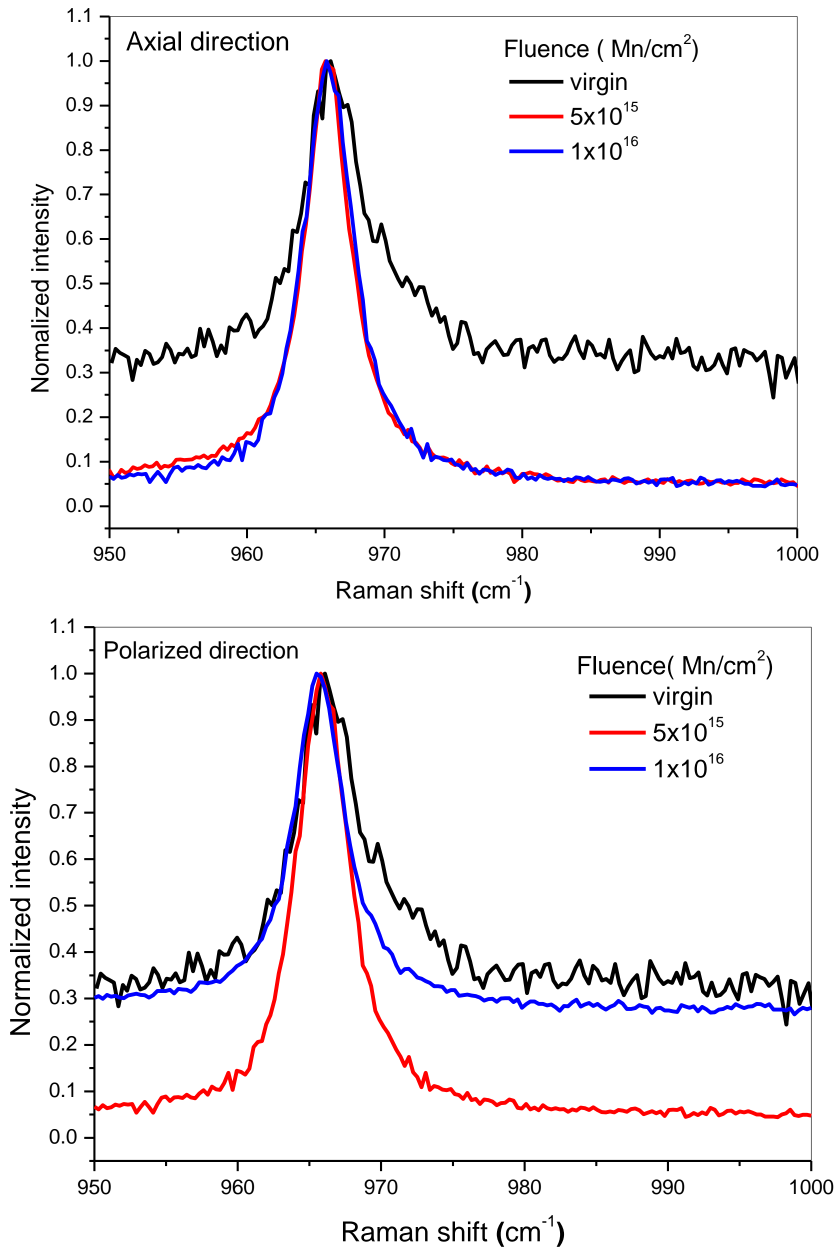


*Figure.3.16. μRS spectra for the three samples (virgin, $5\times10^{15}$ and $1\times10^{16}$ $Mn/cm^2$) in (a) axial direction and (b) polarized direction.*

The absence of frequency shift may be attributed to the small concentration of Mn atoms. Previous study reported a shift in the Raman peaks in 6H-SiC with increasing carrier concentration from ~$10^{16}$ to ~$10^{18}$ $cm^{-3}$ [91]. In our sample, Hall effect measurements were done to calculate the carrier concentrations as a function of fluence. Unfortunately, it was very difficult to perform the measurements for the implanted samples because the implantation area was very small. The calculated carrier concentration of the virgin sample was found to be $(8.1\pm0.3)\times10^{15}$ $cm^{-3}$.

The micro-Raman characterization and analysis have not been pursued further on the as-implanted samples since the possibility of deducing the corresponding signal of the implanted layer was not possible.

## 3.2 Magnetic characterization

In this section, we investigate the magnetic properties of the as-implanted 6H-SiC samples. The aim of this investigation is to correlate the difference of magnetism to the implantation-induced damage. The hysteresis loops are shown in Figure. 3.17. The hysteresis measured using SQUID system was corrected for the diamagnetic background originating from the substrate and sample holder. The magnetization M is normalized to the volume in the implanted region of the as-implanted wafer, whose thickness was taken as the end of range of Mn (about 50 nm). The samples show a ferromagnetic-like behavior. The sample of $1\times10^{16}$ $Mn/cm^2$ shows clear hysteretic one. In contrast, both samples of $5x10^{15}$ and $5\times10^{16}$ $Mn/cm^2$ show very weak hysteretic behaviors. The saturation magnetization corresponds to a magnetic moment per Mn atom of the order of $0.7\mu_B$ for the lowest fluence ($5\times10^{15}$ $Mn/cm^2$). It increases to $1.7\mu_B$ for the intermediate fluence ($1\times10^{16}$ $Mn/cm^2$) and then decreases to $0.19\mu_B$ for the highest fluence ($5\times10^{16}$

$Mn/cm^2$) (see table3.2). This behavior reflects peculiar dependence of the magnetic moment upon doping concentration.

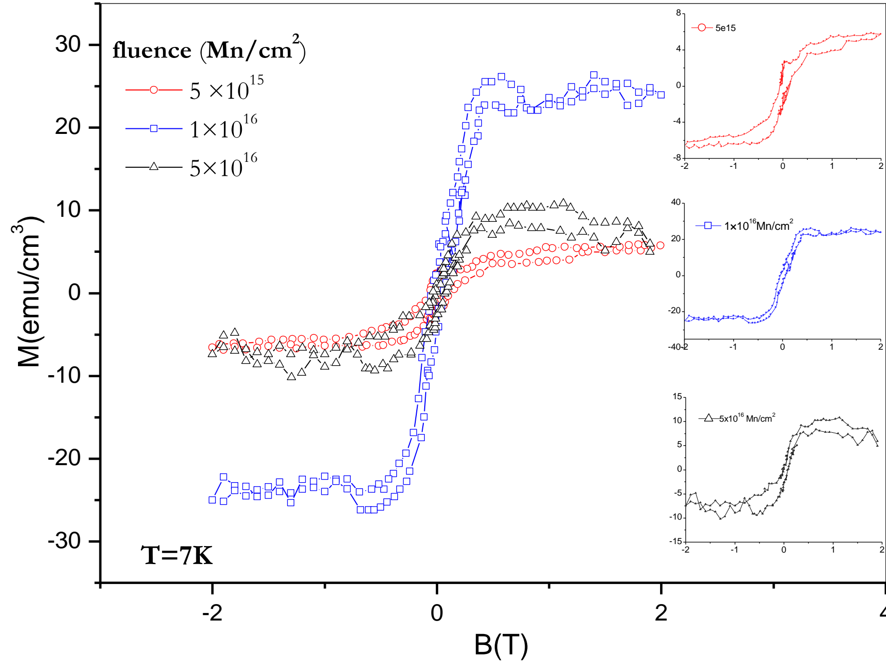


*Figure. 3.17. Hysteresis loops of the samples indicated in the graph recorded at 7 K, the insets are the hysteresis loop for each fluence.*

Some of the behavior could be explained by correlating the magnetism with the structural behavior. As the fluence increases more Mn atoms went into substitutional positions, thereby causing a rise in the moment per Mn till we reach the optimal fluence. Further increase in the fluence leads to amorphazization of the implanted region due to increase of the accumulated damage. At this fluence approximately all the Mn atoms occupy the interstitial positions which suppress the value of the magnetic moment. This scenario is correlated to the *ab-initio* calculations we have performed in this work.

***Table3.2.*** *Accumulated damage parameter $f_D$, percentage of Mn at substitutional site and magnetic moment of Mn implanted 6H-SiC*

| **Fluence $Mn/cm^2$** | **$f_D$** | **Mn (substitutional site)** | **m $\mu_B$/Mn** |
|---|---|---|---|
| $5\times10^{15}$ | 0.16 | 0.41 | 0.7 |
| $1\times10^{16}$ | 0.72 | 0.63 | 1.7 |
| $5\times10^{16}$ | 0.92 | 0 | 0.19 |

The mechanism by which this would happen is not obvious. One can explain the magnetic behavior as follows; for the lowest fluence, most of the Mn atoms occupy C sites where the Mn atoms have small magnetic moments. As we increase the fluence to $1\times10^{16}$ $Mn/cm^2$, more Mn atoms will occupy Si sites which enhance the magnetism due to the large magnetic moment of Mn at Si site. The preference of Si site for magnetic substitution and larger value of the magnetic moments in this case was found in previous studies [32]. Further increase of fluence, increases the number of Mn in interstitial sites which suppress the magnetic moments because Mn atoms at interstitial positions coupled antiferromagnetically to Mn at substitutional site. This is also confirmed by *ab-initio* calculations we have done.

The absence of any secondary magnetic phase, as confirmed by HRXRD studies, has ruled out the possibility of ferromagnetism due to extrinsic origin. Even if some tiny parasitic phase was not detected, the ferromagnetic signal cannot be ascribed to the impurity magnetic phase since nearly all possible Mn–C and Mn–Si compounds are all non-ferromagnetic except $Mn_4Si_7$ which is reported as weakly itinerant ferromagnet with low Curie temperature ($T_C$< 50K) and very low effective magnetic moment

($0.012\mu_B$/Mn)[92-94]. Calculations by Miggs et al. [95] have shown that $Mn_4Si_7$ has zero magnetic moment and a nonmagnetic ground state.

In conclusion, the structural and magnetic properties are correlated. Mn implantation induces different types of defects that control the magnetic properties. We noticed that by increasing Mn at substitutional site, the magnetic moments increases. As we further increase the Mn fluence, accumulated damage increase and the system loses its crystallinity which suppress the fraction of Mn at substitutional sites and therefore decreasing the value of the magnetization.

In order to understand the origin of magnetism in our samples, we have carried *ab-intio* calculations using different configurations of Mn in 6H-SiC. The results obtained confirm the preference of Si sites for Mn substitution. The interstitial sites with C neighbors are more favorable than that with Si neighbors. These results will be discussed in details in the last section of this chapter.

One of the major issues in implanted systems is to retain the semiconducting electronic structure while doping the system with magnetic impurities. Usually the implantation, as observed from the above results, induces large damages and strain that can affect the intrinsic structure and therefore the band structure of SiC. In order to recover the crystalline structure and anneal out defects, subsequent annealing at different temperature was performed in such way that we can investigate the diffusion of Mn and various defects (interstitials, vacancies, and complexes). As shown from *ab- initio* calculation, it is expected that Mn will go to Si substitutional site which is more energetically favorable, and in turn should contribute to the enhancement of magnetism. This study is presented in the following section.

## 3.3 Subsequent thermal annealing treatment

The as-implanted samples were annealed using high frequency induction furnace. The post implantation annealing was performed in $N_2$ atmosphere at 1600 $^oC$, for 10 minutes under a vacuum of ~ $5\times10^{-6}$ mbar. After annealing, the samples have been characterized again using RBS, μRS and SQUID techniques. It is important to stress out that the main purpose of this two-step process (implantation + annealing) is to eliminate the implantation-induced disorder. The degree of the structural recovery depends on the annealing temperature as well as annealing time. In this study the annealing was performed at very short time in order to prevent Mn diffusion and possible clustering. Several previous works were carried out to study the effect of annealing on the magnetic and structural properties of ion implanted SiC. The results obtained are summarized on table (A.1) in appendix A. We note that the annealing behavior is complex and is related to different processes: annealing of point defects, relaxation, and annealing of amorphous clusters especially in the heavily damaged samples. The presence of different chemical species and defect concentrations makes the recrystallization process in SiC difficult. Annealing of point defect and relaxation may be achieved at annealing temperature of ~ 1100 $^oC$. For examples, the short distance order is achieved in a highly damaged 4H-SiC implanted with Al after annealing at 1100 $^oC$ in $N_2$ for 1h [36] and for Ni implanted 4H-SiC and annealed at 1100 $^oC$ for 40 min [34]. It was found that very limited recovery occurs in amorphous SiC even at 1200 $^oC$ [96] while a good recrystallization without dopant loses was found after annealing of Al implanted 6H-SiC at 1700 $^oC$ [43]. The annealing of Al implanted 6H-SiC at 1550 $^oC$ for 30 minutes suppress the implantation induced amorphous layer [39]. For the Fe implanted SiC, results are contradicting, while some

groups reported that at high annealing temperature (1500-1600 °C), the implanted species diffuse out and are lost through the surface [97, 98], another group reported the redistribution of the Fe atoms, but a significant fraction is incorporated into the recrystallized lattice[38]. Luo et al [99] studied the annealing of different type of defects created due to implantation and annealing process. They found that all the electron irradiation-induced primary and secondary defects were annealed out at the temperature of 1600 °C.

From these studies, we conclude that the recovery of all type of defects induced by implantation takes place at temperature between (1600-1700°C). So, in this work we anneal the samples at 1600°C for 10 minutes and then we characterize them to see the effect of annealing on the structural and magnetic properties.

### 3.3.1 Structural characterization

Figure 3.18 displays the RBS/C SiC spectra of 1600°C annealed samples for different fluencies as compared to virgin sample. A drastic change seen in Figure 3.18 is related to the total disappearance of Mn signal upon thermal annealing at 1600°C in contrast with what is reported in literature [100] for Mn implanted 4H-SiC. In Mn-implanted 4H-SiC with 300KeV to a fluence of $1\times10^{16}$ atom/$cm^2$ and subsequently annealed between 1400°C and 2000 °C during 15 mins in Ar atmosphere using RF-furnace, a substantial rearrangement of Manganese is observed in the implanted region.

The other observation is the appearance of an additional peak (indicated by arrows) in all samples after annealing which may be due to the formation of secondary phases. Indeed, recent results on annealed Mn-doped SiC films by Yukai An et al [101] show the formation of a secondary phase, namely $Mn_4Si_7$, after annealing at 1200°C. The intermediate

position of the later peak around 500 keV between that of C and Si may suggest that C atoms have been incorporated in the $Mn_4Si_7$. This phase is shown to be ferromagnetic above room temperature in the same work.

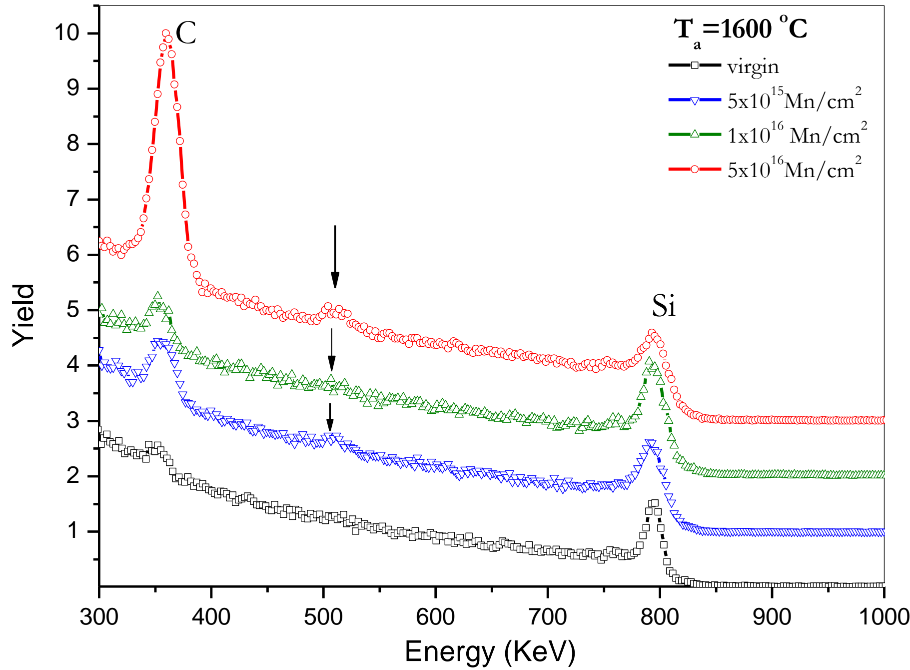


*Figure. 3.18. RBS/C spectrum for implanted samples annealed at 1600$^0$C. The spectrum of the virgin sample is shown here for reference. The arrow points to the peak appearing at around 500 keV after annealing that may be due to a secondary phase.*

Figure 3.19 shows the comparison between the RBS/C spectrum for each fluence before and after annealing. The reduction of the Si yield is clear in figure 3.19 and it is an indication of the damage recovery after thermal treatment. As we discussed in section (3.1.1) the main defects introduced by Mn implantation into 6H-SiC are point defects such as vacancies and interstitials (Si, C, Mn). The vacancy related defects peak disappeared after thermal annealing treatments at 1600$^0$C. This can be described by the thermal diffusion of $V_{Si}$ and $V_C$ vacancies at high temperature. It is found that the $Si_I$ and $C_I$ diffuse faster at elevated temperature than the lattice atoms which makes the

recombination of the $Si_I$ and $C_I$ atoms with their vacancies more probable. This indicates a substantial decrease of disorder.

we also notice the increase of the C yield after thermal treatment indicating more carbon segregation at the surface of samples. This may be due to two possibilities; the formation of graphene phase as observed in similar samples [22] or the decomposition of SiC, with Si evaporating leaving C behind. The later possibility can be excluded because the decomposition of SiC was observed at temperature above 1600°C [102, 103].

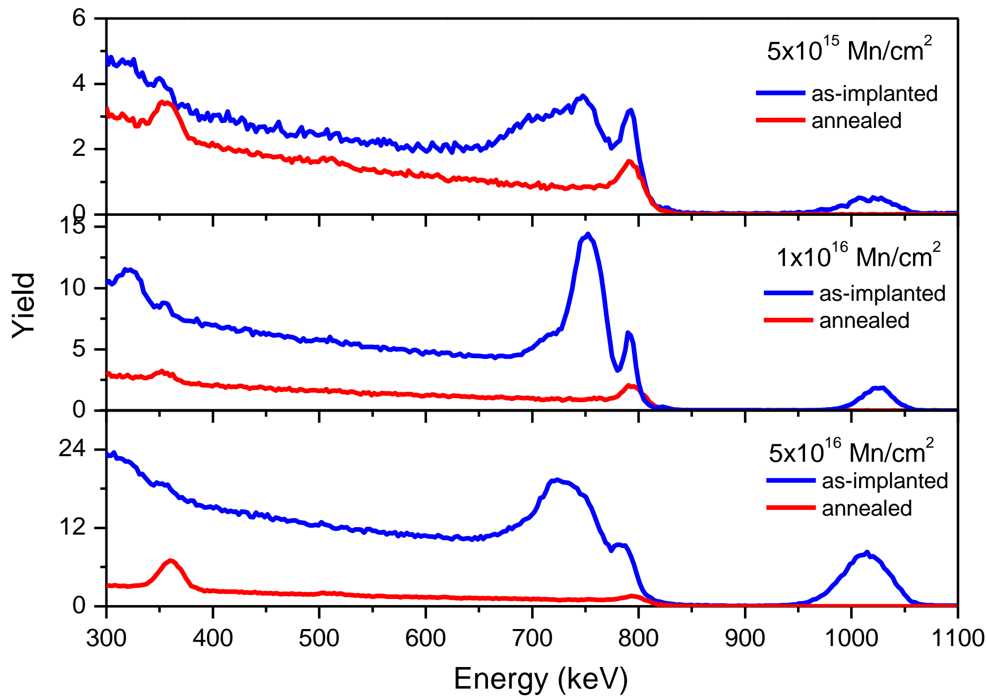


*Figure. 3.19. RBS/C spectrum for samples B,C and D before and after annealing at 1600°C.*

One open question arising from the disappearance of the Mn signal was whether Mn has segregated to the surface and then evaporated, or has diffused to the volume of SiC resulting in strong Mn dilution. In attempt to answer this question, Electron Probe Micro Analysis in the Energy Dispersive X-ray Analysis mode (EPMA-EDX) measurements was performed on the $5\times10^{15}$ Mn/cm$^2$. The corresponding results are displayed in Figure

3.19. The advantage of this technique is the possibility, by varying the incident electrons energy, to have a selective sensitivity about the depth profile chemical composition of the investigated sample.

In this respect, three energies of the electrons were used: 5 keV, 10 keV and 20 keV. The respective calculated penetration depths of the incident electrons are: 220 nm, 920 nm and 3µm.

As one can see, the *L* alpha line of Mn is clearly observed, especially for 5 keV. As the penetration depth increases, the Mn signal weakens. These results show that Mn is still in the initial implanted SiC (and therefore its diffusion versus annealing was rather localized) and explain why magnetic signal is still observed even though no Mn was observed by RBS. This can be attributed to the formation of Mn clusters or Mn-Si-C alloys well localized and therefore difficult to detect using directional probe technique such as RBS.

The disappearance of Mn signals after annealing from RBS spectrum can be attributed to the decrease of Mn concentration to a value below the detection limit of RBS which vary from $5\times10^{12}$ ion /$cm^2$ (Z = 20) to $2x10^{10}$ ion /$cm^2$ (Z = 80) [104]. The effect of annealing on the magnetic properties of the samples will be discussed in the next section.

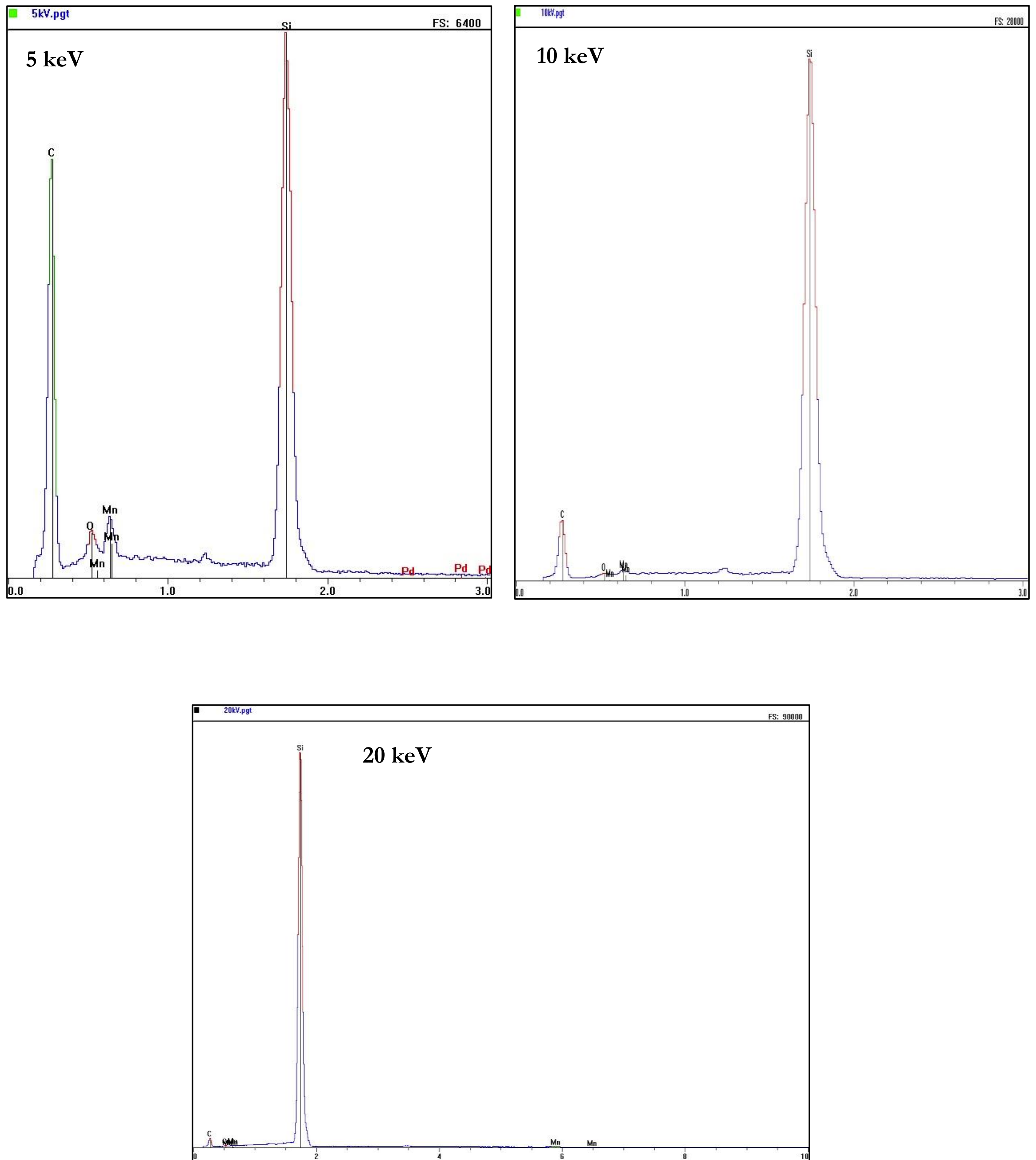


*Figure. 3.20. EPMA- EDX measurements of the $5\times10^{15}$ Mn/cm$^2$ at three different electrons energies: 5, 10 and 20 keV.*

### 3.3.2 Magnetic properties

Figure 3.21 shows the field dependence of the magnetization measured at 7K for the as-implanted sample and annealed samples. The magnetization exhibits a clear saturation at high magnetic fields for all samples indicating ferromagnetic like behavior. There is a clear significant decrease in the magnetization of all samples after annealing as shown in Figure (3.22). The ratio of saturation magnetization of annealed and as-implanted samples ($M_{s\text{-anneled}}/M_{s\text{-as implanted}}$) are 0.29%, 0.36% and 0.14% for $5\times10^{15}$, $1\times10^{16}$ and $5\times10^{16}$ Mn/cm$^2$ respectively. The existence of this ferromagnetic like behavior is a good evidence that Mn atoms still exist within the sample after annealing. The formation of secondary phases after annealing cannot be excluded. $Mn_4Si_7$ phase had been observed after annealing at 1200°C [101]. Since the secondary phase $Mn_4Si_7$ is a weak ferromagnet, this will lead to the reduction of Mn atoms contributing to the sample ferromagnet. Previous study of the effect of annealing on the Mn in SiC found that Mn may migrate with a high rate, but at a low concentration in the undamaged region after heat treatments at 1400 and 1600$^0$C for 15 mins [100].

The magnetization maintains its fluence dependence as before annealing. The intermediate fluence still exhibits higher magnetization compared with other two fluences.

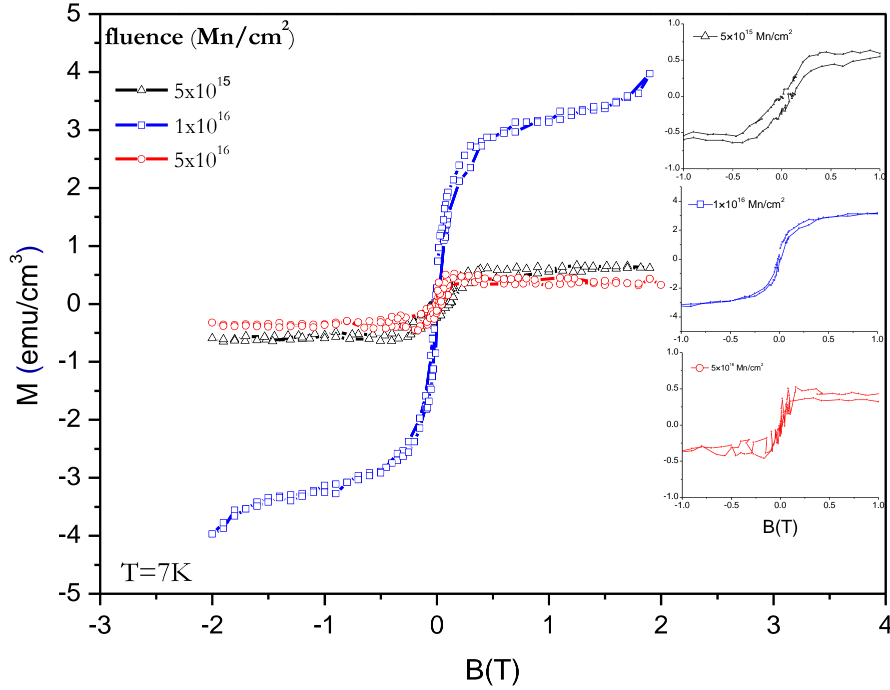


*Figure. 3.21. Hysteresis loops of the annealed samples recorded at 7 K.*

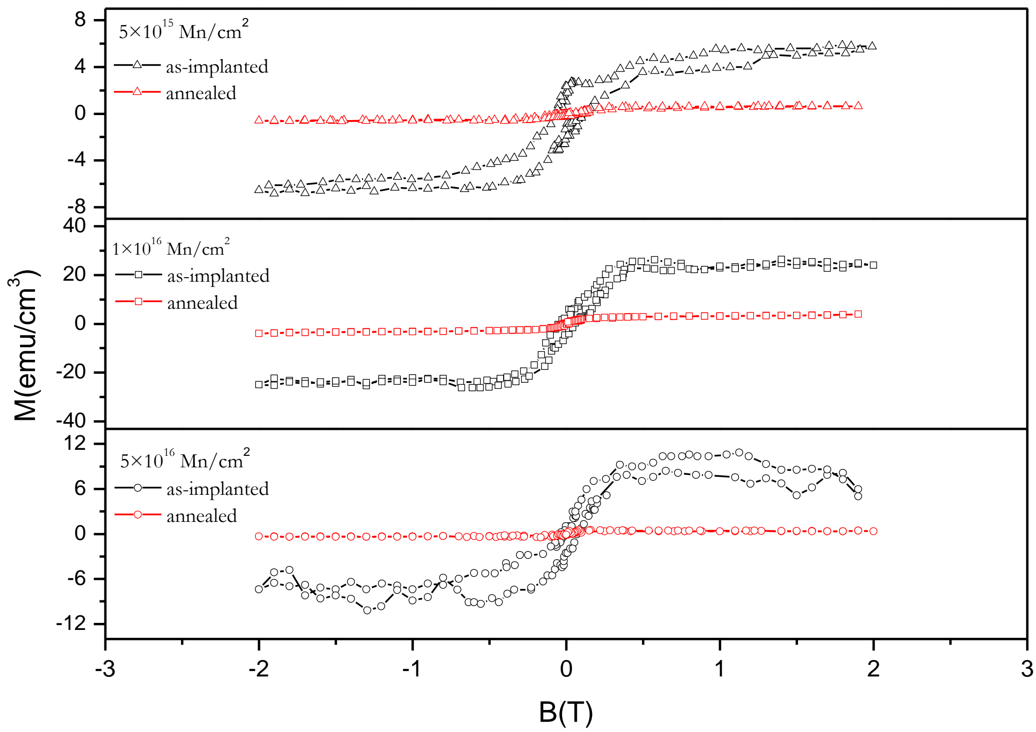


*Figure. 3.22. Hysteresis loops of the samples recorded at 7 K before and after annealing at 1600 $^oC$.*

In order to estimate the magnetic moment per Mn atom (Bohr magnetron per Mn atom) for samples annealed at 1600°C, one needs to evaluate the Mn concentration. Since there are no measurements of diffusion of Mn in SiC versus temperature, we estimated the concentrations of Mn by using the average diffusion constant of transitions metals in 6H-SiC which is ~ $2.0\times10^{-12}$ $cm^2/s$ at 1300 °C [105]. The estimated values of $C_{Mn}$ and $\mu_B/Mn$ are summarized in table (3.3).

***Table 3.3.*** *The estimated values of $C_{Mn}$, the saturation magnetization and the magnetic moment of the annealed samples.*

| **Fluence**<br>**$Mn/cm^2$** | **$C_{Mn}$**<br>**(at.%)** | **$M_s$**<br>**($emu/cm^3$)** | **m**<br>**$\mu_B/Mn$** |
|---|---|---|---|
| $5\times10^{15}$ | 0.034 | 0.58 | 0.2 |
| $1\times10^{16}$ | 0.06 | 3.13 | 0.7 |
| $5\times10^{16}$ | 0.34 | 0.42 | 0.017 |

To confirm that Mn per unit area after annealing was below the detection limit, we estimated the perpendicular distanced covered by Mn atom using the following arguments:

If $N_{Mn}$ is the number of Mn atoms, the total volume occupied by Mn atoms is given by:

$$V = AL.N_{Mn} = v_{Mn}.N_{Mn} = \frac{4\pi}{3}r^3 .N_{Mn} \quad (3.3)$$

Where A is the area of the sample and L is the distance covered by Mn atoms, r is the radius of the region occupied by a single Mn atom and can be written as:

$$r = \left(\frac{3}{4\pi}\frac{V}{N_{Mn}}\right)^{\frac{1}{3}} \qquad (3.4)$$

That means that the cross-sectional area per Mn atom equals:

$$A_{Mn} = \pi r^2 = \pi\left(\frac{3}{4\pi}\frac{V}{N_{Mn}}\right)^{2/3} \qquad (3.5)$$

Hence, the number of Mn atom per unit area is:

$$\frac{A}{A_{Mn}} = \frac{A}{\pi\left(\frac{3}{4\pi}\frac{V}{N_{Mn}}\right)^{2/3}} = \frac{A}{\left(\frac{3}{4\pi}\frac{AL}{N_{Mn}}\right)^{2/3}} = \frac{1}{\pi}\left(\frac{N_{Mn}}{3/4\pi}\right)^{\frac{2}{3}}.\frac{A^{\frac{1}{3}}}{L^{\frac{2}{3}}} \qquad (3.6)$$

We assume that Mn per unit area equal $10^{12}$ atom/cm$^2$ which is the detection limit of RBS. The average calculated distance equals $(5.0 \pm 0.2)\times 10^{-4}$ cm which corresponds to a diffusion constant of $(1.92\pm0.53)\times10^{-10}$ cm$^2$/s. This value is reasonable compared with the value used in this study if we take into account the difference in the implantation method and the annealing temperature which is greater by 300 $^o$C .

The other possible sources of the observed magnetism are the secondary phases (Mn-Si) or (Mn-C) that can be formed after thermal treatment or the formation of graphene phase. To confirm the existence of these phases, HR-XRD and μRS measurements have been done on the annealed samples. More recently it was suggested that carbon incorporation in Mn-Si compounds induces ferromagnetic order with a $T_C$ above RT [106, 107]. The origin of the ferromagnetism induced by the presence of carbon was recently explained as an effect of the anisotropic modification of the local structure around the Mn sites by carbon. The Raman spectra of all carbons show several common features in the 800-2000

$cm^{-1}$ region, the so-called G and D peaks, which lie at around 1560 and 1360 $cm^{-1}$ [22]. That means it may overlap with second order spectra of 6H-SiC. Comparison of Raman spectra associated to as-implanted and annealed $5x10^{16}$ $Mn/cm^2$ (Figure 3.23) sample did not show any obvious difference between the two spectra. No apparent peak corresponds to graphene, which exclude the possibility of the origin of ferromagnetism due to the graphene phases.

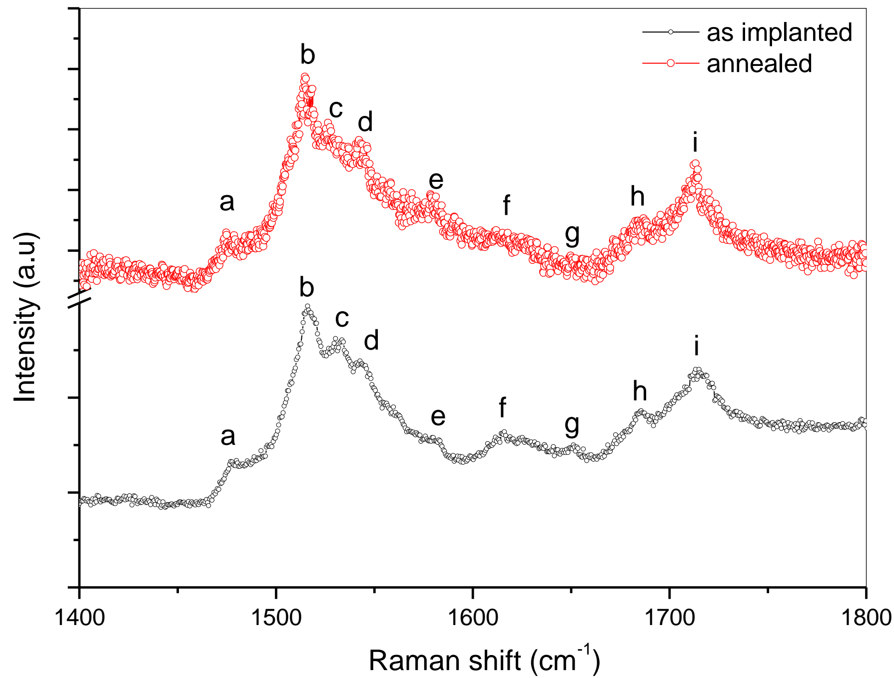


*Figure. 3.23. Second-order Raman spectra of $5\times10^{15}$ $Mn/cm^2$ sample before and after annealing.*

Figure (3.24) also shows the micro-Raman spectra before and after 1600 $^oC$ annealing for samples C and D. There is no obvious change between the two spectra for the $1\times10^{16}$ $Mn/cm^2$ whereas there is a small shift (~ 0.5 $cm^{-1}$) of the annealed spectra for the $5\times10^{16}$ $Mn/cm^2$. This shift reflects the local relaxation of the system after thermal treatment and confirms the local redistribution or diffusion as discussed above. Therefore, the

ferromagnetism observed in this annealed sample could be due to the lattice relaxation realized by the high temperature post annealing.

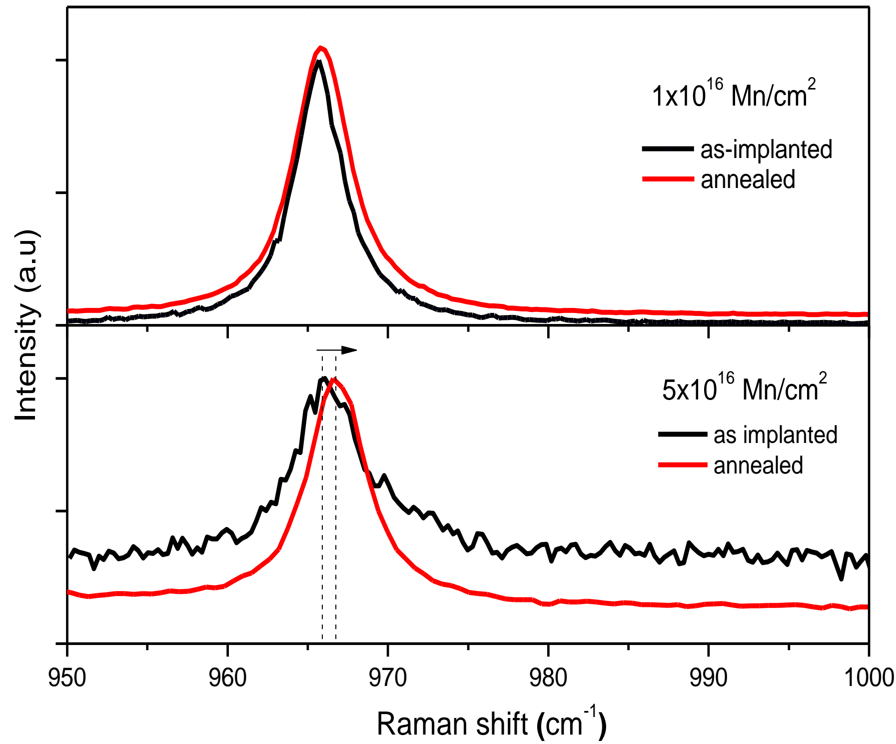


*Figure. 3.24. The first-order Raman spectra LO mode of as-implanted and annealed C and D samples.*

### 3.3.3 Annealing temperature effect

Figure 3.25 shows the RBS/C spectra for the sample implanted with a Mn fluence of $5\times10^{16}$ Mn/cm$^2$ and annealed at different temperature of 800, 1100 and 1600°C, respectively. A slight crystal recovery is observed for annealing at 800°C. With increasing annealing temperature from 800 to 1100 °C, the channeling spectra indicate that the lattice disorder of 6H-SiC substantially decreases. Annealing at 1600 $^{o}$C results in a slight change as compared to annealing at 1100°C, and the channeling spectrum is

almost comparable with the virgin 6H-SiC. This means that the recovery has essentially occurred at 1100°C.

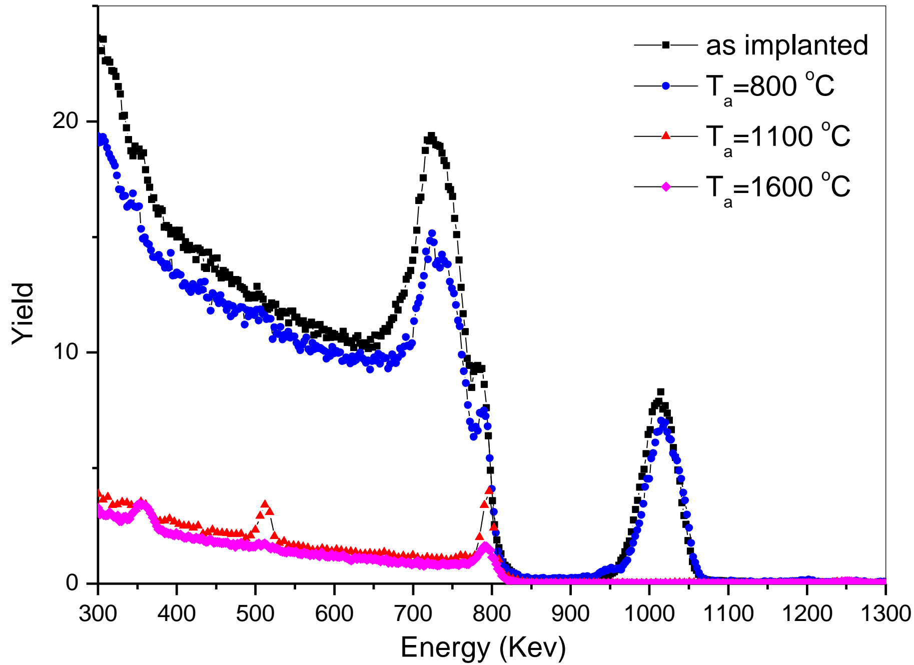


*Figure. 3.25. RBS/C spectrum of 5×10$^{15}$ Mn/cm$^2$ sample annealed at different temperatures.*

Figure 3.26 represents the Si yield and Mn yields for different annealing temperature. For 800 °C annealing temperature, the effect of annealing is rather small as confirmed by XRD scan (Figure.3.27). We notice a small shift on the main peak corresponding to a lattice parameters decreased by about (Δa=0.008Å and Δc=0.11Å) which means that there is very small relaxation effect. There is a decrease in the Si yield, indicating that implantation defects are partially annealed out. We can notice the absence of vacancy related peak after annealing at 1100℃ which may be attributed to the diffusion of Si vacancies (and also C vacancies) and recombination with their atoms.

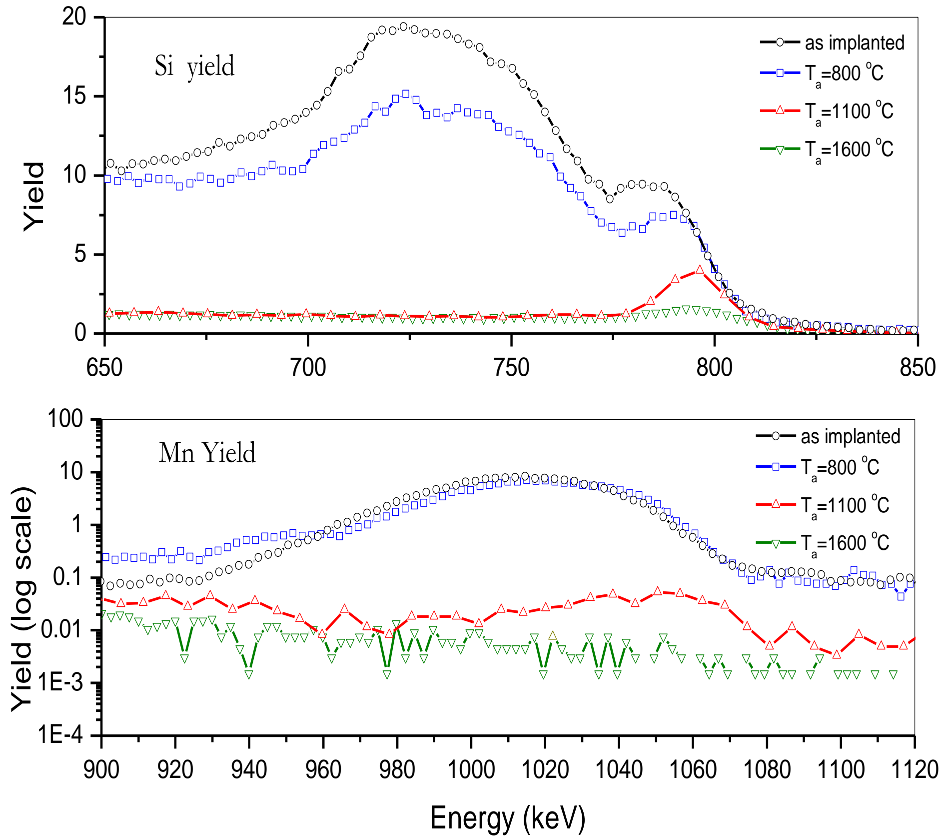


*Figure. 3.26. RBS/C Si yield (upper part) and the Mn Yield (lower part) for $5\times10^{15}$ Mn/cm$^2$ sample annealed at different temperatures.*

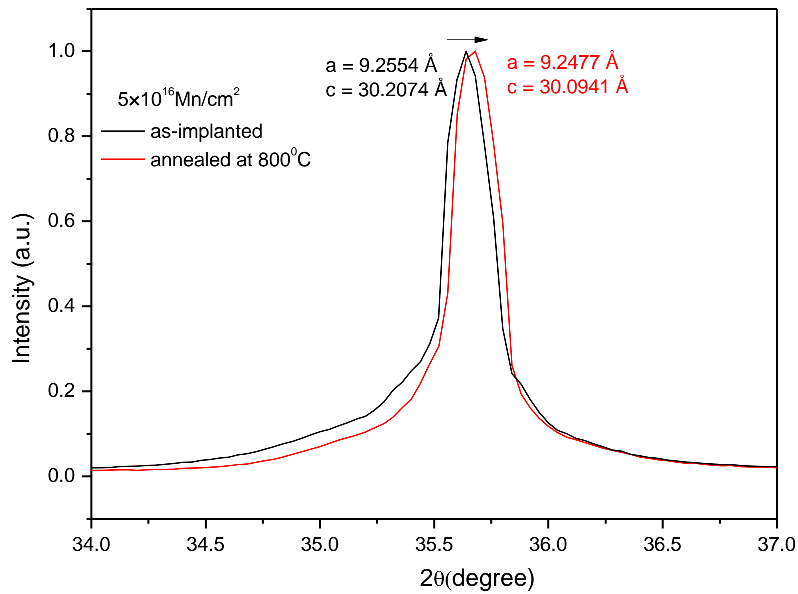


*Figure. 3.27. XRD spectra of $5\times10^{16}$ Mn/cm$^2$ samples before and after annealing at 800°C.*

This also explains the decrease in the Si yield due to $Si_I$-$V_{Si}$ recombination. At 1600 $^oC$, the sample retains its crystalline structure because almost all defects have been recovered. From the Mn yield graph, we notice the decrease of the Mn yield with increasing annealing T. The Mn signal is very low after annealing at 1100 $^oC$ and it disappears completely after 1600 $^oC$ annealing.

Figure 3.28 shows, for the $5\times10^{15}$ Mn/cm$^2$ sample, the magnetization versus field curves recorded at 7 K for different annealing temperatures. The sample exhibits clear hysteresis after each annealing step. However, magnetization decreases with increasing annealing temperature.

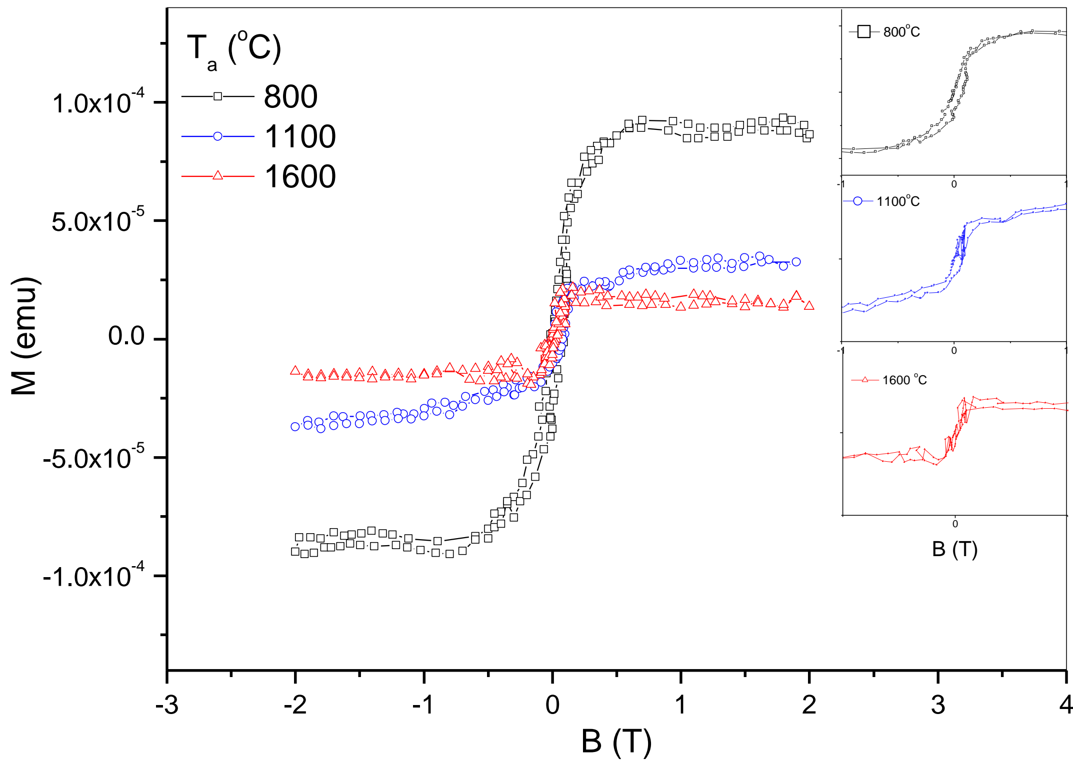


*Figure. 3.28. Hysteresis loops of the $5\times10^{15}$ Mn/cm$^2$ sample annealed at different temperature, the insets are the hysteresis loop for each temperature around zero magnetic fields.*

The observed magnetic behavior on the annealed sample after 1100 and 1600 $^{0}$C may be explained using different scenario.

- As $T_a$ increases, $Mn_I$ diffuses and occupies the substitutional (C/Si) sites whereas interstitial $Si_I$ atoms recombines with $V_{Si}$, Mn at sustitutional (C/Si) sites in this case enhance the magnetism as confirmed from RBS and SQUID measurements .
- The vacancies at neighboring Mn at substitutional sites are annealed. This leads to decrease in magnetic moment because our *ab- initio* calculations showed that the magnetic moment of Mn atom with neighboring vacancy possess more magnetic moment compared to the same configuration without vacancy.
- Before annealing, the Mn atoms are confined to a narrow region in the sample and the ferromagnetic coupling between the Mn atoms is relatively strong. After annealing, the atoms are spread in a larger region which decreases the coupling strength and hence decrease the magnetization. The average interatomic distances between two Mn atoms in as-implanted samples were estimated to be (20Å, 10Å and 5Å for samples B,C and D respectively compared with 40 Å, 30 Å and 20 Å for the same samples after annealing).
- $Mn_I$ and $Si_I/C_I$ forms secondary phases such as manganese silicides or manganese's carbide. From HRXRD measurements, we didn't observe any peaks related to these phases which exclude the possibility of magnetism related secondary phases.
- Mn clustering: Mn may forms small clusters that cannot be detected by RBS (sensitivity of RBS to size)

- Mn segregation to surface, (because the Mn position shifts to higher energy as $T_a$ increases from 800 to 1100 $^oC$).

From this discussion it can be concluded that the Mn ion implantation into 6H-SiC produces different types of defects that play essential role on the magnetic properties of the implanted samples. As Mn fluence increases, Mn in substitutional sites increases to certain fluence. Further increase in the fluence leads to an increase in the accumulated damage that suppresses the magnetization. The maximum magnetic moments obtained related to a fluence of $1\times10^{16}$ Mn/cm$^2$ at which the ratio of Mn at substitutional site was maximum. This suggests that the origin of the observed magnetism is related to the coupling between Mn atoms at substitutional sites. Our results are different from those obtained in Fe implanted 6H-SiC with a fluence of $2.2\times10^{16}$ Mn/cm$^2$. The authors didn't detect any ferromagnetic response in the as-implanted sample, even at low temperature under 1T despite a high level of substitutional fraction of Fe atoms on Si-sites. In our study, increasing the fluence leads to an increase in the point defects and a large fraction of Mn atoms go into interstitial positions where the coupling between them and the substitutional sites is antiferromagnetic.We excluded the possibility of magnetism related secondary phases such as $Mn_4Si_7$ as there was no evidence of second phase formation from HRXRD measurements. The post implantation thermal treatments were done in order to study the effect of temperature on the structural and magnetic properties of the implanted samples. The results showed a very limited recovery after annealing at 800 $^oC$ indicating that the damage is stable to at least at that temperature. Almost all defects have been removed after annealing at 1100 $^oC$ as confirmed from RBS measurements. The Mn couldn't be detected by RBS after annealing at 1100 $^oC$ in contrast with Fe implanted 6H-

SiC and annealed at 1300 $^{o}$C [21] and 1500 $^{o}$C [41]. The Mn signals was detected using EPMA- EDX measurements which confirm that Mn is still in SiC samples. The decrease in the magnetization for all samples after annealing at 1600 $^{o}$C was attributed to the diffusion of Mn atoms and vacancies. Due to the diffusion of Mn atoms deeper toward undamaged region, the distance between Mn atoms increases which suppress the coupling between them. On other hand, the diffused $Mn_I$, $Si_I$ and $C_I$ atoms can recombine with the vacancies in the substitutional sites which also lead to a decrease in the magnetic moment of Mn atoms at ideal substitutional sites. At high temperature ≥1100°C, the formation of secondary phases was expected as confirmed from previous study of Mn implanted 3C-SiC [101]. In that study, the authors reported the formation of $Mn_4Si_7$ phase after annealing at 1200°C and they attributed the magnetic signals obtained to the secondary phase. But in our annealed samples, we couldn't detect any secondary phases from HRXRD measurements.

It is clear for us that the defects play the major role in the magnetic properties of the as-implanted and annealed samples. To have a clear picture about the correlation between structural and magnetic properties, we investigated the structural properties and magnetism of Mn-doped using *ab-initio* calculations. Various configurations of Mn site and vacancy type have been considered. The coupling effect (Ferromagnetism, Antiferromagnetism) between the Mn atoms with and without neighboring vacancy, with Mn at substitutional and/or interstitial sites were explored. In addition, the effect of distance between two Mn atoms on the strength of magnetic interaction was explored. The results obtained will be discussed in the next section.

## 3.4 Ab-initio calculations results

In attempt to shed more light of the experimental magnetic features of our samples, we have performed *ab-initio* calculations. The calculations were carried out by means of the self-consistent full-potential linearized augmented-plane-wave method (FLAPW) using the WIEN2K package [68].

The embedded impurities in SiC are modeled by a 2×2×1 supercell (see Figure.3.29). The muffin-tin radii (RMT) were chosen as 1.66 au for both Si and C and 1.77 au for Mn. An optimum number of k-points was reached by testing the convergence of the total energy and the electric field gradient for the basic unit cell of 6H-SiC with two Mn as substitutional atoms. The supercell calculations were performed with an energy cut-off such that RMT×$k_{max}$ = 6.0 and a k sampling with a 8×8×2 Monkhost–Pack mesh. The Kohn–Sham equations were solved using the Perdew–Burke–Ernerhof GGA approximation [72]. The self-consistent procedure has been done using 64 k-points in the irreducible BZ. Further increase in the cut-off value, basis set and the k-points number did not lead to any noticeable change in the eigenvalues. The self-consistent cycles were stopped when the total energy difference between successive cycles is less than 0.0001Ry and the charge density difference between successive cycle is $10^{-4}$.

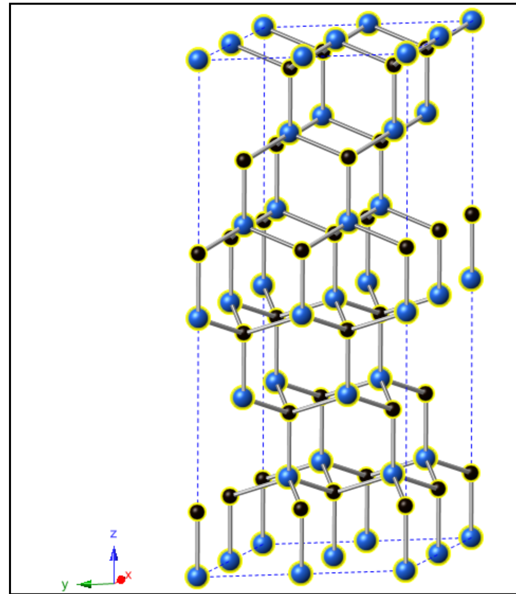


*Figure. 3.29. The supercell used in the calculation*

Three different cases have been studied including the density of state of virgin 6H-SiC, the magnetic moments and density of states of one Mn impurity at Si/C sites with or without vacancy at neighboring C/Si site and the coupling effect (Ferromagnetism, Antiferromagnetism) between the atoms in the presence of vacancy, with Mn at substitutional and/or interstitial site. The relaxation effect on the magnetic ordering was also explored.

### 3.4.1 The electronic structure of virgin 6H-SiC

The total and projected Density of states (DOSs) of undoped 6H-SiC are shown in Figure (3.30). As we can see from Figure (3.30), the full band can be divided into two subbands, separated by a gap of about 2.0 eV. The first part, starting from the bottom of the valence band to −10.19 eV, is composed mainly of the localized atomic C-s states with a small mixture of Si-s and Si-p states. The second part constituting the valence band starts from -8.42 eV and mainly consists of C-p and a mixture of Si-s and Si-p states. The conduction band consists of a mixture of Si-spd and C-sp states. The total and partial densities of states are very similar to the density of states spectra of pure 6H-SiC calculated using the FLAPW techniques and presented in ref [28]. 6H-SiC is an indirect band gap semiconductor, with experimental value of 3.04 eV. Our calculations give a smaller band gap of about 2.0 eV. It is known that the underestimation of the band gap ranges from 32 to 45%, which results from the discontinuity of the exchange correlation energy in the LDA. But our result is in agreement with the best value of band gap found from the calculation of energy gap and valence-band width obtained by Zhenyi Jiang et al. [108].

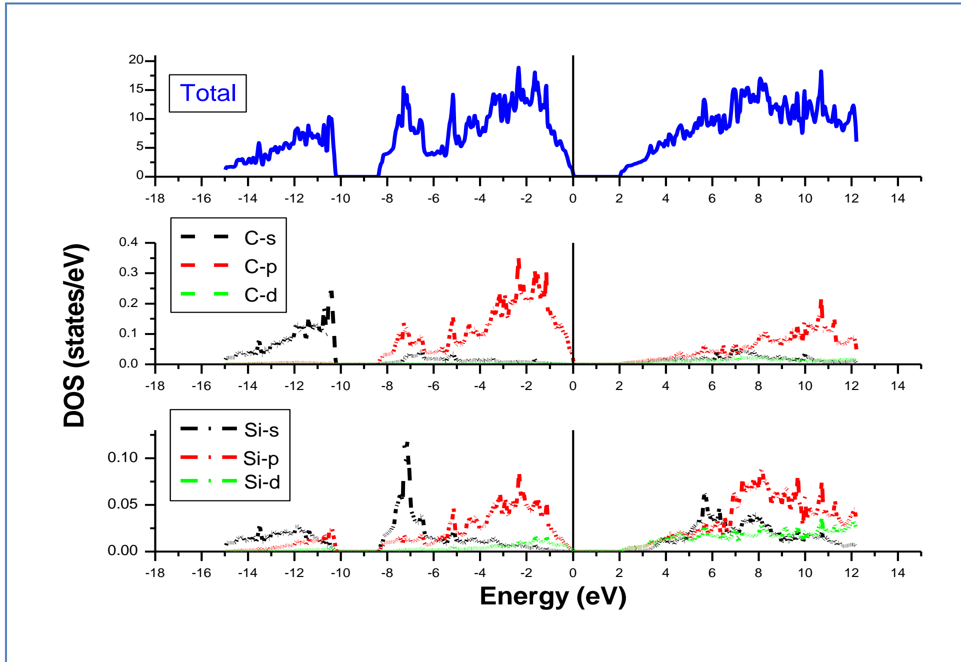


*Figure 3.30. The total (upper panel) and partial densities of states of undoped hexagonal 6H-SiC.*

### 3.4.2 Magnetic moments in Mn-doped 6H-SiC

In order to correlate the calculation with experimental results, we studied different configurations of Mn implanted 6H-SiC. From previous discussion in section (3.1.1), we have observed that Mn implantation produces different types of defects. The main defects introduced by Mn implantation into 6H-SiC are vacancy type defects and interstitials. So, we studied two cases of substitution: (i) Mn at Si/C site without neighboring vacancy, and (ii) Mn at Si/C site with neighboring C/Si vacancy. In addition, Mn at interstitial positions where it can be surrounded by four C/Si atoms was also studied. The calculated energy and magnetic moments for each configuration are presented in table (3.4). The first column represents the substitutional site and the second column is the vacancy site. The energy tabulated is the energy relative to Mn at Si site. MMT refers to the total

magnetic moment of the supercell while MMI refers to the moment within the muffin tin sphere.

***Table 3.4.*** *Energy (eV) and magnetic moments ($\mu_B$) in 6H-SiC doped with Mn atom. MMT is the total magnetic moment of the supercell, while MMI is the magnetic moment per 3d-atom. $Mn_I$(Cnn) refers to Mn at interstitial site with C neighbors and $Mn_I$(Sinn) refers to Mn at interstitial site with Si neighbors. The energies shown are values relative to Mn at Si site.*

| Dopant site | Vacancy site | Energy (eV) | MMT ($\mu_B$) | MMI($\mu_B$) |
|---|---|---|---|---|
| Substitutional site | | | | |
| Si | - | - | 3.00 | 2.31 |
| C | - | - | 1.00 | 0.68 |
| Si | C | 0 | 3.67 | 2.68 |
| C | Si | 8.53 | 2.38 | 1.44 |
| Interstitial site | | | | |
| $Mn_I$ (Cnn) | - | 0 | 3.00 | 1.52 |
| $Mn_I$(Sinn) | - | 2.04 | 0.96 | 0.48 |

A reflection from table 3.4 shows that the calculations of 6H-SiC doped with Mn atoms possess a moment for both types of substitution. However, the magnetic moment differs depending on whether a dopant atom substitutes the C or Si sites. In the case of the absence of vacancy, the magnetic moment of Mn at C site is smaller as compared to that relative to the configuration when Mn substitute Si atom. The values of the magnetic moments obtained are very close to those reported by Shaposhnikov and Sobolev [28]. The energy stability couldn't be compared in this case because the number of atoms in the supercell is different in each configuration. In order to simulate the introduction of defects by ion implantation and to be able to compare the energy stability, the previous configurations were studied with neighbouring Si/C vacancy.

The results show that the configuration of Mn at the Si site with a neighbouring C vacancy is far more stable than the configuration of Mn at the C site with Si vacancy with an energy difference of more than 8.0 eV per Mn atom. We note that Miao and Lambrecht [26] obtained a similar difference in the formation energies for Mn substitutional atoms in 3C-SiC without vacancies. This may be justified by the large differences in atomic radii of Mn and C, on one hand, and their similarities for Mn and Si, on the other hand. The Si site substitution preference is also in agreement with previous studies [26, 28, 29, 109, 110].

Beside vacancy defects, we have also explored the situation where Mn atoms occupy interstitial sites; we notice that the Mn interstitial sites with C neighbors are more favorable than those with Si neighbors with an energy difference of 2.0 eV. The magnetic moment in this case is less compared to the substitutional sites, which explains the decrease of the magnetic moment by increasing the interstitial defects. It should be pointed out that these results are consistent with the experimental results for the as-implanted samples. Indeed, we found that the sample with lower fluence, even though most Mn atoms occupy C substitutional site, the relatively low Mn concentration (0.7%) leads to a small magnetic moment. As the fluence increases, the ratio of Mn atoms occupying substitutional sites increases, corresponding to higher Mn concentration (~2%), and the Mn substitute Si site giving relatively higher magnetic moment. The large difference between the total magnetic moment of the unit cell and the magnetic moment at the 3d-atom in some cases can be explained by the fact that in FLAPW calculations not all the charge is located at the atomic sites but part of it is situated in the interstitial region outside the muffin tin radius. It is clear that Mn behaves differently at the Si and the C

sites indicating the great difference in the microscopic environment around the Mn atoms.

To better understand the difference in the magnetic behaviour between the different configurations, we consider the density of states of Mn in SiC. The formation of substitutional Mn atom can be thought as a two-step process, involving first the removal of a (Si or C) atom, and second the placement of spin-polarized Mn impurity atom in its position. The combined impurity/host orbitals simply results from coupling between the host crystal cation vacancy state (‘’dangling bonds’’ of t (p) symmetry) and the impurity orbitals of the 3d atom filling this vacancy (having t(d) symmetry as well as non-bonding state e(d) symmetry). On comparing the DOS of SiC with C vacancy and SiC with Si vacancy we see that the filled carbon dangling bonds are at upper part of the valence band while the empty levels are in the band gap as reflected in Figure 3.31. On the other hand, the filled dangling bonds of Si are in the band gap while empty levels are in the conduction band (Figure 3.32). The computed DOSs of the C and Si dangling bonds are in a good agreement with previous works[111-113].

The 3d DOS of Mn placed at Si site shows that the main part of minority levels is in the band gap, whereas the 3d DOS of Mn at C site shows the main part of the minority levels in the valence band. Note that majority states are found at the Fermi level for Mn at Si site, while minority states are found at the Fermi level for Mn at C site.

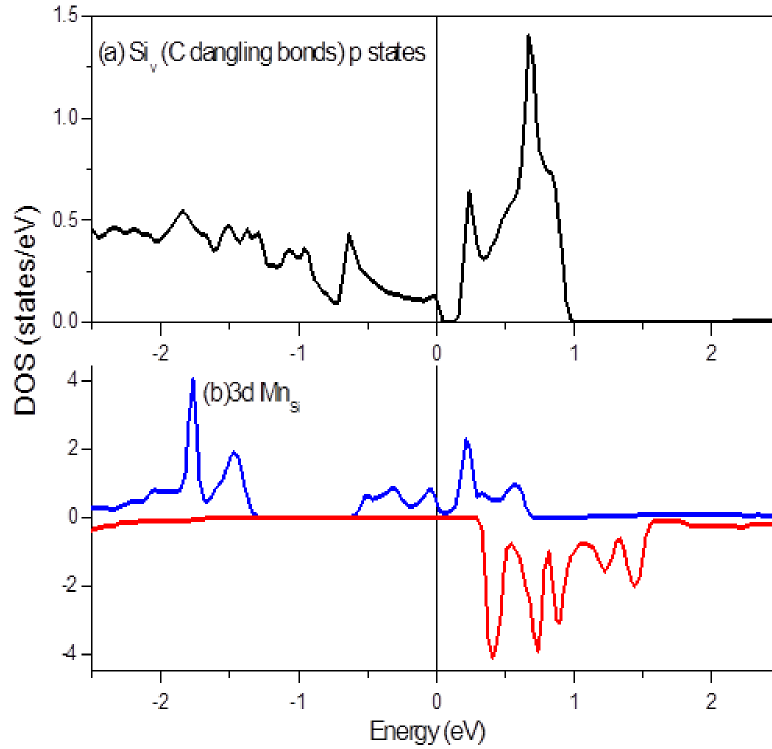


*Figure.3.31. (a) P states of 6H-SiC with Si vacancy, (b) DOS of 3d Mn substitute Si site in 6H-SiC.*

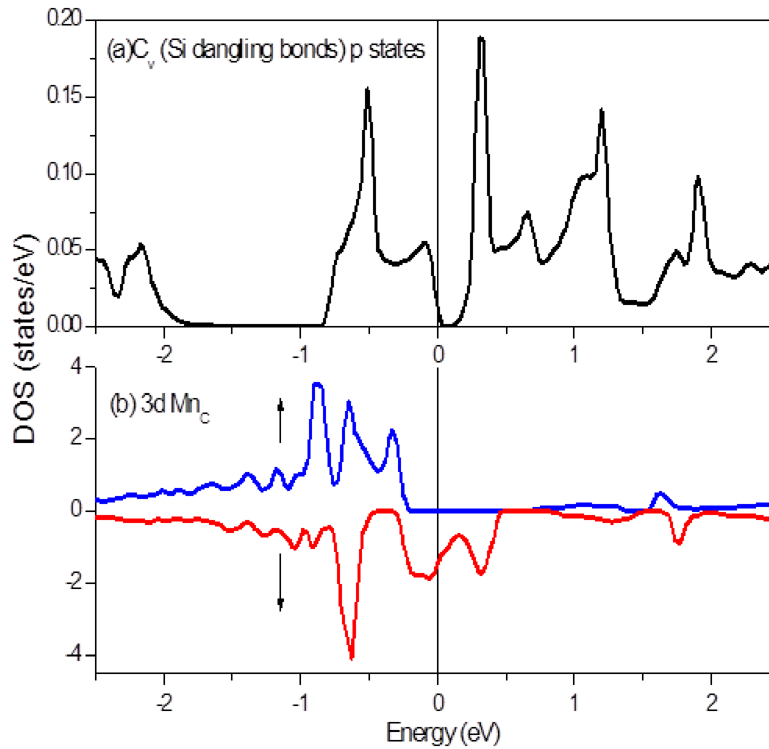


*Figure.3.32. (a) P states of 6H-SiC with C vacancy, (b) DOS of 3d Mn substitute C site in 6H-SiC.*

To explain this electronic structure features we propose the following model shown schematically in Figure 3.33. In this model, we propose that initially the minority level of the Mn atom fall in the gap, below the Si filled density band and above the filled C dangling bonds.

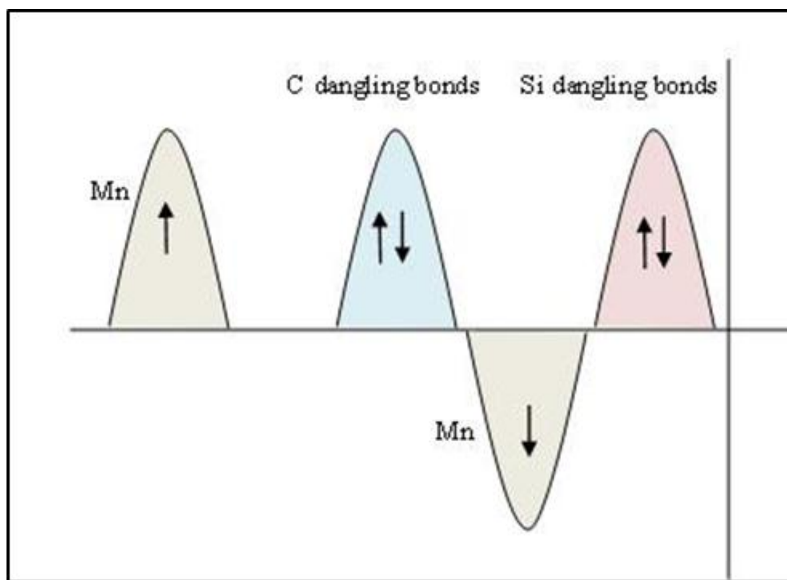


*Figure. 3.33. Energy level diagram of Si/C dangling bonds and 3d Mn level.*

In the case of Mn substitution at the Si site, the coupling between the 3d spin down Mn states and the C dangling bonds pushes the minority levels upward towards the conduction band resulting in electron transfer to the majority levels and hence increasing the magnetic moment at the Mn site. This lead to Mn 3d band structure exhibited in Figure 3.31. In contrast, for Mn at C site, the coupling between the Si dangling bonds and the Mn 3d minority level pushes the minority band towards the valence band closer to the majority band and hence reducing the magnetic moment at the Mn site as reflected in Figure 3.32.

To explain the calculated magnetic moments, a schematic energy-level diagram is proposed in Figures. 3.34a and 3.34b for Mn at the Si site and at the C site, respectively.

It is well known that the crystal field in a tetrahedral environment splits the d levels into a $t_2$ and an e levels with the e level lying below the $t_2$ level. These are further split by exchange-correlation into majority and minority levels. So, two different Mn levels have to be distinguished: A twofold degenerate e-state ($d_{z2}$, $d_{x2-y2}$), the associated wave functions hybridize very little with the valence band t(p)-states for symmetry reasons, and a threefold degenerate $t_2$-state ($d_{xy}$, $d_{yz}$, $d_{zx}$) which strongly hybridizes with the t(p) states resulting in bonding and anti-bonding hybrids. While the bonding hybrids are located in the valence band, the anti-bonding hybrids form the impurity $t_2$-states in the gap. Five d electrons from Mn and four p electrons from the neighboring anions fill the states resulting from the bonding structure. For Mn at the Si site, the C-DB-$t_2$ energy levels are lower than the Mn spin-down $t_2$ levels. From Figure 3.34a, we can see that the coupling between these levels leads to electron filling which gives a net spin of 3/2 and a net magnetic moment of 3 $\mu_B$. The highest occupied level in this case is the $t_2$ majority level. At the C site, the Mn spin-down $t_2$ levels are lower than the Si-DB-$t_2$ levels. By the filling with nine electrons, we obtain a net spin of 1/2 and a net magnetic moment of $1\mu_B$ as shown in Figure 3.34b. The highest occupied level in this case is the e minority state. These results compare well with computed values as shown in table (3.4).

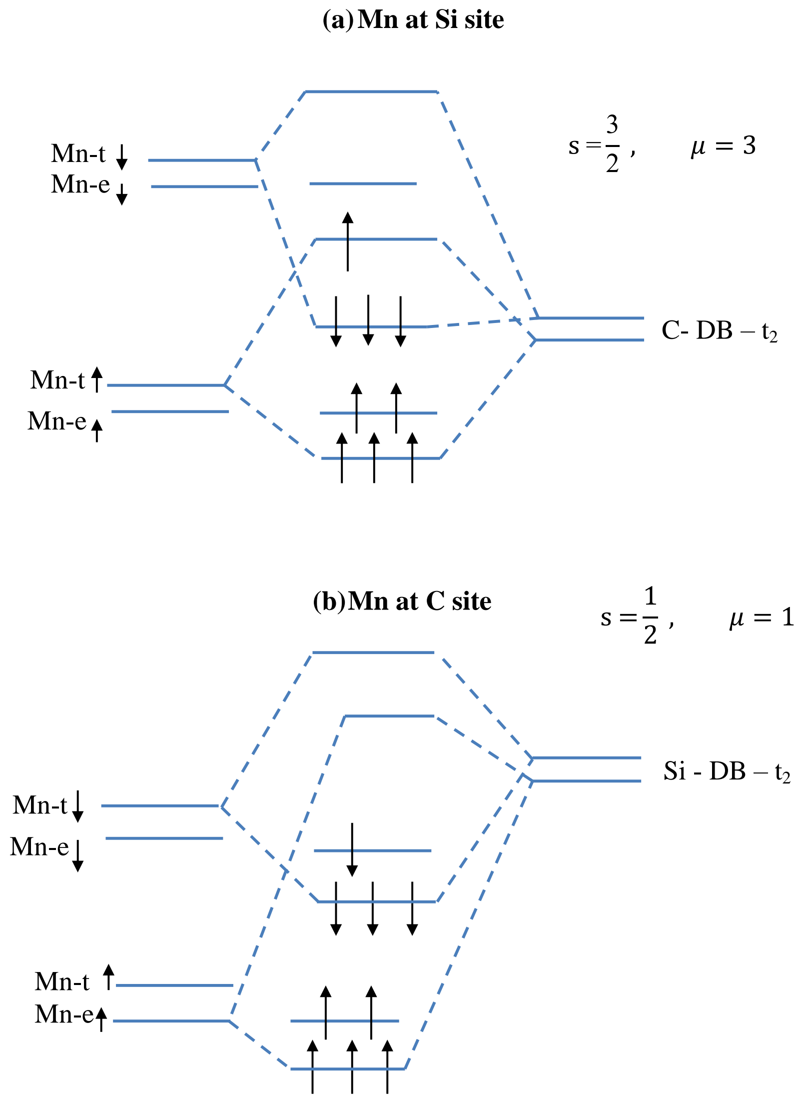


*Figure. 3.34. Energy-level diagram of (a) Mn at Si site and (b) Mn at C site.*

The previous discussion deals with Mn at Si/C sites without neighboring vacancy. The presence of vacancies and interstitials after implantation was confirmed from our experimental work. The total and projected DOS of Mn substitute Si/C site with neighboring C/Si vacancy are shown in Figure (3.35).

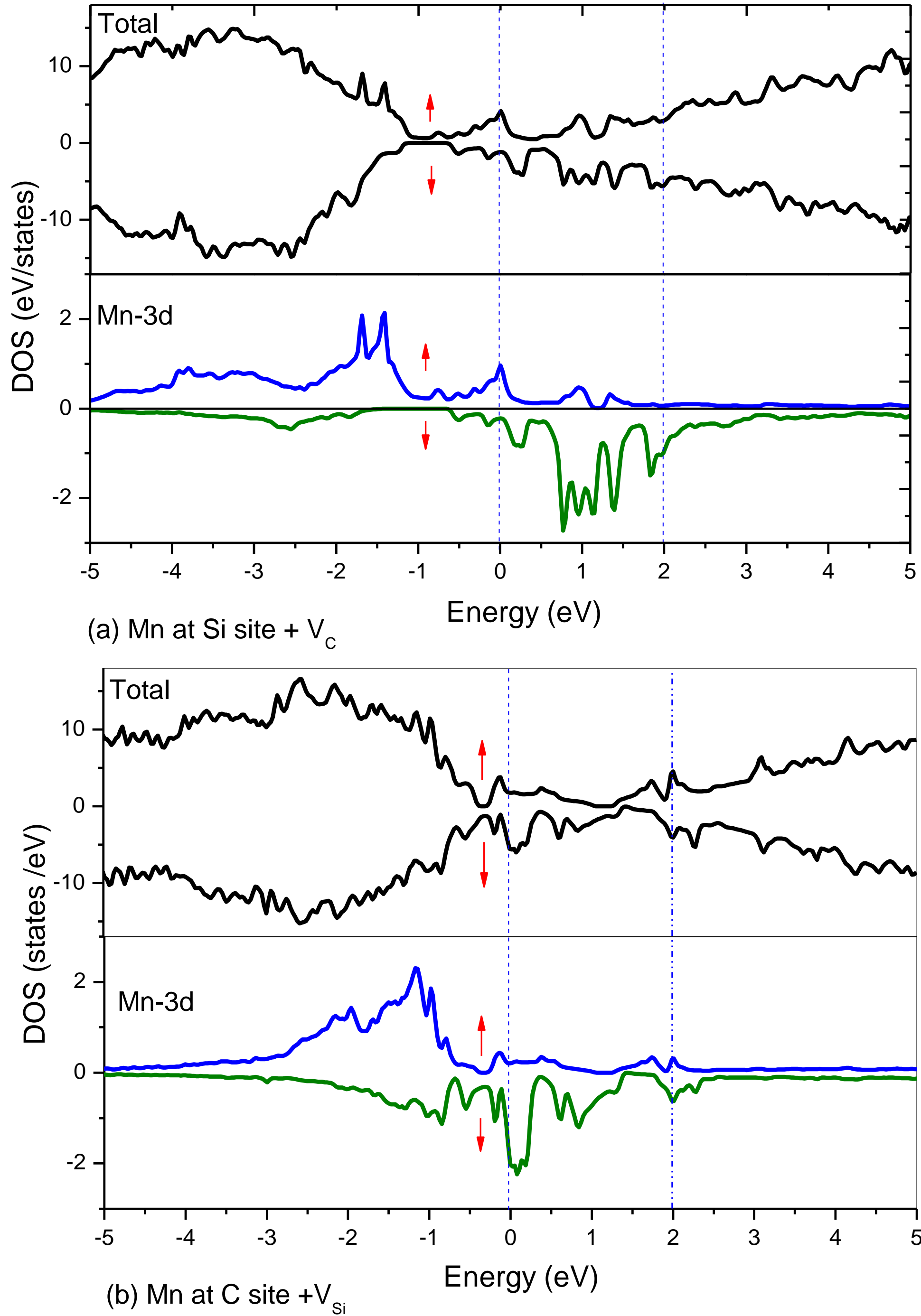


*Figure. 3.35. Total (upper panel) and 3d-Mn (lower panel) densities of states of Mn-doped 6H-SiC. (a) The dopant is at the Si site with neighboring C vacancy and (b) The dopant is at the C site with neighboring Si vacancy. The Fermi level corresponds to the zero of energy.*

Figure 3.35 shows a small shift of the majority level towards the valence band compared with the same configuration without vacancy whereas a shift of the majority level towards the band gap in the case of Mn at C site compared with the same configuration without vacancy is observed. The introduction of vacancy leads to an increase of the magnetic moment for either substitution as indicated in table (3.4) above.

### 3.4.3 Coupled impurities

The implantation can produce several of more or less complicated configurations of host materials, Mn impurities and various types of defects. As can be seen from RBS results from the previous section, the Mn concentration presents a Gaussian depth profile. In other words, the concentration of Mn is not uniform throughout the depth and situations where Mn-Mn short distances are expected. Hence Mn-Mn coupling should also be considered. In previous sections, the magnetic moments calculations were performed for a supercell containing single TM impurity. In this section we use a supercell containing a pair of TM impurities to study which of ferromagnetic or antiferromagnetic coupling will be more favorable. From our result in the previous section and from previous studies [28, 109], it is well established now that the Si sublattice of the SiC lattice is more favorable for TM substitution. Si site substitution preference can be explained according to atomic radii which are much closer for Si and Mn and therefore much smaller lattice distortion would be required in this case. To study the coupling of neighboring Mn atoms in 6H-SiC, we place the two Mn atoms at two neighbors Si sites as nearest neighbors in the supercell (Figure.3.36) with and without common vacancy at nearest C atoms. The calculation of two Mn atoms substituting two

C atoms with and without neighboring Si vacancy for the same supercell has also been included for comparison.

In addition to Mn at substitutional site, the presence of Mn atom at interstitial site has also been explored. This is because at high fluence (high concentration of Mn atom), more Mn atoms may occupy interstitial site and the coupling between Mn atoms at these sites or with Mn atoms at substitutional site may occur.

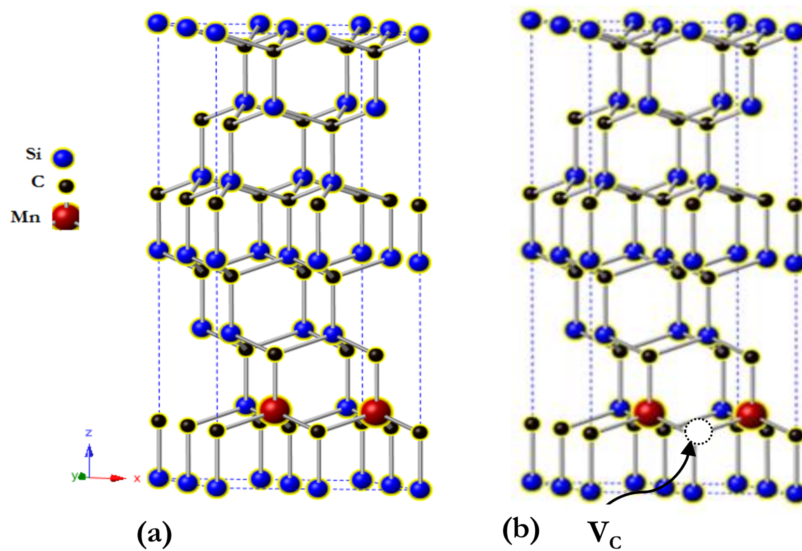


*Figure.3.36. The Supercell used in the calculation of Mn-Mn magnetic ordering, (a) without vacancy, (b) with C vacancy $V_C$.*

Two different cases of interstitial sites were explored. In the first case one of the Mn atom or both of them displaced slightly from their original site towards neighboring C vacancy, we call it ($Mn_d$). While in the second case the Mn atoms are placed in interstitial region where it can be surrounded by (four C/Si atoms), we call it ($Mn_I$). We then calculate the total energy of supercells with Mn spins ordered ferromagnetically (FM) and antiferromagnetically (AFM). Energies and magnetic moments for different configurations are summarized in table (3.5). The first column in the table describes the

configuration of the two Mn atoms, we start with two Mn atoms at two neighboring Si sites ($Mn_{Si}$-$Mn_{Si}$) with common C vacancy and then we displaced slightly one of Mn atoms towards interstitial site ($Mn_d$-$Mn_{Si}$). In addition, we displaced both Mn atoms from their sites slightly towards interstitial positions; these configurations are represented as ($Mn_d$-$Mn_d$). All indicated configurations were studied for both ferromagnetic and antiferromagnetic coupling as indicated by arrows. In the case of Mn at interstitial site, two different cases were studied; Mn at interstitial sites ($Mn_I$) surrounded with four C atoms coupled with next nearest neighbor Mn at Si site ($Mn_I$-$Mn_{Sinext}$) and $Mn_I$ surrounded with four C atoms coupled with nearest Mn at Si site ($Mn_I$-$Mn_{Sin}$). For all configurations, the energy was calculated relatively to the ferromagnetic coupling energy. The arrows indicate the parallel (FM) and antiparallel (AFM) coupling.

***Table 3.5.*** *(a) Relative energy to the FM configuration and average magnetic moment per Mn atom for different coupled pair configurations with neighboring C vacancy and (b) Energy and average magnetic moment per Mn atom for coupled Mn atoms at substitutional and interstitial sites.*

| Configuration | Energy (eV) | M ($\mu_B$) |
|---|---|---|
| (a) Mn at substitutional and displaced sites | | |
| $\uparrow Mn_{Si}$-$\uparrow Mn_{Si}$ | 0 | 3.03 |
| $\uparrow Mn_d$-$\uparrow Mn_{Si}$ | -0.56 | 2.78 |
| $\uparrow Mn_d$-$\uparrow Mn_d$ | +4.13 | 2.25 |
| $\uparrow Mn_{Si}$-$\downarrow Mn_{Si}$ | -0.12 | -0.02 |
| $\uparrow Mn_d$-$\downarrow Mn_{Si}$ | -0.60 | -0.68 |
| $\uparrow Mn_d$-$\downarrow Mn_d$ | +4.13 | 0.00 |
| (b) Mn and interstitials sites | | |
| $\uparrow Mn_I$ -$\uparrow Mn_{Sinextnn}$ | 0 | 0.27 |
| $\uparrow Mn_I$-$\downarrow Mn_{Sinextnn}$ | -0.002 | 0 |
| $\uparrow Mn_I$ -$\uparrow Mn_{Sinn}$ | 0 | 2.28 |
| $\uparrow Mn_I$-$\downarrow Mn_{Sinn}$ | -0.88 | 0 |

It is clear that the AFM coupled cases are more stable than the FM cases for Mn at substitutional sites. The table 3.5 also shows that the magnetic stability improves when one of the Mn atoms is displaced toward interstitial positions. However, the configuration with two displaced Mn atoms is far less stable. The average magnetic moment per Mn atom is reduced when one or both atoms are displaced from substitutional sites toward interstitial positions. This result is in agreement with the previous work done by Bernardini et al [114] who studied the energy stability and magnetic properties of Mn dimmers in silicon.

For the interstitial positions, in the case of $Mn_I$ coupled with Mn at next neighbor Si substitutional site, the FM configuration is not stable because it change sign and becomes antiferromagnetic. Also, Mn at interstitial site coupled with Mn atom at nearest neighbor Si site is found to be less stable in the case ferromagnetic coupling compared with antiferromagnetic coupling. In addition, two Mn atoms at interstitial positions were found to be nonmagnetic. From the latter results, one can argue that that Mn at interstitial sites is electrically non-active considering that magnetism is carriers-mediated mechanism.

These results explain the decrease in the magnetic moment by decreasing the ratio of Mn atoms at substitutional sites. As fluence increases, more Mn atoms go to interstitial position and the coupling between them or with Mn atoms at Si sites decreases the average magnetic moments of the system.

To correlate between our calculation and experimental results, we propose that for the lowest fluence ($5\times10^{15}cm^{-2}$), the magnetism observed is attributed to the Mn atoms at C substitutional sites (about 41% of Mn atoms occupy substitutional sites as confirmed from RBS measurements). As the fluence increases, more Mn atoms occupy Si

substitutional positions (about 63% of Mn atoms occupy substitutional sites), thereby causing a rise in the moment per Mn.

Further increase of fluence, decreases the ratio of the Mn atoms that occupy substitutional site and most Mn atoms occupy interstitial site. Hence, for the highest fluence ($5\times10^{16}cm^{-2}$) the observed substantial reduction in magnetism can be attributed to a large fraction of Mn atoms at interstitial sites and also to the AFM coupling between Mn at interstitial sites and substitutional site.

### 3.4.4 Magnetic coupling strength

The energy difference $\Delta E$ between FM and AFM configurations reveals the strength of the exchange coupling between Mn atoms. When the energy difference is positive, the ground state of the DMS is AFM.

Two Mn atoms at two Si substitutional sites were studied with different separation. For each Mn-Mn separation, ferromagnetic (FM) and antiferromagnetic (AFM) alignments of Mn spins were considered. The total energy difference $\Delta E$ between these two alignments is a measure of the coupling strength. Table 3.6 summarizes the results obtained for the coupling strength versus distance for $Mn_{Si}$-$Mn_{Si}$ with different separation. In addition to the 2×2×1 supercell used for calculation, a larger supercell containing 98 atoms was used also to study the effect of the distance on the magnetic ordering and strength of two Mn atoms at Si substitutional site with neighboring C vacancy.

As we can see from the table, in the nearest neighbor arrangement ($Mn_{Si}$-$Mn_{Si}$), the antiferromagnetic order of Mn atoms are very stable with the absolute value of energy difference of about 120 meV. Our values of the Mn coupling energy for the nearest-

neighbor (120 meV) are larger than those reported by Miao et al [26] and Andrei Los et al [109] for 3C-SiC (20 meV and 96 meV respectively).

***Table3.6.*** *Magnetic moments and energy differences between FM and AFM coupled configurations as a function of Mn-Mn distances. The energies shown are values relative to the FM energy.*

| Configuration | d (a.u) | Energy (eV) | M ($\mu_B$) | ΔE (FM-AFM) (eV) |
|---|---|---|---|---|
| **SiC 2x2x1** | | | | |
| $\uparrow Mn_{Si}$-$\uparrow Mn_{Si}$ | 5.82 | 0 | 3.03 | 0.125 (AFM) |
| $\uparrow Mn_{Si}$-$\downarrow Mn_{Si}$ | 5.82 | -0.123 | -0.02 | |
| $\uparrow Mn_{Si}$-$\uparrow Mn_{Si}$ | 9.67 | +0.994 | 2.60 | 0.068 (AFM) |
| $\uparrow Mn_{Si}$-$\downarrow Mn_{Si}$ | 9.67 | +0.926 | 0.16 | |
| **SiC 3x3x1** | | | | |
| $\uparrow Mn_{Si}$-$\uparrow Mn_{Si}$ | 5.82 | 0 | 3.31 | 0.252 (AFM) |
| $\uparrow Mn_{Si}$-$\downarrow Mn_{Si}$ | 5.82 | -0.252 | 0.003 | |
| $\uparrow Mn_{Si}$-$\uparrow Mn_{Si}$ | 11.66 | +1.062 | 3.12 | 0.096 (AFM) |
| $\uparrow Mn_{Si}$-$\downarrow Mn_{Si}$ | 11.66 | +0.964 | 0.53 | |

It is clear from table 3.6 that coupling strength reduces, although still being significant when Mn atoms are drawn further apart, while their magnetic moment alignment remains antiferromagnetic. At Mn-Mn distance of about ~10a.u, the magnetic coupling calculated in [26] changes the sign and becomes antiferromagnetic, while our calculations show almost no change compared to the nearest-neighbor case. These different in calculation may be attributed to the difference in structure of each polytype and the computational method used to produce the results. We expect that as the distance increases, the coupling changes sign and the FM becomes more stable. Further increase in distance will reduce the coupling and the system will become paramagnetic. The decrease of the coupling strength with increasing distance between Mn atoms can be used as a plausible scenario

to explain the reduction of magnetism after annealing. As was described in section (3.4.3) the atoms are spread in a larger region after annealing which decreases the coupling strength and hence decreases the magnetization.

Moreover, the reduction of magnetic coupling strength with increasing Mn-Mn separation may reflect the localized character of magnetism, rather than carriers-mediated one. This aspect is also corroborated by the fact of the presence of damaged zones (high defects concentration) that can alter any mechanism mediated by carriers.

### 3.4.5 Relaxation effect

It has been shown in several earlier studies that electronic and magnetic properties of DMSs are influenced significantly by lattice relaxation. In fact, the very existence of the TM magnetic moments in SiC, DMSs critically depends on the supercell geometry and on whether or not the supercell was allowed to reconstruct after the impurity substitution. In order to investigate the effect of the relaxation on the energy stability, magnetic moments and magnetic ordering, relaxation of the supercell aimed at minimizing intra-cell forces and optimizing the atomic positions is carried out. On the basis of atomic sizes, one may expect a stronger relaxation for the C than for the Si site substitution. The comparison between energy and magnetic moment of the supercell before and after relaxation are summarized in Table (3.7). As was expected, the energy after relaxation has been lowered for both configurations. However, we didn't notice a change in the magnetic moment of the FM coupling, whereas there is a small increase in magnetic moment after relaxation for AFM alignment.

***Table3.7.*** *Energy, total magnetic moments and magnetic moment per 3d-atom for FM and AFM configurations before and after relaxation. The energies shown are relative to the relaxed case of each configuration.*

| Configuration | | Energy (eV) | MMT ($\mu_B$) | MMI($\mu_B$) |
|---|---|---|---|---|
| $\uparrow Mn_{Si}$-$\uparrow Mn_{Si}$ | not relaxed | 0 | 6.06 | 2.36<br>2.36 |
| | relaxed | -0.64 | 6.00 | 2.49<br>2.50 |
| $\uparrow Mn_{Si}$-$\downarrow Mn_{Si}$ | not relaxed | 0 | 0.04 | 2.33<br>-2.31 |
| | relaxed | -0.53 | 0.57 | 2.68<br>-2.31 |

The energy difference ΔE (FM-AFM) after relaxation is 110 meV as compared to 120 meV which indicates that the coupling strength decreases slightly due to relaxation effect even though the AFM alignment remains the preferred coupling between Mn atoms. Energy wise, we found that the Mn atoms are slightly displaced from the regular crystalline positions towards the C vacancy. This result is in agreement with data of Miao et al. [26] who found that magnetic moment of Mn doped 3C-SiC decreases after relaxation and have attributed this reduction to a stronger hybridization with the Si dangling bonds due to relaxation.

### 3.4.6 GGA+U results

We have performed GGA+U calculations to investigate the effect of electron correlations and compare it with the GGA calculations. U has been varied from 2.0 eV to 3.0 eV treating as a parameter. The magnetic moment and energy stability of each configuration are listed in Table 3.8. Mn at Si/C sites with nearest C vacancy has been

studied. The energy is taken with respect to the GGA calculation for the same configuration. It is clear that energy increases for both configurations when we use GGA+U approximation and it increases also with increasing U. The local magnetic moment is bigger in the case of GGA+U than that of GGA approximation.

***Table. 3.8.*** *Energy relative to the GGA calculation and average magnetic moment per Mn atom for different configurations with neighboring C vacancy.*

| | **Mn at Si site** | | | **Mn at C site** | | |
|---|---|---|---|---|---|---|
| **U (eV)** | **Energy (eV)** | **$M_{tot}$** | **$M_I$** | **Energy (eV)** | **$M_{tot}$** | **$M_I$** |
| 2.0 | 0.18 | 4.22 | 3.12 | 1.77 | 2.99 | 1.99 |
| 2.5 | 2.03 | 4.25 | 3.14 | 2.76 | 2.99 | 2.01 |
| 2.7 | 2.22 | 4.28 | 3.18 | 3.03 | 2.99 | 2.05 |
| 3.0 | 2.41 | 4.31 | 3.22 | 3.29 | 2.99 | 2.09 |

Figure 3.37 shows the DOSs obtained from GGA+U calculations for Mn at Si site and Mn at C site respectively. In the case of Si substitution, increasing U results in a small shift of spin down towards the conduction band resulting in electron transfer to the majority levels and hence increasing the magnetic moment.

In case of C substitution, there was no noticeable difference between DOS's in case of GGA and GGA+U calculations. As we increase U, no change can be observed in DOS's. So, in this case, magnetic moments didn't change. So, we can conclude that using GGA approximation yields reasonable results without including the repulsion on site interaction U.

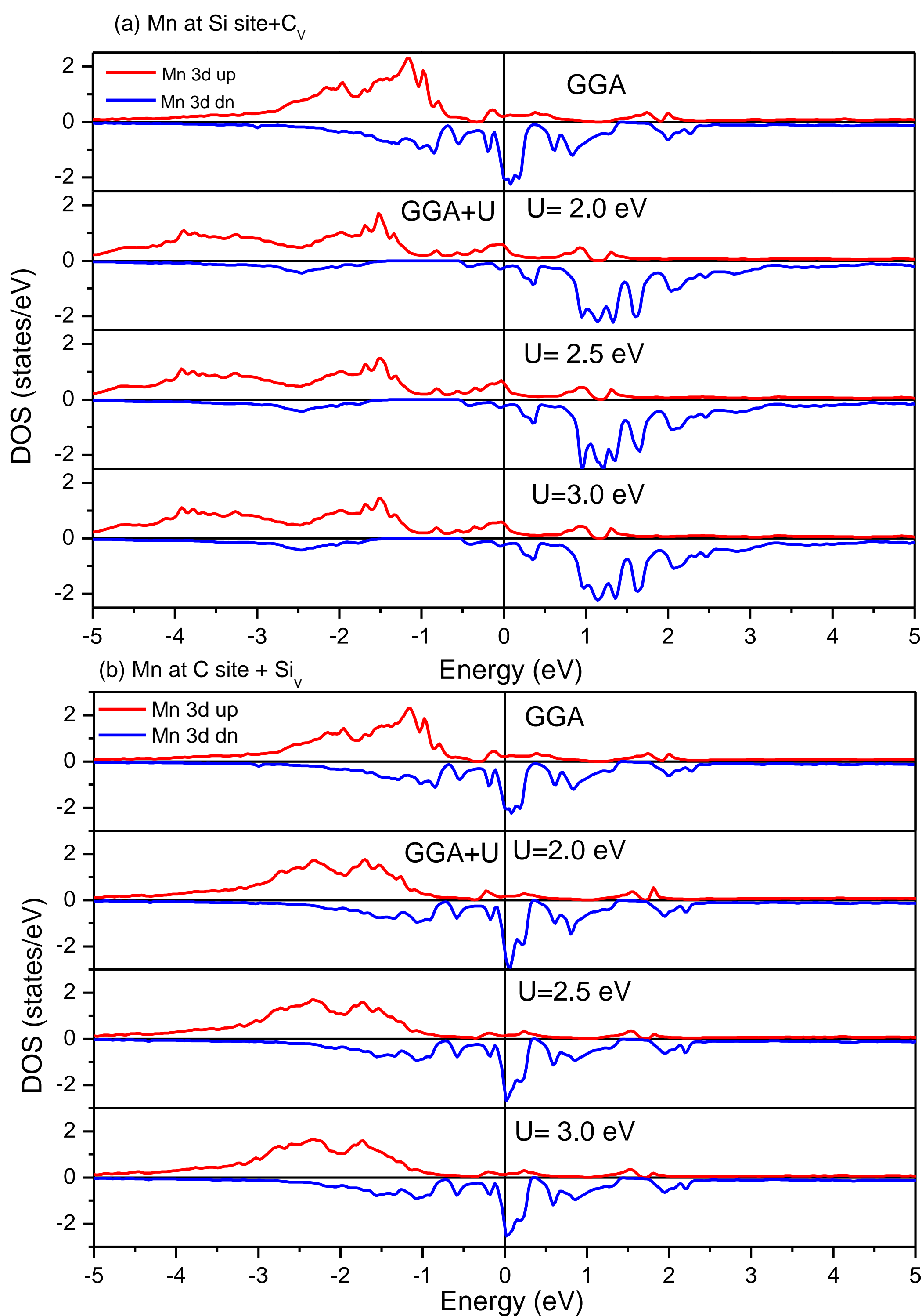


*Figure. 3.37. Mn d states from the GGA and GGA+U calculations for different values of U for (a) Mn at Si site with nearest C vacancy and (b) Mn at C site with nearest Si vacancy.*

# Chapter 4. Conclusion

In this work, we have investigated two important ion implantation related issues in Mn implanted 6H-SiC: implantation-induced lattice damage and the effect of structural disorder on the magnetic properties of the implanted samples.

Ion implantation is known to create a huge amount of defects. The accumulation and the recovery of this damage upon annealing as a function of Mn fluence has been characterized structurally using Rutherford Backscattering and Channeling Spectroscopy (RBS/C), High Resolution X-Ray Diffraction technique (HRXRD) and micro Raman Spectroscopy (µRS). A set of 6H-SiC samples were implanted with Mn atoms using four different fluencies of $1\times10^{12}$, $5\times10^{15}$, $1\times10^{16}$ and $5\times10^{16}$ Mn/cm$^2$. The implantation was carried out using Mn ions of energy 80 keV at 365°C (to allow for crystallization). RBS/C measurements indicate that Mn-implantation introduces various types of disorder in the 6H-SiC lattice. This disorder is distributed in depth through the crystal into two main regions, one closer to the surface and another coinciding with the implanted ion projected range. The degree of damage was measured by the accumulated damage parameter $f_D$ ($f_D$ is a parameter that varies from 0 for perfect crystal to 1 for amorphous phase). The accumulated damage increases with increasing fluence (0.2 for $5x10^{15}$, 0.7 for $1x10^{16}$ and 0.9 for $5x10^{16}$ Mn/cm$^2$). $F_D$ was very small for the lowest fluence ($1x10^{12}$ Mn/cm$^2$) which is mainly attributed to surface defects, but substantially increases as the fluence increases from $5x10^{15}$ Mn/cm$^2$ reflecting by the increase in the vacancies and interstitials concentrations. The sample is almost amorphous for the highest fluence ($5\times10^{16}$ Mn/cm$^2$). The maximum accumulated damage is centered around 50 nm below the surface for the two lowest fluencies and are well correlated to Mn profile (since their

depth profiles are both centered at the same position of around 50 nm). For the highest fluence, another type of Mn related defects is expected (since the defects profile is centered at around 80 nm and Mn profile at 50 nm).

SRIM simulation confirmed that the damage build-up is dominated by simple point defects such as Mn, Si and C interstitials and vacancies. The fraction $f_s$ of Mn atoms that occupy substitutional sites was found to increase from 41% to 63% with increasing fluence from $5\times10^{15}$ Mn/cm$^2$ to $1\times10^{16}$ Mn/cm$^2$ respectively. But it vanishes in the higher fluencies which mean a sizable fraction of that Mn atoms, in this case, are in interstitial sites. For the lowest fluence, we expect more Mn atoms to occupy C substitutional site because the number of C vacancies is greater than Si vacancies. As we increase the fluence to $1\times10^{16}$ Mn/cm$^2$, Mn occupying Si sites increases. The drastic decrease of the fraction of Mn atoms occupying a regular substitutional site for the fluence $5\times10^{16}$ cm$^{-2}$ is attributed to the degradation of the crystal lattice caused by a substantial enhancement of defects concentration.

HRXRD measurements analysis confirmed that the damage produces strain which increases with increasing fluence, from 2% for $5\times10^{15}$ to 4% for $1\times10^{16}$ and reaching a value of 5% for $5\times10^{16}$ Mn/cm$^2$.

The magnetic characterization of the implanted samples showed a ferromagnetic-like behavior. The saturation magnetization corresponds to a magnetic moment per Mn atom of about 0.7$\mu_B$ for the lowest fluence (5x10$^{15}$ Mn/cm$^2$). It increases to 1.7 $\mu_B$ for the intermediate fluence (1x10$^{16}$ Mn/cm$^2$) and then decreases to 0.19 $\mu_B$ for the highest fluence (5x10$^{16}$ Mn/cm$^2$). This magnetic behavior was explained by correlating the magnetism with the structural behavior. For the lowest fluence, most Mn atoms go into C

substitutional positions, giving a rise to a small magnetic moment per Mn atoms. As the fluence increases, more Mn atoms occupy Si substitutional sites and the magnetic moment per Mn atom increases. Further increase in the fluence leads to amorphasization of the implanted region due to increase of the accumulated damage. At this fluence, a large fraction of the Mn atoms occupy the interstitial positions which suppress the value of the magnetic moment. This scenario is affirmed by the *ab-initio* calculations. The results of our calculations indicated that when Mn atom substitute a Si atom, it gives higher magnetic moment compared to the case when Mn substitutes a C atom and this explain the magnetic behavior of the lowest and intermediate fluencies. The different behavior of Mn at Si and C sites was attributed to the different coupling between C/Si dangling bonds and the 3d Mn. The other important result obtained was the increase of the magnetic moment when there is a neighboring C/Si vacancy of Mn at Si site and Mn at C site respectively. However, the results showed that the configuration of Mn at the Si site with a neighbouring C vacancy is far more stable than the configuration of Mn at the C site with Si vacancy. The calculation also showed that Mn at interstitial sites with C neighbors are more favorable than those with Si neighbors and the magnetic moment in this case is less compared to the substitutional sites. This explains the decrease of the magnetic moment by increasing the interstitial defects. For the highest fluence, the decrease of the magnetic moment can be attributed to a large fraction of Mn atoms at interstitial sites and also to the AFM coupling between Mn atoms at interstitial sites and substitutional sites.

We have also found that the Fermi level of Mn doped 6H-SiC lies in the band gap in the impurity states produced by Mn atoms. This may make the understanding of the magnetism of Mn doped 6H-SiC in accord with the impurity band model.

The study of the crystalline structure recovery of the implantation-induced damage showed a very limited recovery after annealing at 800 $^{o}$C indicating that the damage is stable to at least up to that temperature. Almost all defects have been annealed out after thermal treatment of 1100$^{o}$C with a disappearance of Mn signals from RBS spectrum. However, the EPMA- EDX measurements confirmed that Mn is still in the 1100 °C annealed SiC. We expect Mn to diffuse leading to a strong Mn dilution to a value below the detection limit of RBS. The existence of ferromagnetic like behavior in SQUID measurements is a good evidence that Mn atoms still exist within the sample after annealing. Even though the magnetization values were reduced strongly, the magnetization maintains its fluence dependence as before annealing and the intermediate fluence still exhibits higher magnetization compared with the other two fluences. The observed reduction in magnetization on the annealed sample after 1100 $^{0}$C and 1600 $^{0}$C can be due to the annealing of vacancies neighboring Mn at substitutional site. This leads to a decrease in the magnetic moment as was supported by our *ab- initio* calculations. The other possible reason for the magnetization reduction after annealing is the increase of interatomic distances between the Mn atoms due to the diffusion, which reduces the ferromagnetic coupling and hence decreases the magnetization.

In summary, we have presented an elaborated overview of the structural and magnetic properties of Mn implanted 6H-SiC. This overview provides some new and fundamentally interesting informations, which will be useful for different types of studies

on ion implanted 6H-SiC. Although we have presented many experimental and theoretical results about the implantation induced damage in this thesis, there are still many open problems that require further investigations. With respect to the electrical characterization of the lattice damage, the interesting topic is to study the effect of these structural defects on the transport properties of 6H-SiC as a function of Mn fluence using Hall Effect measurements. For the magnetic characterization, it is important to identify the Curie temperature which is estimated to be higher than 250K in this study.

In this thesis, the study of the recovery of the implantation-induced damage showed very limited recovery after annealing at 800 $^{o}$C while almost all defects have been removed after annealing at 1100 $^{o}$C with disappearance of Mn signals. So, it is interesting to study the effect of subsequent thermal annealing treatment between 800 $^{o}$C and 1100$^{o}$C on the structural and magnetic properties of the annealed samples. Such study will help identifying the appropriate annealing temperature at which substantial damage recovery and magnetization enhancement will occur at the same time. In particular, one can monitor the annealing out of various types of defects: Mn impurity, Si and C vacancy, host atoms and Mn interstitials, besides the complex defects that can be formed.

In our *ab-intio* calculation results, we found that the antiferromagnetic coupled Mn atoms at substitutional sites are more stable than those feromagnetically coupled. In our calculations, we used two supercelles containing 48 atoms and 98 atoms respectively to study the effect of the distance on the magnetic ordering and strength of two Mn atoms at Si substitutional site with neighboring C vacancy. Larger superells are needed to study the effect of distance between Mn atoms and the coupling strength. The nature of this

exchange coupling can provide important information about the nature of magnetism in Mn doped SiC.

# Publications

## Published Papers

**1- M. Al Azri, M. Elzain, K. Bouziane, S. M. Chérif, Y. Roussigné, A. Declémy, M. Drouet, and L. Thome´ ,** Magnetic properties of Mn implanted 6H-SiC single crystal, J. App. Phy. **111**, 07C315 (2012). [The article was selected for the March 2012 issue of Virtual Journal of Quantum Information].

2- **M. Al Azri, M. Elzain, K. Bouziane, S. M. Chérif, A. Declémy and L. Thomé,** Model for Mn in 6H-SiC from first-principle studies, J. App. Phy. **113**, 17C305 (2013).

## Accepted for Publication

- **M. Al Azri, M. Elzain, K. Bouziane, S. M. Chérif, A. Declémy and L. Thomé,** First principle calculation of the electronic and magnetic properties of Mn-doped 6H-SiC, EPJ Web of Conferences.

## Conference Presentations

1. **M. Al Azri, M. Elzain, K. Bouziane, S. M. Chérif, Y. Roussigné, A. Declémy, M. Drouet, and L. Thome´ ,** Magnetic properties of Mn implanted 6H-SiC single crystal, 56th Annual conference on magnetism and magnetic materials (MMM) , **(30 October – 3 November 2011)**, Arizona, USA.

2. **M. Al Azri, M. Elzain, K. Bouziane, S. M. Chérif, A. Declémy and L. Thomé,** Model for Mn in 6H-SiC from first-principle studies, 12th Joint MMM/Intermag Conference, **(January 14th to 18th, 2013)**, Chicago, Illinois, USA.

3. **M. Al Azri, M. Elzain, K. Bouziane, S. M. Chérif, Y. Roussigné, A. Declémy, M. Drouet, and L. Thomé ,** Structural and Magnetic Properties of Mn implanted 6H-SiC, Nano Science conference, ( 2010) Paris 13 university, France.

4. **K. Bouziane , M. Al Azri, M. Elzain, S. M. Chérif, Y. Roussigné, A. Declémy, M. Drouet, and L. Thomé,** Electronic and Magnetic Properties of Mn-doped 6H-SiC Experiment and first principal calculation, The International Conference on Advanced Materials for Photonics, Sensing and Energy Conversion Applications (AMPSECA 2012), (**December 5-7, 2012**), El Jadida, Morocco.

## References:


1. H. Ohno, Science **281** (5379), 951-956 (1998).
2. M. C. Wang, R. P.; Rushforth, A. W.; Edmonds, K. W.; Foxon, C. T.; Gallagher, B. L., Applied Physics Letters **93** (13) (2008).
3. T. Jungwirth, K. Y. Wang, J. Mašek, K. W. Edmonds, J. König, J. Sinova, M. Polini, N. A. Goncharuk, A. H. MacDonald, M. Sawicki, A. W. Rushforth, R. P. Campion, L. X. Zhao, C. T. Foxon and B. L. Gallagher, Physical Review B **72** (16), 165204 (2005).
4. T. Dietl, H. Ohno, F. Matsukura, J. Cibert and D. Ferrand, Science **287** (5455), 1019-1022 (2000).
5. T. Dietl, H. Ohno and F. Matsukura, Physical Review B **63** (19), 195205 (2001).
6. S. J. Pearton, C. R. Abernathy, M. E. Overberg, G. T. Thaler, D. P. Norton, N. Theodoropoulou, A. F. Hebard, Y. D. Park, F. Ren, J. Kim and L. A. Boatner, Journal of Applied Physics **93** (1), 1-13 (2003).
7. M. Canino, Univ. Di Bologna, 2007.
8. P. Krishna and D. Pandey, *Close Packed Structures*. (International Union of Crystallography, 1981).
9. H. Baumhauer, Z. Kristallogr **50**, 33-39 (1912).
10. A. R. Verma and P. Krishna, *Polymorphism and polytypism in crystals*. (Wiley, 1966).
11. G. L. Harris and INSPEC, *Properties of Silicon Carbide*. (INSPEC, Institution of Electrical Engineers, 1995).
12. O. Kordina, Linköping University, 1994.
13. G. Pensl, H. Morkoc, B. Monemar and E. Janzen in *Silicon Carbide, III-Nitrides, and Related Materials* (Trans Tech Publications, Switzerland, 1998), pp. 264-268.
14. S. M. Sze and K. K. Ng, *Physics of Semiconductor Devices*. (Wiley, 2006).
15. W. J. Choyke and G. Pensl, MRS Bull. **22** (3), 25-29 (1997).
16. V. S. M. Syväjärvi, M. Izadifard, W. M. Chen, I. A. Buyanova, P. Svedlindh, and R. Yakimova, Mater. Sci. Forum 457-460 **747** (2004).

17. N. Theodoropoulou, A. F. Hebard, S. N. G. Chu, M. E. Overberg, C. R. Abernathy, S. J. Pearton, R. G. Wilson and J. M. Zavada, Electrochemical and Solid-State Letters **4** (12), G119-G121 (2001).
18. N. Theodoropoulou, A. F. Hebard, S. N. G. Chu, M. E. Overberg, C. R. Abernathy, S. J. Pearton, R. G. Wilson, J. M. Zavada and Y. D. Park, Journal of Vacuum Science & Technology A: Vacuum, Surfaces, and Films **20** (3), 579-582 (2002).
19. F. Stromberg, W. Keune, X. Chen, S. Bedanta, H. Reuther and A. Mücklich, Journal of Physics: Condensed Matter **18** (43), 9881 (2006).
20. S. Lin, Z. Chen, P. Liang, D. Jiang and H. Xie, Chemical Physics Letters **496** (1–3), 56-58 (2010).
21. C. Dupeyrat, A. Declémy, M. Drouet, D. Eyidi, L. Thomé, A. Debelle, M. Viret and F. Ott, Physica B: Condensed Matter **404** (23-24), 4731-4734 (2009).
22. K. Bouziane, M. Mamor, M. Elzain, P. Djemia and S. M. Chérif, Physical Review B **78** (19), 195305 (2008).
23. W. Wang, F. Takano, H. Ofuchi and H. Akinaga, New Journal of Physics **10** (5), 055006 (2008).
24. B. Song, H. Bao, H. Li, M. Lei, J. Jikang, J. Han, X. Zhang, M. Songhe, W. Wang and X. Chen, Applied Physics Letters **94** (10), 102508-102508-102503 (2009).
25. S. B. Ma, Y. P. Sun, B. C. Zhao, P. Tong, X. B. Zhu and W. H. Song, Physica B: Condensed Matter **394** (1), 122-126 (2007).
26. M. S. Miao and W. R. L. Lambrecht, Physical Review B **68** (12), 125204 (2003).
27. H. K. Y. Kim, B. Yu, D. Choi and Y. Chung, Key Engineering Materials **264 - 268**, 1237-1240 (2004).
28. V. L. Shaposhnikov and N. A. Sobolev, Journal of Physics: Condensed Matter **16** (10), 1761 (2004).
29. A. V. Los, A. N. Timoshevskii, V. F. Los and S. A. Kalkuta, Physical Review B **76** (16), 165204 (2007).
30. C. M. Zetterling and I. o. E. Engineers, *Process Technology for Silicon Carbide Devices*. (INSPEC, The Institution of Electrical Engineers, 2002).

31. K. O. Barbosa, W. V. M. Machado and L. V. C. Assali, Physica B: Condensed Matter **308–310** (0), 726-729 (2001).
32. J. Zhou, H. Li, L. Zhang, J. Cheng, H. Zhao, W. Chu, J. Yang, Y. Luo and Z. Wu, The Journal of Physical Chemistry C **115** (1), 253-256 (2010).
33. J. Z. M. Rawski, M. Kulik, A. Drozdziela, L. Lin, S. Prucnal, K. Pyszniak and M. Turek, ACTA PHYSICA POLONICA A **120** (2011).
34. J. García López, Y. Morilla, J. C. Cheang-Wong, G. Battistig, Z. Zolnai and J. L. Cantin, Nuclear Instruments and Methods in Physics Research Section B: Beam Interactions with Materials and Atoms **267** (7), 1097-1100 (2009).
35. E. Morvan, N. Mestres, J. Pascual, D. Flores, M. Vellvehi and J. Rebollo, Materials Science and Engineering: B **61–62** (0), 373-377 (1999).
36. G. Battistig, N. Q. Khánh, P. Petrik, T. Lohner, L. Dobos, B. Ṕcz, J. García López and Y. Morilla, Journal of Applied Physics **100** (9) (2006).
37. F. Takano, W. Wang, H. Ofuchi, T. Ohshima and H. Akinaga, AIP Conference Proceedings **1199** (1), 443-444 (2010).
38. P. Miranda, U. Wahl, N. Catarino, K. Lorenz, J. G. Correia and E. Alves, Nuclear Instruments and Methods in Physics Research Section B: Beam Interactions with Materials and Atoms **286** (0), 89-92 (2012).
39. Z. C. Feng, S. C. Lien, J. H. Zhao, X. W. Sun and W. Lu, Thin Solid Films **516** (16), 5217-5222 (2008).
40. A. V. Komarov, A. V. Los, S. M. Ryabchenko and S. M. Romanenko, Journal of Applied Physics **109** (8), 083936-083937 (2011).
41. J. Romanek, D. Grambole, F. Herrmann, M. Voelskow, M. Posselt, W. Skorupa and J. Żuk, Nuclear Instruments and Methods in Physics Research Section B: Beam Interactions with Materials and Atoms **251** (1), 148-156 (2006).
42. K. Abe, O. Eryu, O. Kogi and K. Nakashima, Nuclear Instruments and Methods in Physics Research Section B: Beam Interactions with Materials and Atoms **206** (0), 960-964 (2003).
43. L. Ottaviani, M. Lazar, M. L. Locatelli, J. P. Chante, V. Heera, W. Skorupa, M. Voelskow and P. Torchio, Materials Science and Engineering: B **91–92** (0), 325-328 (2002).

44. L. Calcagno, M. G. Grimaldi and P. Musumeci, Journal of Materials Research **12** (7), 1727-1733 (1997).
45. M. V. Rao, D. Nordstrom, J. A. Gardner, A. Edwards, E. G. Roth, G. Kelner and M. Ridgway, Nuclear Instruments and Methods in Physics Research, Section B: Beam Interactions with Materials and Atoms **127-128**, 655-659 (1997).
46. C. Zener, Physical Review **82** (3), 403-405 (1951).
47. T. Dietl and H. Ohno, Materials Today **9** (11), 18-26 (2006).
48. M. Dobrowolska, K. Tivakornsasithorn, X. Liu, J. K. Furdyna, M. Berciu, K. M. Yu and W. Walukiewicz, Nat Mater **11** (5), 444-449 (2012).
49. P. Mahadevan and A. Zunger, Applied Physics Letters **85** (14), 2860-2862 (2004).
50. M. Herbich, A. Twardowski, D. Scalbert and A. Petrou, Physical Review B **58** (11), 7024-7034 (1998).
51. M. v. Schilfgaarde and O. N. Mryasov, Physical Review B **63** (23), 233205 (2001).
52. T. Matsuoka, H. Okamoto, M. Nakao, H. Harima and E. Kurimoto, Applied Physics Letters **81** (7), 1246-1248 (2002).
53. R. C. Jaeger, *Introduction to Microelectronic Fabrication*, Second Edition ed. (Prentice-Hall, Inc, 2002).
54. S. O. Kasap, *Principles of electronic materials and devices*. (McGraw-Hill, 2006).
55. M. Nastasi and J. W. Mayer, *Ion Implantation and Synthesis of Materials*. (Springer-Verlag Berlin and Heidelberg GmbH & Company KG, 2006).
56. J. Ziegler and J. Biersack, in *Treatise on Heavy-Ion Science*, edited by D. A. Bromley (Springer US, 1985), pp. 93-129.
57. J. F. Ziegler, *Handbook of Ion Implantation Technology*. (North-Holland, 1992).
58. H. Geiger and E. Marsden, Proceedings of the Royal Society of London. Series A **82** (557), 495-500 (1909).
59. E. Rutherford, Philosophical Magazine Series 6 **21** (125), 669-688 (1911).
60. J. E. Westmoreland, J. W. Mayer, F. H. Eisen and B. Welch, Radiation Effects **6** (2), 161-174 (1970).
61. L. C. Feldman and J. W. Mayer, *Fundamentals of Surface and Thin Film Analysis*. (P T R Prentice Hall, 1986).

62. J. Lindhard, Mat. Fys. Medd. Dan. Vid. Selsk **34** (14) (1965).

63. J. W. Mayer and E. Rimini, *Ion Beam Handbook for Material Analysis*. (Elsevier Science, 1977).

64. K. W. Edmonds, K. Y. Wang, R. P. Campion, A. C. Neumann, N. R. S. Farley, B. L. Gallagher and C. T. Foxon, Applied Physics Letters **81** (26), 4991-4993 (2002).

65. B. scientific, (1998).

66. J. Blomgren, (1998).

67. G. H. Kassier, University of Pertoria, 2006.

68. P. Blaha, K. Schwarz, G. K. H. Madsen, D. Kvasnicka and J. Luitz, *WIEN2K, An Augmented Plane Wave Plus Local Orbitals Program for Calculating Crystal Properties* (Karlheinz Schwarz,Technical Universitat Wien, Austria, 2001).

69. S. Cottenier, *Density Functional Theory and the Family of (L)APW-methods: a step-by-step introduction*. (Instituut voor Kern- en Stralingsfysica (IKS), Katholieke Universiteit Leuven, Belgium, 2004).

70. P. Hohenberg and W. Kohn, Physical Review **136** (3B), B864-B871 (1964).

71. W. Kohn and L. Sham, Phys. Chem. Rev. A **140**, 1133 (1965).

72. J. P. Perdew, K. Burke and M. Ernzerhof, Physical Review Letters **77** (18), 3865-3868 (1996).

73. V. I. Anisimov, J. Zaanen and O. K. Andersen, Physical Review B **44** (3), 943-954 (1991).

74. A. I. Liechtenstein, V. I. Anisimov and J. Zaanen, Physical Review B **52** (8), R5467-R5470 (1995).

75. M. T. Czyżyk and G. A. Sawatzky, Physical Review B **49** (20), 14211-14228 (1994).

76. J. S. Griffith, *The Theory of Transition-Metal Ions*. (Cambridge University Press, 1961).

77. L. Hedin, Physical Review **139** (3A), A796-A823 (1965).

78. B. Pipeleers, Katholieke Universiteit Leuven, 2005.

79. K. Schmid, Radiation Effects **17** (3-4), 201-207 (1973).

80. L. A. Christel and J. F. Gibbons, Journal of Applied Physics **52** (8), 5050-5055 (1981).
81. A. Declémy, E. Oliviero, M. F. Beaufort, J. F. Barbot, M. L. David, C. Blanchard, Y. Tessier and E. Ntsoenzok, Nuclear Instruments and Methods in Physics Research Section B: Beam Interactions with Materials and Atoms **186** (1–4), 318-323 (2002).
82. S. Leclerc, A. Declemy, M. F. Beaufort, C. Tromas and J. F. Barbot, Journal of Applied Physics **98** (11), 113506-113506 (2005).
83. G. Bai and M. A. Nicolet, Journal of Applied Physics **70** (2), 649-655 (1991).
84. L. Tewordt, Physical Review **109** (1), 61-68 (1958).
85. J. C. Burton, F. H. Long and I. T. Ferguson, Journal of Applied Physics **86** (4), 2073-2077 (1999).
86. S. Nakashima, K. Kisoda and J. P. Gauthier, Journal of Applied Physics **75** (10), 5354-5360 (1994).
87. S. Nakashima and H. Harima, physica status solidi (a) **162** (1), 39-64 (1997).
88. S. Nakashima, H. Katahama, Y. Nakakura and A. Mitsuishi, Physical Review B **33** (8), 5721-5729 (1986).
89. P. J. Colwell and M. V. Klein, Physical Review B **6** (2), 498-515 (1972).
90. R. Héliou, J. L. Brebner and S. Roorda, Semiconductor Science and Technology **16** (10), 836 (2001).
91. H. Harima, S.-i. Nakashima and T. Uemura, Journal of Applied Physics **78** (3), 1996-2005 (1995).
92. U. Gottlieb, A. Sulpice, B. Lambert-Andron and O. Laborde, Journal of Alloys and Compounds **361** (1-2), 13-18 (2003).
93. A. Sulpice, U. Gottlieb, M. Affronte and O. Laborde, Journal of Magnetism and Magnetic Materials **272–276, Part 1** (0), 519-520 (2004).
94. M. Lee, Y. Onose, Y. Tokura and N. P. Ong, Physical Review B **75** (17), 172403 (2007).
95. D. B. Migas, V. L. Shaposhnikov, A. B. Filonov, V. E. Borisenko and N. N. Dorozhkin, Physical Review B **77** (7), 075205 (2008).

96. H. G. Bohn, J. M. Williams, C. J. MacHargue and G. M. Begun, J. Mater. Res. **2** (1987).
97. E. Wendler, A. Heft and W. Wesch, Nuclear Instruments and Methods in Physics Research Section B: Beam Interactions with Materials and Atoms **141** (1–4), 105-117 (1998).
98. A. Kozanecki, C. Jeynes, B. J. Sealy and A. Nejim, Nuclear Instruments and Methods in Physics Research, Section B: Beam Interactions with Materials and Atoms **136-138**, 1272-1276 (1998).
99. J. M. Luo, Z. Q. Zhong, M. Gong, S. Fung and C. C. Ling, Journal of Applied Physics **105** (6), 063711-063714 (2009).
100. M. K. Linnarsson and A. Hallén, Nuclear Instruments and Methods in Physics Research Section B: Beam Interactions with Materials and Atoms **273** (0), 127-130 (2012).
101. Y. An, S. Wang, D. Feng, Y. Huang, Z. Qin, X. Li, Z. Wu and J. Liu, Journal of Physics D: Applied Physics **46** (10), 105004 (2013).
102. T. T. Hlatshwayo, J. B. Malherbe, N. G. van der Berg, A. J. Botha and P. Chakraborty, Nuclear Instruments and Methods in Physics Research Section B: Beam Interactions with Materials and Atoms **273** (0), 61-64 (2012).
103. X. W. Zhou and C. H. Tang, Progress in Nuclear Energy **53** (2), 182-188 (2011).
104. V. Havránek, V. Hnatowicz, J. Kvítek and V. Peřina, Nuclear Instruments and Methods in Physics Research Section B: Beam Interactions with Materials and Atoms **72** (2), 224-226 (1992).
105. S. M. Bet, University of Central Florida , USA, 2003.
106. M. Gajdzik, C. Surgers, M. Kelemen, B. Hillebrands and H. VonLohneysen, Applied Physics Letters **68** (22), 3189-3190 (1996).
107. M. Gajdzik, C. Surgers, M. T. Kelemen and H. Von Lohneysen, Journal of Magnetism and Magnetic Materials **221** (3), 248-254 (2000).
108. Z. Jiang, X. Xu, H. Wu, F. Zhang and Z. Jin, Solid State Communications **123** (6–7), 263-266 (2002).
109. A. Los and V. Los, Journal of Physics: Condensed Matter **21** (20), 206004 (2009).

110. V. A. Gubanov, C. Boekema and C. Y. Fong, Applied Physics Letters **78** (2), 216-218 (2001).

111. Á. Gali, M. Bockstedte, N. T. Son and E. Janzén, MRS Online Proceedings Library **1069**, null-null (2008).

112. J. Ren-Xu, Z. Yu-Ming and Z. Yi-Men, Chin. Phys. B **19** (10), 107105-107105 (2010).

113. F. Bechstedt, A. Zywietz and J. Furthmüller, EPL (Europhysics Letters) **44** (3), 309 (1998).

114. F. Bernardini, S. Picozzi and A. Continenza, Applied Physics Letters **84** (13), 2289-2291 (2004).

## Appendix A

*Table A.1: List of recently reported annealing studies of SiC implanted with different elements.*

| substrate | Implanted ion | Growth T | Annealing T | comments | Ref |
|---|---|---|---|---|---|
| 4H-SiC | $Al^{+}$ | RT | 1100 °C in $N_2$ for 1 h | In a highly damaged SiC crystal, the short distance order is achieved during the post implantation annealing, but not the long distance order. | [36] |
| 3C-SiC | Mn | 800 °C | 1650 °C for 20 min | ————— | [37] |
| 6H-SiC | Fe | 550 °C | 1100 °C for 4min | Enhancement of ferromagnetic signals | [21] |
| 6H-SiC | Fe | 250 °C | 1000 °C - 1500 °C for 30 s | ————— | [38] |
| 4H-SiC | $Ni^{+}$ | 450 °C | 1100 °C, for 40 min | partial recovery of the crystal lattice quality was found for the less damaged samples | [34] |
| 6H–SiC | $C^{+}/Al^{+}$ | 600 °C | 1550 °C for 30 | -Elimination/suppression of the implantation induced amorphous layer.<br>- The activation of the implant acceptors are confirmed | [39] |
| 4H–SiC and 6H-SiC | Mn and Fe ions | 350 °C | 1650 C for 30 min | ferromagnetic ordering is not realized in both (Si,Mn)C and (Si,Fe) DMSs, at least at an effective concentration of corresponding ions of $10^{21}$ $cm^{3}$. | [40] |
| 6H-SiC | Al+ | - | 1650 °C for 10 min | ————— | [41] |
| 6H–SiC | $N^{+}$ | - | between 1600 and 1850 C for 20 s | Compared with the FA samples, the RTA samples had smoother surfaces. the RTA samples had better crystallinity than the FA samples. In the case of RTA for 20s, the samples needed to be annealed above 1750 C. | [42] |
| 6H–SiC | Al | RT | 1700 °C for 30 min | good recrystallization, no dopant loosing | [43] |
| 6H–SiC | N+ | RT | 200–1000 °C | - an almost total defect recovery occurred in partially damaged layers<br>- Amorphous layers were stable in the investigated temperature range | [44] |
| 6H–SiC | N, P, Al, B, V, Si, and C | Different temp | 1200 -1700°C. | ————— | [45] |

**Appendix B**

## Rutherford Backscattering and Channeling Spectrometry (RBS/C)

Rutherford backscattering spectrometry is a powerful non-destructive analytical technique employed in the characterization of materials, allowing to quantitatively assessing the elemental composition and structure of the analyzed material. Combining RBS with channeling, as explained in chapter 2, provides a measure of the crystalline quality and the location of impurities in the crystalline lattice.

RBS allows to obtain answers to the questions "Which elements are present in a material?", "How are they distributed through the material?" and "How much of each element is present?". Simply be measuring the energy of the detected backscattered ions, it is possible to identify the element at which the He ion was backscattered in the target, and the depth in the target at which the collision took place. Also, from the amount of backscattered ions with a particular energy it is possible to quantify the concentration of an element in the target material. Three physical concepts at the base of RBS allow answering the above questions, namely the kinematic factor K, the stopping cross section and the scattering cross section.

### B.1 Kinematic factor K

Since this technique is based on the detection of the backscattered alpha particles, the detector is placed at an angle greater than $90^0$ but less than $180^0$ with respect to an incoming particles (see Figure. B.1). The $^4He^+$ beam impinges on the target and a small fraction of the $^4He^+$ ions will be backscattered and collected in the detector where they create an electric signal proportional to their energy. The detector is coupled to an amplifier and a multichannel analyzer (MCA).

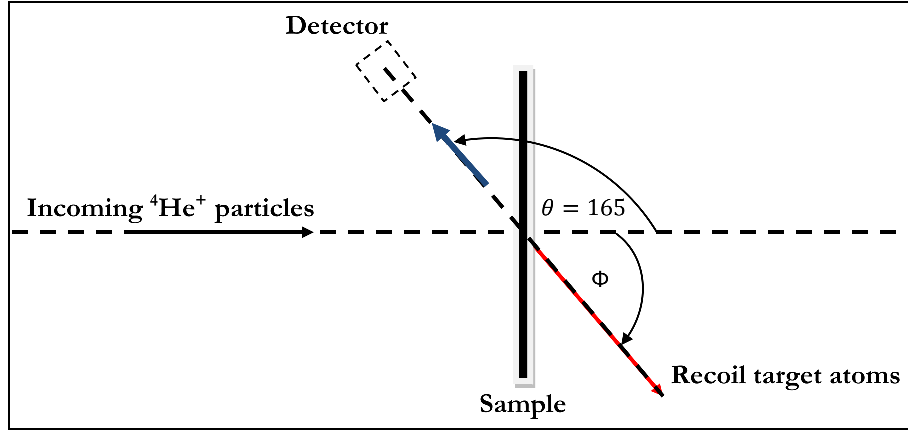


*Figure. B.1. A schematic diagram of RBS experiment.*

Depending on the energy of the backscattered He particle, the count will be placed in a certain channel by the MCA. In this way, all detected $^4He^+$ ions are contributing to a backscattering yield in function of the energy and a RBS spectrum is built up.

The energy $E_1$ of a backscattered projectile with incident energy $E_0$ and mass $M_1$ after scattering is given in the laboratory system by:

$$E_1 = KE_0 \qquad (B.1)$$

Where the kinematic factor K is given by:

$$K = \frac{E_1}{E_0} = \left[\frac{(M_2^2 - M_1^2 sin^2\theta)^{\frac{1}{2}} + M_1 cos\theta}{M_2 + M_1}\right]^2 \qquad (B.2)$$

Where $E_o$ is the energy of the incident ion with mass $M_1$, $E_1$ is the energy of the backscattered projectile, $M_2$ is the mass of the target atom and $\theta$ the scattering angle. Thus, the backscattered energy is equivalent to a mass scale.

During a backscattering experiment, the mass $M_1$ of the incident projectile, as well as the detection angle $\theta$, are fixed. As such, K is only dependent on, the target mass. By measuring $E_1$ at the detector, $M_2$ can be obtained from equation B.2 and the target mass identified.

The target material often consists of two (or more) types of atoms which differ in mass by a certain amount $\Delta M_2$. K is a monotonously increasing function with decreasing angle and increasing mass. So, to obtain the largest variation in K for the two masses, the scattering angle θ should be the largest possible, ideally θ= 180°. In practice, the detector is placed at 165°, as can be seen in Figure B.1.

## B.2. Stopping cross section

The projectile particles will not only scatter from the surface atoms, but they will also penetrate the sample and collide with target atoms at a depth *t* in the sample. In this case, the stopping of the ion due to electronic collisions has to be taken into account (Figure B.2).

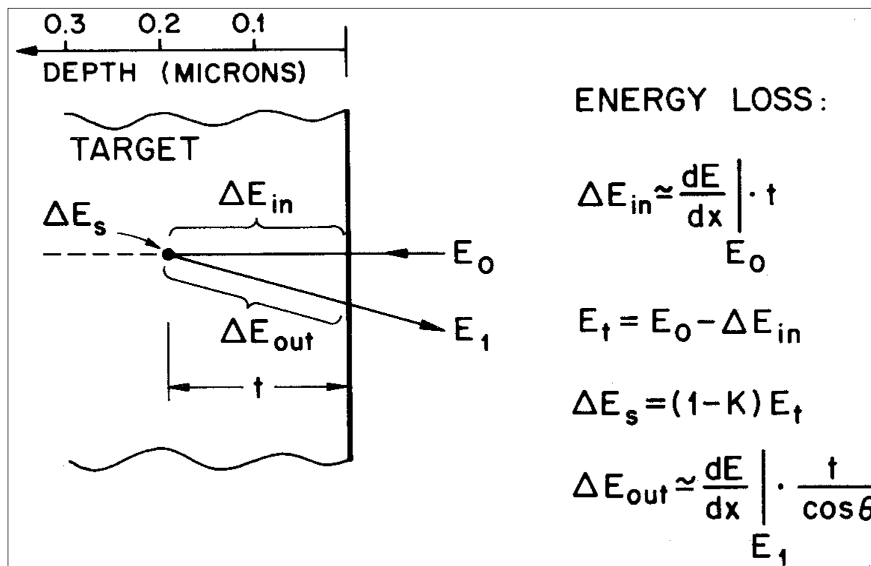


*Figure B.2. Components of energy loss for a projectile that scatters at a depth t. $\Delta E_{in}$ is the energy lost via electronic stopping along the incoming path, ΔEs is the energy lost due to scattering and $\Delta E_{out}$ is the energy lost by the outgoing ion caused by electronic stopping on the outgoing path. Then $E_1 = E_0 - \Delta E_{in} - \Delta E_s - \Delta E_{out}$.*

The energy loss occurs via three steps:

- Electronic energy loss during the inwards path due to inelastic scattering with electrons, the energy loss per length unit *dE/dx* is a function of the target material and the energy of the incoming He ions.
- Nuclear energy loss due to the scattering with a target atom. It is described by the kinematic factor K.
- Electronic energy loss along the outwards path.

Based on these three processes, the relation between the energy loss of a backscattered particle and the depth t can be calculated:

$$\Delta E = [S].t \qquad (B.3)$$

In this equation, ΔE is defined as the energy difference between a $^4He^+$ particle scattered from the surface and scattered at a depth t. [S] is called the energy loss factor and is given by:

$$[S] = \frac{K}{cos\theta_1}\frac{dE}{dx}|in + \frac{1}{cos\theta_2}\frac{dE}{dx}|out \qquad (B.4)$$

To increase the depth resolution of the RBS spectra, the length of the trajectory of the $^4He^+$ ions along the incoming or the outgoing path can be increased by respectively tilting the sample ($\theta_1$) so that the ions penetrate at a glancing angle or by positioning the detector ($\theta_2$) at a glancing angle.

## B.3. Scattering cross section

The scattering cross section $\sigma(\theta)$ is defined as the probability of an incident ion being scattered into a solid angle of the detector Ω at a scattering angle $\theta$. The number of particles incident in the detector, *Y,* is given by:

$$Y = \sigma(\theta).\Omega.Q.N_s \qquad (B.5)$$

Where $N_s$ is the total number of target atoms/cm$^2$ and $Q$ is the total number of incident particles in the beam. For RBS, the scattering cross section can be approximated by the Rutherford cross section for $M_1 < M_2$:

$$\sigma(\theta) = \left(\frac{Z_1 Z_2 e^2}{4E}\right)^2 \frac{1}{sin^4\left(\frac{\theta}{2}\right)} \qquad (B.6)$$

From this equation one concludes that $\sigma(\theta) \sim Z_2^2$ , being $Z_2$ the atomic number of the target atom. The scattering probability of an incoming He ion on a heavy ion is much higher than for a lighter atom. As such, on a RBS spectrum of an *LH* compound, where *L* is a light and *H* a heavy element, the signal from *H* will be much stronger than the one of *L*.

## Propriétés Structurales et Magnétiques du 6H-SiC Implanté-Mn

**Résumé:** Dans cette étude, des substrats 6H-SiC (0001) de type-n ont été implantés avec trois concentrations de $Mn^+$ : $5 \times 10^{15}$ Mn/cm$^2$ (teneur en Mn: 0,7%), $1 \times 10^{16}$ (~ 2%), et $5 \times 10^{16}$ cm$^{-2}$ (7 %) à une énergie d'implantation de 80 keV et pour une température de substrat de 365° C. Les échantillons ont été caractérisés par spectroscopie de rétrodiffusion de Rutherford, diffraction des rayons-X à haute résolution, spectroscopie micro-Raman et magnétométrie SQUID. L'objectif est d'étudier l'effet des défauts induits par l'implantation et de déduire une corrélation avec les propriétés magnétiques. Les résultats obtenus à partir des résultats de RBS/C montrent que 41% des Mn occupent les sites de substitution pour la plus faible concentration, 63% pour la concentration intermédiaire, alors qu'une structure amorphe apparaît pour la dose la plus élevée. Les cycles d'hystérésis présentent des formes typiques d'une réponse ferromagnétique. Le moment magnétique maximal a été obtenu pour la concentration $1 \times 10^{16}$ Mn/cm$^2$ à laquelle le taux de Mn en site de substitution est maximal. Les résultats expérimentaux ont été confrontés aux résultats des calculs *ab initio*. Différentes configurations de sites Mn et types d'occupation ont été pris en compte. Les calculs ont montré qu'un atome de Mn substitué sur le site d'un atome de Si possède un moment magnétique supérieur à celui d'un atome Mn sur un site C. Un modèle est introduit pour expliquer la dépendance de la structure magnétique au type d'occupation des sites. Les propriétés magnétiques de paires d'atomes Mn couplés, type ferromagnétique (FM) et antiferromagnétique (AFM), avec et sans sites voisins vacants, ont également été explorées.

## Structural and Magnetic Properties of Mn Implanted 6H-SiC

**Abstract**: In this study, n-Type 6H-SiC(0001) substrates were implanted with three fluencies of $Mn^+$ $5 \times 10^{15}$ Mn/cm$^2$ (Mn content: 0.7%), $1 \times 10^{16}$ (~2 %), and $5 \times 10^{16}$ cm$^{-2}$ (7%) with implantation energy of 80 keV and substrate temperature of 365°C. The samples were characterized using Rutherford Backscattering and Channeling Spectroscopy (RBS/C), High Resolution X-Ray Diffraction technique (HRXRD), micro Raman Spectroscopy (μRS) and Superconducting Quantum Interference Device (SQUID) techniques. The aims were to investigate implantation-induced defects upon dose and to study any correlation between disorder-composition and magnetic properties. RBS/C spectra were fitted using McChasy code, and the corresponding results show that 41% of Mn occupy substitutional sites for the lowest dose , 63% for intermediate Mn content, whereas an almost amorphization occurred for the highest dose. The hysteresis loops of the all samples have typical ferromagnetic shapes. The maximum magnetic moments were obtained for the fluence of $1 \times 10^{16}$ Mn/cm$^2$ at which the ratio of Mn at substitutional site was maximum. In addition, we investigated the structural and magnetic properties of Mn-doped 6H-SiC using ab-initio calculations. Various configurations of Mn sites and vacancy types were considered. The calculations showed that a substitutional Mn atom at Si site possesses larger magnetic moment than Mn atom at C site. A model is introduced to explain the dependence of the magnetic structure on site occupation. The magnetic properties of ferromagnetically (FM) and antiferromagnetically (AFM) coupled pair of Mn atoms with and without neighboring vacancies have also been explored.

**Discipline** Physique

**Mots-clés:** Carbure de Silicium, Implantation ionique, Défauts, Propriétés magnétiques, Calculs *ab initio*

Laboratoire des Sciences des Procédés et des Matériaux
UPR-CNRS 3407, 99 avenue J.B. Clément
93430 Villetaneuse
France